THEORETICAL AND EXPERIMENTAL STUDY OF THE CATALYTIC ROLE OF SUBSTRATE SURFACES IN DEPOSITION PROCESSES

by

Nickolas Mitchell Ashburn

APPROVED BY SUPERVISORY COMMITTEE:

_____

Kyeongjae Cho, Chair

_____

Julia Hsu

_____

Jiyoung Kim

_____

Robert Wallace

THEORETICAL AND EXPERIMENTAL STUDY OF THE CATALYTIC ROLE OF SUBSTRATE SURFACES IN DEPOSITION PROCESSES

by

NICKOLAS MITCHELL ASHBURN, BA, MS

DISSERTATION

Presented to the Faculty of

The University of Texas at Dallas

in Partial Fulfillment

of the Requirements

for the Degree of

DOCTOR OF PHILOSOPHY IN

MATERIALS SCIENCE AND ENGINEERING

THE UNIVERSITY OF TEXAS AT DALLAS

May 2021

ACKNOWLEDGEMENTS

I want to extend my gratitude to my advisor, Dr. Kyeongjae Cho for the opportunity to work in this group on a diverse number of projects. I am thankful for his guidance, sharing his knowledge, and support throughout my doctoral work. I am thankful for the general support of my committee members Dr. Julia W.P. Hsu, Dr. Jiyoung Kim, and Dr. Robert Wallace. I also would like to acknowledge Dr. Julia W.P. Hsu and Dr. Sampreetha Thampy for their guidance and providing me with valuable training in many synthesis and experimental analysis techniques. I would also like to thank Dr. Yongping Zheng for continuously sharing his knowledge with me in a plethora of areas. Finally, I want to express my most sincere gratitude to my family for their encouragement and continuous support throughout my education.

March 2021

THEORETICAL AND EXPERIMENTAL STUDY OF THE CATALYTIC ROLE OF SUBSTRATE SURFACES IN DEPOSITION PROCESSES

Nickolas Mitchell Ashburn, PhD
The University of Texas at Dallas, 2021

Supervising Professor: Kyeongjae Cho

Catalysis is largely important to many processes and aspects of modern technology. Catalysts have crucial roles in chemical synthesis, energy applications from pollution control to liquid fuel refining, and deposition and material growth. As the computers systems and software scales, computational modeling becomes an increasingly effective tool. Without modern computational methods, reaction processes can be slow and difficult to understand as more conventional trial and error methods can be inefficient. To understand these mechanisms that drive the catalytic reactions and aid in the design of new catalysts, density functional theory (DFT) was used in conjunction with experimental techniques to characterize catalytic reactions. In this study DFT is used to elucidate a rationale for surface-gas interaction in a way that give consistent and reliable predictions for catalytic processes. Additionally, the deposition of Co and Ru on various surfaces is investigate along with the role of reactants. These precursors are shown to interact uniquely with different surfaces, where different environmental chemistries allow specific surfaces to act as efficient catalysts facilitating low temperature decomposition when compared to others. We further explain these mechanisms along with a rationale for selective precursor design.

TABLE OF CONTENTS

LIST OF FIGURES

LIST OF TABLES

CHAPTER 1

INTRODUCTION

1.1 Catalysis and Surface Modeling

Catalysts exist in many applications ranging from energy and pollution control, biological mechanisms and drug production, to manufacturing and the fabrication of transistors. Catalysts allow reactions to take place at a faster rate and lower temperature than otherwise possible. Many catalysts are made from precious metals due to their ability to resist corrosion, oxidation, and thus performance degradation. However, oxide catalysts have shown much interest due to their lower costs in comparison.[1] In systems that may comprise of multiple surfaces, understanding the catalytic differences between metal and oxide, nitride, carbide or other surfaces is fundamentally important.

In order to understand the reaction mechanisms from a step by step perspective, many catalytic systems are modeled using first principle simulations in conjunction to experimental analysis. Density functional theory (DFT) is one of the most common techniques used to model reaction processes. In the case for catalysis, a thermodynamically quantifiable step by step depiction of the reaction process can be determined using DFT.[2,3] These reaction processes can then be used to describe and predict catalytic behavior in a certain environment. Thus, certain steps must be taken in order to create accurate models that ensure reliable reaction mechanisms.

Most catalysts involve a solid-gas or solid-liquid interaction where the solid is the catalyst. Therefore, one of the most crucial parts of the interaction is defining catalyst's local surface chemistry. This includes factors such as its electronic properties in the first few atomic layers, atomic morphology and bond coordination, as well as the energetics involved with surface

migration and adsorption/desorption. These local environments can have large effects on the computational approaches taken in order to predict experimental data.[4] Thus, experimental analysis is often needed to supplement certain material characteristics that DFT may fall short on. Such properties may include the surface facets presents, the surface area of the catalysis, certain electronic properties, and reaction rate at a given temperature or potential.

For growth or deposition mechanisms these same traits hold true. The surface of each substrate can act like a catalyst in that different surfaces, even facets of the same material, may facilitate varying growth rates for the same environment.[5,6] It is a common trend to see the growth of materials to be higher on metal substrates than that of oxides. This may be attributed to the ability of metals to dissociate and desorb reactants with lower kinetic penalties. Therefore, when developing and modeling precursors for manufacturing processes, the mechanistic and surface properties of the substrates need to be well understood.

1.2 Device Patterning and Atomic Layer Deposition

As the need for computational resources continues to grow and the transistor finds its way into more and more consumer goods, the need for high efficiency, low cost devices becomes increasing more important. One way this is being achieved is by packing more transistors on a single chip. Known commonly as Moore's law, roughly every two years, the number of transistors on a chip doubles.[7] This is achieved by scaling down both the pitch and the transistor itself to smaller and smaller dimensions. However, scaling to increasingly smaller dimensions creates certain problems which inadvertently affect device performance which must be overcome.

As electronic devices continue to scale down in size approaching critical dimensions (CD) as small as 3-10 nm, the smaller feature sizes become increasingly more difficult to pattern. The

most common patterning technique currently used is ArF laser immersion lithography. In 2004, ArF was limited to patterning feature with a minimum dimension of around 65 nm. This gave rise to the development of immersion, using deionized water, and MP, multi-patterning. The addition of these two techniques allowed for the scaling of lithography technology down to around 10 nm feature sizes. In surpassing this, extreme ultraviolet lithography (EUV) was developed to scale down past the capabilities of ArF MP. EUV however, is more prone to stochastic effects, edge roughness, and defects in addition to having poor power output making it slow and economically taxing.[8]

EUV works through a power source which converts plasma into light at a wavelength around 13.5 nm. This source is then focused using multilayered mirrors, Mo/Si. The thickness of these layers has been shown to affect the source intensity through a trade-off between maximizing the constructive interference of reflected beams and minimizing the absorption of the source.[9] Correspondingly, these mirrors reflect around 70% of the source with layer tolerances of 0.025 nm. This loss of the source's power is responsible for the longer exposure times needed to pattern using EUV. The stochastic effects and edge roughness produced from EUV patterning is caused by photon shot noise.[10] As the wavelength decreases, the light source's intensity is distributed over fewer photons. In addition, the imperfect Mo/Si reflectivity further reduces the photon concentration. With fewer photons creating the pattern, stochastic failures become more common.

One of the proposed techniques to aid in patterning small features is area selective atomic layer deposition (AS-ALD) or ALD-enabled nanopatterning. In AS-ALD, material for the next layer is deposited selectivity on one or more specific materials that make up the substrate while avoiding growth on unwanted substrate surfaces. ALD, a sub-set of chemical vapor deposition

(CVD), works by depositing material below the decomposition temperature of the precursor thus making ALD as self-limiting reaction. In contrast to CVD, where the precursor and reactant are flown through the deposition chamber constantly, the precursor and reactant are only exposed to the chamber in separate pulses. This provides more uniform growth characteristics and lower temperature deposition.[11] There are four main steps to the cyclic reaction process, precursor exposure, purge, reactant exposure, and final purge. Occasionally more than one reactant may be used which requires another reactant and purge step.[12] Figure 1.1 shows a diagram of the ALD reaction steps.

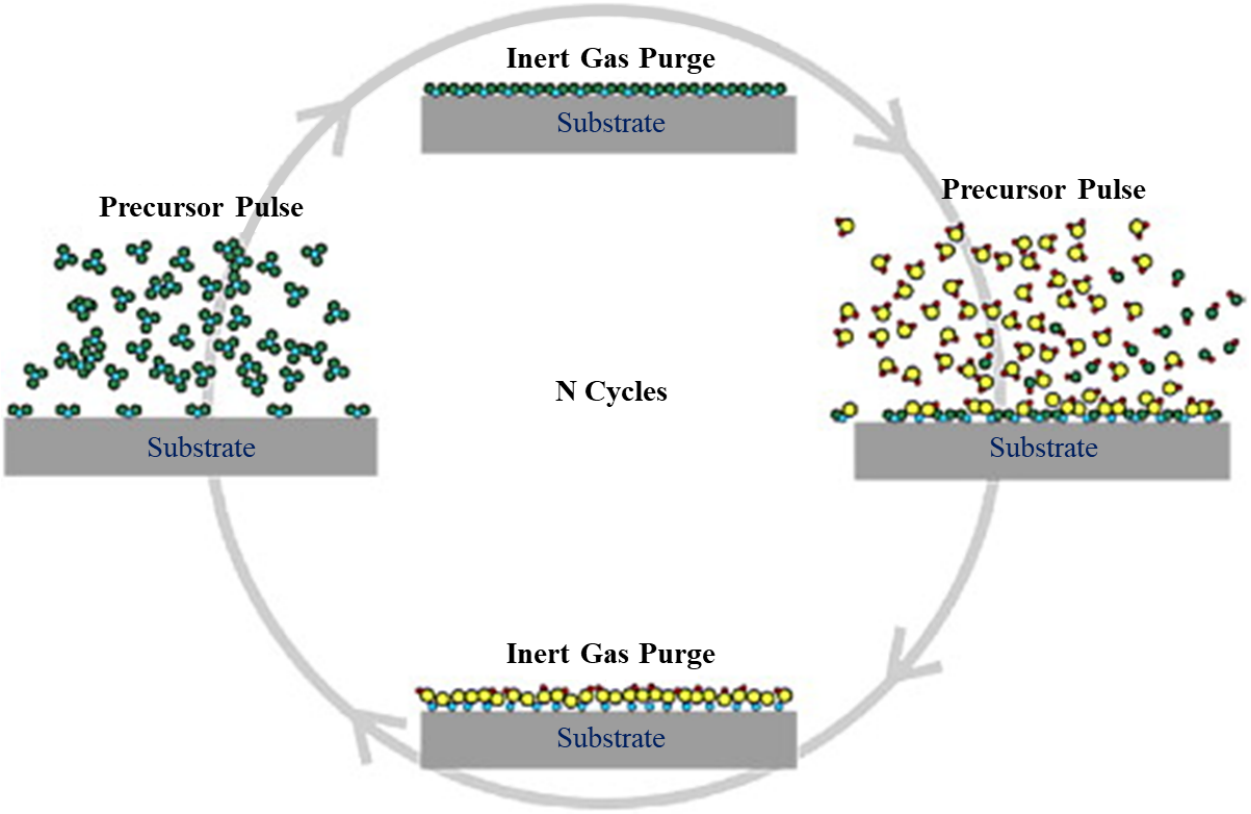

Figure 1.1. Diagram of ALD process steps.[13]

During the precursor exposure, the precursor interacts with substrate surface by bonding to various active sites. Once these active sites are saturated, the adsorption of the precursor stops,

being self-limited. This allows the deposition of the desired material to be very uniform even over high aspect ratio structures. The subsequent purge, usually an inert gas, is done to remove any remaining, non-bonding precursor molecules out of the system. The reactant is then introduced to the chamber where it interacts with both the precursor and the substrate surface. This step is responsible for the deposition and bonding of the desired material to the substrate surface. The final purge is again used to clear the chamber of non-bonded reactant and reaction products.

Certain precursor reactant chemistries allow ALD to become area selective and specific surfaces.[14,15] AS-ALD can thus be used to pattern features on a device. AS-ALD has a few main benefits to the lithography process. For AS-ALD, the process and tools are cheaper than EUV, the patterning or growth of features is not slowed down by the smaller feature sizes which require EUV, and the stochastic defects found in EUV can theoretically be removed through ideal or close to ideal area selective deposition. However, AS-ALD does have significant challenges in its use in device patterning. To achieve selective deposition, the precursor and reactant chemistry must show a strong selective affinity for a specific surface. However, this selective affinity can be very difficult to achieve. If the deposition temperature is above the precursor decomposition temperature, the precursor is thermodynamically unselective, or the surface migration barriers are low the deposited material will not grow selectively. Additionally, having slow or poor growth on the undesirable surface can lead to defects like bridging. Therefore, the kinetic and thermodynamic properties of the precursor and reactant must be carefully tuned such that as little as possible growth occurs on the undesirable surface.

1.3 Interconnect Scaling and Metals

As the pitch between like features scales down, the metal lines which connect the transistors, capacitors, resistors and other various components in the device must scale as well. These metal interconnects found in the back end of line (BEOL) are commonly made from Al, in older technology or technology where the feature size isn't as important, and Cu, for devices with smaller feature sizes where the conductivity of Al lines isn't enough. These Cu and Al lines, however, require thick barriers and liners which reduces the effective size of the interconnect trench.[16] This in turn reduces the cross-sectional area of the metal line causing a decrease in the effective conductivity, especially as the CDs of interconnects push below the 16 nm mark of those found in modern devices. These barriers and liners are needed for metals such as Cu due to their strong diffusivity into dielectrics like SiO_2.[17] Due to increasing resistivity with the scaling of BEOL, alternative metals such as Co and Ru have been proposed to replace Cu.[18] Figure 1.2 shows the correlation between the product of resistivity and the mean free path, λ, and melting temperature or cohesive energy.

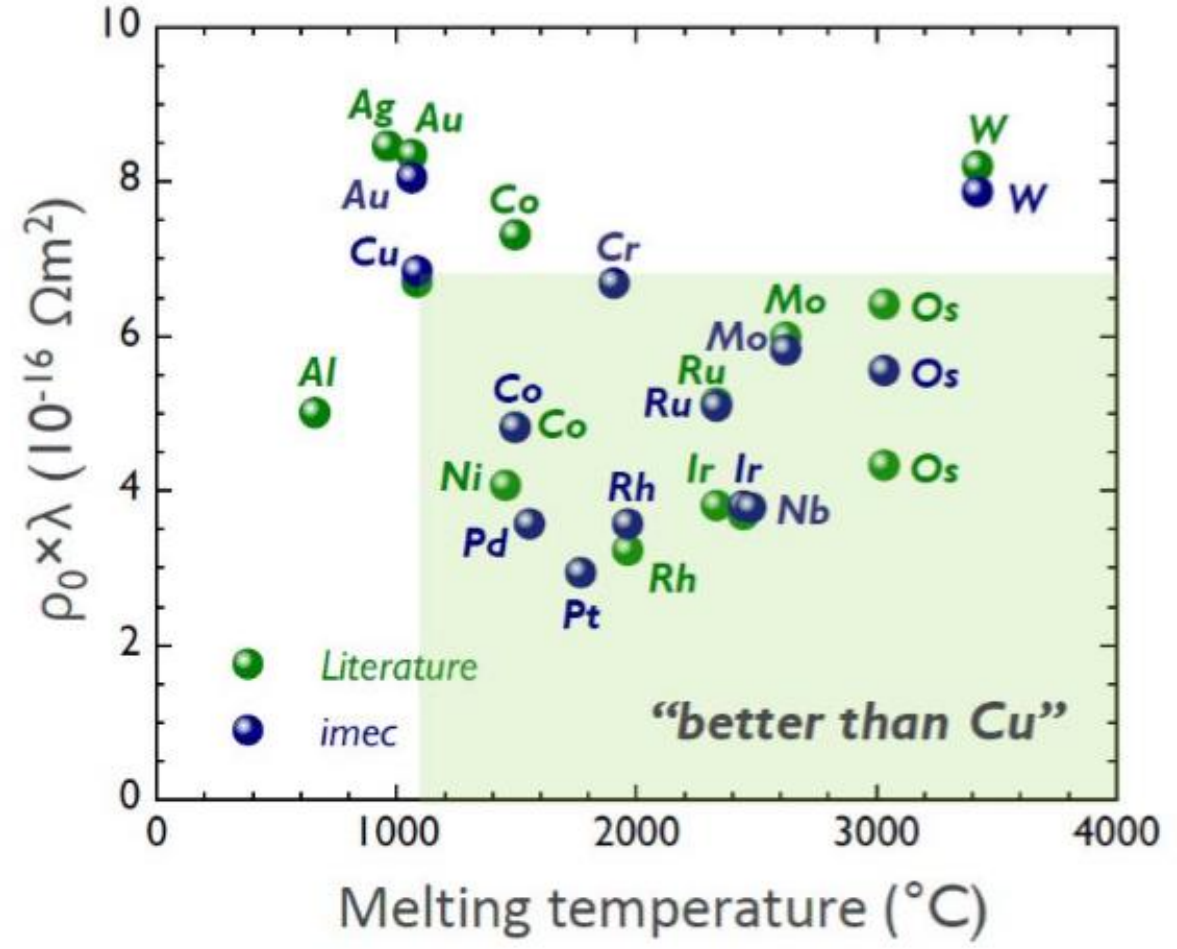

Figure 1.2. Product of resistivity and mean free path plotted against the melting temperature.[19]

The smaller product of resistivity and mean free path is used to indicate potential metals with lower resistivity at small dimensions. Additionally, a higher melting temperature is indicative of a stronger cohesive energy and interatomic bond strength. This in turn increases the activation barriers required for dielectric diffusion and decreases the thermodynamic formation energy of secondary compounds which are often a result of oxidation from dielectric diffusion. The combination of these two qualities, when ideal, gives interconnect options that yield better

resistivity at small dimensions and do not require the use of liners and barriers allowing the effective conductive cross-section to be larger.

It can be seen in Figure 1.2 that Co and Ru are both options that improve upon Cu as an interconnect material at small dimensions. It is important to note that there are several metals in this range that may be used to replace Cu. However, several of these are precious metals and thus are more costly alternatives. Additionally, these trends do not always yield better performance in application. Consequently, the effective resistance of Co, Ru, and Cu are plotted in Figure 1.3.

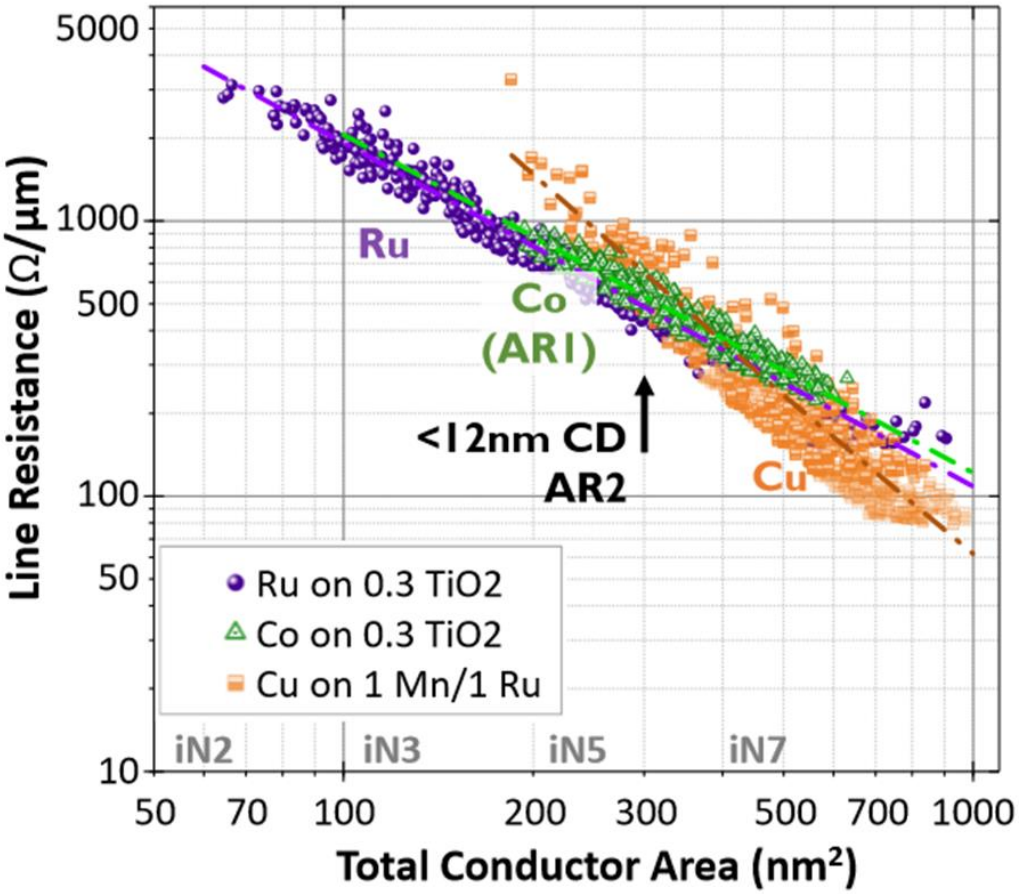

Figure 1.3. Lines resistance versus the total conductor area for Cu, Co, and Ru metal interconnects.[20]

Here the line resistance is plotted versus its dependence on the total conductor area, or trench cross-section. Co and Ru noticeably outperform Cu below 400 nm^2. This is attributed to thicker liner/barrier required for Cu interconnects which inversely affects the line conductivity.

1.4 Catalyst Role in Deposition Process

To achieve the selective deposition of a material on a specific surface over another, the surface reactant reaction must be more favorable than the competing surfaces. Therefore, understanding the catalytic properties that facilitate deposition are crucial to predicting and understanding selective deposition mechanisms. Catalysts facilitate a reaction at a lower temperature than otherwise possible by lowering the kinetic barriers involved in the reaction mechanism. The better the catalyst the lower the activation energy of a reaction.

AS-ALD relies on the fundamental differences between multiple surfaces. In order to be selective, some surfaces must demonstrate certain properties other surfaces do not. One way to study these properties is to look at the surface interaction with simple molecules. These reactions have fewer products and the reaction mechanisms are often more simplistic making the modeling of reaction pathways quicker and easier. One of the most well-known catalysts is that found in the exhaust of combustion engines. The precious metal Pt, Pd, and Rh based catalysts are commonly used to oxidize NO_x, CO, and hydrocarbon particulates.[21] The surface of the catalyst readily dissociates oxygen in the environment. In addition, the oxygen-surface binding energy is not extremely strong, allowing the surface oxygen to react favorably with hydrocarbons, NO_x, and CO. When compared to other material surfaces, these properties facilitate and accelerate the reaction process. Other materials may have surfaces which show poor dissociation of O_2 or binding of oxygen which is too strong for desorption.

However, oxygen dissociation is not the only property for the precious metals. Many precious metals show strong dissociative properties with reducers such as ammonia, formic acid, or amines while still maintaining lower desorption barriers. Furthermore, many precious metals show strong resistance to thermal degradation, surface passivation, and chemical decomposition. These strong catalytic properties make many metals highly efficient in multiple fields of catalysis and material selective deposition.

When identifying selective precursors, the interaction and decomposition of the reactants on the surface must also be more favorable on a specific surface. Previous work has shown how the catalytic properties of the substrate can facilitate and block certain reaction mechanisms leading to surface selective growth.[22] The selective deposition of metal oxides in this work is shown to be selective towards metals over SiO_2, Al_2O_3, and Au due to the ability of certain metals to dissociate oxygen gas on their surfaces. This dissociative property of weakly bound oxygen facilitates the growth of certain metal oxides while the more strongly bound oxygen on the SiO_2, Al_2O_3 are shown to interact poorly with the Fe precursors. Furthermore, the dissociative properties of oxygen on SiO_2, Al_2O_3, and Au are shown to be insufficient. Similar reasoning can be applied to AS-ALD of different systems.[23-26]

References

(1) National Research Council (US) Chemical Sciences Roundtable. (2012). Replacing Critical Materials with Abundant Materials. In the Role of the Chemical Sciences in Finding Alternatives to Critical Resources: A Workshop Summary. National Academies Press (US).

(2) Zhang, C., Cao, H., Wang, C., He, M., Zhan, W., & Guo, Y. (2020). Catalytic mechanism and pathways of 1, 2-dichloropropane oxidation over LaMnO3 perovskite: An experimental and DFT study. Journal of Hazardous Materials, 402, 123473.

(3) Reynaldi, V., Cahyanto, W. T., & Abdullatif, F. (2020). Quantum Simulations of Preferable H2O Dissociation Pathway on the Ru-Alloyed Pt (111) Surface Based on Density Functional Theory. In Key Engineering Materials (Vol. 840, pp. 495-500). Trans Tech Publications Ltd.

(4) Aykol, M., & Wolverton, C. (2014). Local environment dependent GGA+ U method for accurate thermochemistry of transition metal compounds. Physical Review B, 90(11), 115105.

(5) Bobb-Semple, D., Nardi, K. L., Draeger, N., Hausmann, D. M., & Bent, S. F. (2019). Area-selective atomic layer deposition assisted by self-assembled monolayers: a comparison of Cu, Co, W, and Ru. Chemistry of Materials, 31(5), 1635-1645.

(6) Waechtler, T., Oswald, S., Roth, N., Jakob, A., Lang, H., Ecke, R., ... & Hietschold, M. (2009). Copper oxide films grown by atomic layer deposition from Bis (tri-n-butylphosphane) copper (I) acetylacetonate on Ta, TaN, Ru, and SiO2. Journal of The Electrochemical Society, 156(6), H453.

(7) Huang, A. (2015). The Death of Moore's Law Will Spur Innovation. Institute of Electrical and Electronics Engineers: Technology, Engineering, and Science News.

(8) De Bisschop, P. (2017). Stochastic effects in EUV lithography: random, local CD variability, and printing failures. Journal of Micro/Nanolithography, MEMS, and MOEMS, 16(4), 041013.

(9) Montcalm, C., Bajt, S., Mirkarimi, P. B., Spiller, E. A., Weber, F. J., & Folta, J. A. (1998, June). Multilayer reflective coatings for extreme-ultraviolet lithography. In Emerging Lithographic Technologies II (Vol. 3331, pp. 42-51). International Society for Optics and Photonics.

(10) Hutchinson, J. M. (1998, June). Shot-noise impact on resist roughness in EUV lithography. In Emerging Lithographic Technologies II (Vol. 3331, pp. 531-536). International Society for Optics and Photonics.

(11) Doll, G. L., Mensah, B. A., Mohseni, H., & Scharf, T. W. (2010). Chemical vapor deposition and atomic layer deposition of coatings for mechanical applications. Journal of thermal spray technology, 19(1-2), 510-516.

(12) Lu, J., Low, K. B., Lei, Y., Libera, J. A., Nicholls, A., Stair, P. C., & Elam, J. W. (2014). Toward atomically-precise synthesis of supported bimetallic nanoparticles using atomic layer deposition. Nature communications, 5(1), 1-9.

(13) Leskelä, M., Niinistö, J., & Ritala, M. (2014). 4.05-Atomic Layer Deposition. *Comprehensive Materials Processing*, *4*, 101-123.

(14) Pinna, N., & Knez, M. (Eds.). (2012). Atomic layer deposition of nanostructured materials. John Wiley & Sons.

(15) Knez, M., Nielsch, K., & Niinistö, L. (2007). Synthesis and surface engineering of complex nanostructures by atomic layer deposition. Advanced Materials, 19(21), 3425-3438.

(16) Willis, B. G., & Lang, D. V. (2004). Oxidation mechanism of ionic transport of copper in SiO2 dielectrics. *Thin Solid Films*, 467(1-2), 284-293.

(17) Fisher, I., & Eizenberg, M. (2008). Copper ion diffusion in porous and nonporous SiO2-based dielectrics using bias thermal stress and thermal stress tests. *Thin Solid Films*, 516(12), 4111-4121.

(18) Pedreira, O. V., Croes, K., Leśniewska, A., Wu, C., Van Der Veen, M. H., De Messemaeker, J., Vandersmissen, K., Jourdan, N., Wen, L.G., Adelmann, C. & Briggs, B. (2017, April). Reliability study on cobalt and ruthenium as alternative metals for advanced interconnects. In 2017 IEEE International Reliability Physics Symposium (IRPS) (pp. 6B-2). IEEE.

(19) Adelmann, C., Sankaran, K., Dutta, S., Gupta, A., Kundu, S., Jamieson, G., Moors, K., Pinna, N., Ciofi, I., Van Eishocht, S., & Bömmels, J. (2018, June). Alternative Metals: from ab initio Screening to Calibrated Narrow Line Models. In 2018 IEEE International Interconnect Technology Conference (IITC) (pp. 154-156). IEEE.

(20) van der Veen, M. H., Heyler, N., Pedreira, O. V., Ciofi, I., Decoster, S., Gonzalez, V. V., Jourdan, N., Struyf, H., Croes, K., Wilson, C.J. & Tőkei, Z. (2018, June). Damascene benchmark of Ru, Co and Cu in scaled dimensions. In 2018 IEEE International Interconnect Technology Conference (IITC) (pp. 172-174). IEEE.

(21) Thakur, P. C. (2018). Advanced mine ventilation.

(22) Singh, J. A., Thissen, N. F., Kim, W. H., Johnson, H., Kessels, W. M., Bol, A. A., ... & Mackus, A. J. (2018). Area-selective atomic layer deposition of metal oxides on noble metals through catalytic oxygen activation. Chemistry of Materials, 30(3), 663-670.

(23) Minjauw, M. M., Rijckaert, H., Driessche, I. V., Detavernier, C., & Dendooven, J. (2019). Nucleation enhancement and area-selective atomic layer deposition of ruthenium using RuO4 and H2 gas. Chemistry of Materials, 31(5), 1491-1499.

(24) Stevens, E., Tomczak, Y., Chan, B. T., Altamirano Sanchez, E., Parsons, G. N., & Delabie, A. (2018). Area-selective atomic layer deposition of TiN, TiO2, and HfO2 on silicon nitride with inhibition on amorphous carbon. Chemistry of Materials, 30(10), 3223-3232.

(25) Zyulkov, I., Krishtab, M., De Gendt, S., & Armini, S. (2017). Selective Ru ALD as a catalyst for sub-seven-nanometer bottom-up metal interconnects. ACS applied materials & interfaces, 9(36), 31031-31041.

(26) Chen, R., Kim, H., McIntyre, P. C., Porter, D. W., & Bent, S. F. (2005). Achieving area-selective atomic layer deposition on patterned substrates by selective surface modification. Applied Physics Letters, 86(19), 191910.

CHAPTER 2

DENSITY FUNCTIONAL THEORY

2.1 Schrödinger Equation

Density functional theory (DFT) relies on modern physics to calculate atomic level interactions. These interactions are often described through the Schrödinger equation which helps explain a quantum mechanical system. Quantum mechanical systems are often described at the atomic and subatomic levels exhibiting characteristics such as wave-particle duality, the quantization of states, and entanglement among others.[1] The Schrödinger equation describes these systems through a wavefunction of quantized states. This representation is most generally expressed as the time-dependent Schrödinger equation:

$$i\hbar\frac{d}{dt}\psi(r,t) = \hat{\mathrm{H}}\psi(r,t) \tag{2.1}$$

Where *i* is imaginary unit, $\hbar$ is Planck's constant per radian, Ψ is the quantum wavefunction dependent on time and position, *t* and *r* respectively, and $\hat{\mathrm{H}}$ is the Hamiltonian operator describing the systems energy. For systems not explicitly dependent on time, the time independent Schrödinger equation can be used to describe the system as follows:

$$E\psi(r) = \hat{\mathrm{H}}\psi(r) \tag{2.2}$$

In the time independent Schrödinger equation *E* is the energy of the system and *r* is the three-dimensional position vector. Since this equation is not time dependent, Ψ represents a standing wave for a static description of a system. This description is often applied to the hydrogen atom and its single electron. However, for many bodied systems a solution cannot be achieved analytically. Due to this there exists methods such as the Hartree-Fock method.[2] Using such

methods do not come without their challenges however, as computational costs for large systems such as molecules and extended solids are enormous making these methods impractical. In many bodied problems for *N* particles, there exists 3*N* degrees of freedom. To compute these and reduce the computational resources required, developments in computational methods have been made such that the electronic density can be simplified from 3*N* to 3 variables as approximated in DFT.

2.2 Hohenberg-Kohn Theorems

In 1964 Hohenburg and Kohn proved two theorems allowing DFT to become possible.[3] These were as follows:

- The external potential is a unique functional of the electron density.
- The electron density that minimizes the energy of the potential is ground state density.

These theorems allow the variables to be reduced from 3*N* to 3, allowing the electron density to be represented by

$$n(r) = 2\sum_i \psi_i^*(r)\psi_i(r) \tag{2.3}$$

Thus, the energy as a function of the ground state electron density can be represented as

$$E[n(r)] = F[n(r)] + \int V(r)n(r)d^3r \tag{2.4}$$

Where $n(r)$ is the electron density which is the ground state at its lowest energy, $V(r)$ is the external potential, and $F[n(r)]$ is and independent functional consisting of the kinetic energy and Hartree or electron-electron interaction energy. While the Hohenberg-Kohn theorems have provided excellent advancement towards solving for the exact ground state solution of a given environment, the $F[n(r)]$ term is still unknown.

2.3 Kohn-Sham Equations

In 1965, Kohn and Sham proposed an additional technique which equates the ground state density of a system of interacting particles in an external potential to that of a fictitious system of non-interacting particles.[4] This is also known as the Kohn-Sham system or equation and is written as follows:

$$\left[-\frac{\hbar^2}{2m}\nabla^2 + V_s(r)\right]\varphi_i(r) = \varepsilon_i\varphi_i(r) \tag{2.5}$$

Where $V_s(r)$ is the Kohn-Sham potential, $\varphi_i(r)$ is the Kohn-Sham orbital, and ε_i is the orbital energy of $\varphi_i(r)$. The Kohn-Sham potential is a combination of three different potentials (V, V_H, and V_{xc}) where V is the potential representing the interaction between the atomic nuclei and the electron, V_H is the Hartree potential, and V_{xc} is the exchange-correlation potential. The Hartree potential describes the coulomb interaction between one electron and the electron density and is thus given by

$$V_H(r) = e^2 \int \frac{n(r')}{|r-r'|} d^3r' \tag{2.6}$$

Where e is the electron charge. It should be noted that the exact ground state density solution is not provided through these equations and thus the solution must be solved iteratively from an initial electron density guess. This density can then be used to solve for the wavefunction using the Kohn-Sham equations which in turn is used to solve for the electron density. This self-consistent manner of solving for the electron density and the wavefunction will continue iteratively until it converges within a specified parameter. The total energy of the system can then be described by Equation (2.4) as

$$E[n(r)] = \sum_i \varepsilon_i - \frac{e^2}{2}\int d^3\, r \int \frac{n(r)n(r')}{|r-r'|} d^3r + E_{xc}[n(r)] + \int V_{xc}(r)n(r)d^3r \tag{2.4}$$

2.4 Exchange-Correlation Functionals

The accuracy of the Kohn-Sham equations depends heavily on the exchange-correlation functional used. However, exact functionals for the exchange-correlation are unknown, except for the free electron gas, and multiple approximations exist. One of the most common is the local density approximation (LDA) which was proposed by Kohn and Sham.[4] LDA is derived from the homogeneous electron gas approximation and hence defines the exchange-correlation by only the local electron density. Although LDA uses the exchange-correlation solution from a homogeneous electron gas and applies it to inhomogeneous solids and molecules, its results have been relatively successful, particularly for systems which lack strong electron correlation. However, because LDA assumes the density to be the same everywhere, it has a tendency to underestimate the exchange energy while over-estimating the correlation energy. Thus, it is common to include the electron density gradient as a higher order approximation. This allows the non-homogeneity of extended solids and molecules and the change in electron density away from the point of interest to be taken into consideration. Such approximations are often referred to as the generalized gradient approximation (GGA) which comes in many flavors, most notably the Perdew-Wang functional (PW91) and the Perdew-Burke-Ernzerhof functional (PBE).[5] Since GGA is a more realistic assumption it tends to outperform LDA methods leading to more accurate forces, system energies, and electronic structures.

References

(1) Schrödinger, E. An Undulatory Theory of the Mechanics of Atoms and Molecules. Physical Review, 28, 1049-1070, 1926

(2) Fischer, C. F. General Hartree-Fock program. Computer Physics Communication, 43, 355-365, 1987.

(3) Hohenberg, P., & Kohn, W. Inhomogeneous electron gas. Physical review 136 (3B), B864, 1964.

(4) Kohn, W., & Sham, L. J. Self-consistent equations including exchange and correlation effects. Physical Review. 140 (4A): A1133–A1138, 1965.

(5) Perdew, John P., Chevary, J. A., Vosko, S. H., Jackson, Koblar A., Pederson, Mark R., Singh, D. J., & Fiolhais, Carlos. Atoms, molecules, solids, and surfaces: Applications of the generalized gradient approximation for exchange and correlation. Physical Review B. 46 (11): 6671, 1992.

CHAPTER 3

THEORETICAL DESIGN PRINCIPLES FOR EXPERIMENTALLY ACCURATE CATALYSIS SURFACES

3.1 Introduction

This chapter is written with permission based on the published work by authors Nickolas Ashburn, Yongping Zheng, Sampreetha Thampy, Sean Dillon, Yves Chabal, Julia Hsu, and Kyeongjae Cho. Nickolas Ashburn wrote the manuscript, performed all calculations, XRD, and TPD studies, as well as grew all the samples. Yongping Zheng aided in developing the methodology. Sampreetha Thampy took the BET and FTIR data. Sean Dillon performed many FTIR and LEIS studies that contributed to the methodology and development of this work although these specific data sets are not shown here. Integrated Experimental-Theoretical Approach to Determine Reliable Molecular Reaction Mechanisms on Transition Metal Oxide Surfaces. ACS applied materials & interfaces, 11(33), 30460-30469. Copyright (2019) American Chemical Society.

3.1.1 Background

Platinum group metals (PGMs) have historically been the primary materials for many catalytic applications (e.g., Pt in fuel cells and exhaust gas cleaning catalytic converters) due to the unique electronic structure of their surfaces. The PGM catalytic reactivity is well understood based on the d-orbital electronic structure of transition metal surfaces. However, PGMs are rare elements in the earth's crust (typically ppb level), and to overcome the limited availability of PGM catalysts, modern catalytic material development has been focused on abundant elements (e.g. 3d transition

metals) with high efficiency at a low cost of production. Due to their high reactivity in elemental form, many of these alternative materials are based on abundant transition metal compounds (e.g. Mn oxides rather than Mn) which are commonly used in applications such as oxidation catalysts, electrocatalysts, sensors, batteries, and fuels cells.[1-4] However, in theoretical studies, these transition metal (TM) compounds are difficult to model, and thus understand, due to their strongly correlated d shell electrons and dependence on their chemical environments.[5-7] Such strongly correlated *d* electrons are not accurately modeled within the usual density functional theory (DFT) method using the local density approximation (LDA) or generalize gradient approximation (GGA). Thus, on-site Coulomb correlation interactions, needed to correct for the strong correlation effect, are included by the Hubbard U correction. Furthermore, the TM compound material's surfaces differ from their bulk structure in their atomic oxidation states, charge, bond geometries, and thus different *d* electron occupation and TM binding energies, all which affect chemical reactions on the surface. This complexity makes modeling the TM compound surface even more challenging as its atomic arrangement on surface is usually unknown. Specifically, uncertainty in the surface TM *d* electron configuration makes it very difficult to accurately correct the *d* electron correlation by using suitable Hubbard U values on TM compound surfaces. Here we demonstrate a unique technique which can be used to characterize the surface chemistry of oxide materials such as perovskites (ABO_3 where A and B are unique cations such as $SmMnO_3$), mullites (AB_2O_5 such as $SmMn_2O_5$), binary oxides (A_nO_m such as CeO_2) and others commonly found compounds in various types of catalysts.

The surface chemistry of a material, in a broad sense, includes the study of its electronic structure, atomic arrangement, bond lengths and bonding geometry, and binding energies between

atoms on the surfaces. These features are particularly important when studying materials used as catalysts for various applications as the catalytic reactions occur primarily on the material's surfaces. This work shows a novel characterization method for modeling reliable surface reactions at TM sites on TM compound surfaces using DFT method. Previous studies have shown how DFT method can be used to accurately model bulk materials, including those involving strongly correlated d and f shell electrons.[5-7] However, DFT methods are often difficult to use when modeling reaction pathways due to the high computation costs of running accurate functionals such as Heyd-Scuseria-Erzenhof (HSE06) and the inaccuracies brought about in under and over-binding when using HSE and the GGA for electronic interactions.[6,7] Although bulk oxide properties are well reported in literature, there have been significantly less studies done on a universal surface modeling process for reaction mechanisms across multiple materials. Thus, the bulk electronic correlation (e.g., Hubbard U value) is usually assumed for the surface TM atoms. Considering the difference in atomic bonding and chemical environment on TM compound surfaces from bulk environment, such approximation would introduce significant errors in DFT treatment of surface TM atoms. Thus, we propose a unique surface characterization process that uses the activation energy of surface atoms obtained through temperature programmed desorption (TPD) which can then be used to quantitatively model the surface of the material through DFT, and therefore, the reaction pathways. This approach allows the reaction mechanisms to be reliably and accurately understood in a step by step process where each reaction step has an independent Gibbs free energy change.

For this purpose, eight different oxide materials were studied, including mullites, perovskites, and binary oxides. These materials were studied with oxygen TPD, to create the surface chemistry

(as defined in the previous paragraph) for each material, then with CO or NO TPD, to verify the surface chemistry and study a surface gas reaction. Additionally, molecular over-binding, which is found in many covalent molecules, is discussed in this work, impacting the reaction mechanisms of each catalytic material. The GGA method is known to have under and over-binding issues as mentioned before. This DFT binding energy issue is already known to exist in molecular oxygen.[6] We found that most covalent molecules had some amount of over-binding and thus affected the calculated NO and CO oxidation processes. To correct for these issues, the bond lengths and charge states were analyzed from DFT for each molecule in different environments to identify a correlation between charge density and the over-binding amount. The relationship comes out as a linear correlation, which was then used to correct the over-binding of surface adsorbed molecules and atoms.

For the comparative study, experimental oxide samples and procedures are carefully selected as follows. Both binary and complex oxides were chosen to incorporate a variety of different material structures in order to demonstrate the wide range of applications the TPD process applies to. CO oxidation does not require over-binding corrections when the desorbed gas is CO_2, which is discussed in section 3.3.3. Thus, perovskite oxides were chosen to model this reaction process. NO oxidation however, does require over-binding corrections, and to demonstrate how the over-binding of surface and molecular NO_x is calculated, NO oxidation was modeled on mullite-type oxides. Additionally, each material must be able to crystallize at low temperatures such that they have a large enough surface area to produce a strong gas sorption signal. Low surface areas and large particle size samples were not able to produce reliable desorption peaks in the RGA. The materials must also be stable through the temperature range we selected for this study.

Furthermore, each material must also have only a few stable surfaces. A multitude of present surfaces will convolute the peak positions which increases the complexity in determining which peaks belong to which surfaces. For these last three reasons, only one binary oxide was selected, CeO_2.

3.2 Materials and Methods

3.2.1 Experimental Design and Synthesis Methods

The first step in creating a reliable description of the surface chemistry, is to identify and model the exposed or cleavage surfaces. This identification can be done using Fourier-transform infrared spectroscopy (FTIR) and calculating the possible vibration modes of adsorbed molecules or with TPD. In this work both FTIR and TPD experiments are performed. Since all our samples were oxides, oxygen TPD was performed on every sample. The activation energies of the oxygen peaks in TPD was then determined through equations for kinetic reaction processes. DFT was then used to calculate the desorption peaks for a specific surface. The number of oxygen peaks along with their temperature differences and their total partial pressures were then compared between TPD and that calculated using theory. This comparison, along with surface formation energy calculations, enabled us to identify the surfaces present on our oxide samples. Since transition metal oxides and lanthanide oxides have strongly correlated *d* and *f* shell electrons, an effective interaction parameter ($U_{eff} = U - J$) is necessary to model surface and bulk properties. Without accurately modeling *d* and *f* shell electron correlations, the initial peak positions from DFT won't match those from TPD. Therefore, the binding and activation energies from oxygen TPD were used to help calculate the oxygen-metal bond strength in DFT, which was then compared to the bulk data. It is shown that the surface binding energies are not comparable to that of the bulk. Once

DFT and TPD showed similar surface chemistry, through their oxygen desorption temperatures, a gas reaction process was studied on the surface for some of the materials. This was done through the oxidation of CO on perovskite and NO on mullite. Similarly, NO and CO TPD were performed which yielded a partial pressure versus temperature plot. The surface model validated by oxygen TPD was then used to model the molecule oxidation reactions for NO and CO. Consistently, the corresponding gas oxidation energies from DFT showed to be highly reliable when compared to the TPD data from CO and NO gas.

Eight different oxides materials were synthesized and studied in this work. These included $SmMn_2O_5$, $PrMn_2O_5$, YMn_2O_5, $GdMn_2O_5$, $LaFeO_3$, $LaMnO_3$, $SmCoO_3$, and CeO_2. Each sample was synthesized using analytical grade A= (Y, La, Ce, Pr, Sm, Gd) $A(NO_3)_3 \cdot 6(H_2O)$, $Co(NO_3)_2 \cdot 6(H_2O)$, $Fe(NO_3)_3 \cdot 9(H_2O)$, $Mn(NO_3)_2 \cdot 4(H_2O)$, $KMnO_4$, and $Mn(C_2H_3O_2)_2 \cdot 4(H_2O)$ through a variety of different synthesis methods in attempt to yield high surface area samples. All mullite-type oxides, AB_2O_5, where A is different elements, B is Mn, and O is oxygen, were synthesized using a hydrothermal method. Here, $KMnO_4$, 0.006 moles, and $Mn(C_2H_3O_2)_2 \cdot 4(H_2O)$, 0.014 moles, were mixed in stochiometric amounts with 0.01 moles of $A(NO_3)_3 \cdot 6(H_2O)$, a ratio of 3:7:5 respectively, and dissolved in 60 ml of deionized water. The pH was then brought up between 9.8 and 10.4 using a 5M NaOH solution and allowed to mix for 30 minutes. These samples were then placed in Teflon lined autoclaves at 60 percent fill and heated at 180 °C for 24 hours. The resulting product was dried at 105 °C. Fe perovskite, ABO_3, materials were synthesized using a coprecipitation method as shown by Thampy *et al.*[4] The samples were calcined at 700 °C for 8 hours. For all other perovskites, a combustion synthesis method was employed. $A(NO_3)_3 \cdot 6(H_2O)$, $Mn(NO_3)_2 \cdot 4(H_2O)$ or $Co(NO_3)_2 \cdot 6(H_2O)$, and citric acid, $C_6H_8O_7$, were dissolved in 10 ml

deionized water in a molar ratio of 3:3:5 respectively. The solution was dried at 90 °C for 12 hours then placed in a furnace and heated to 250 °C for 2 hours. The sample was then removed and crushed for 15 minutes followed by a final calcination at 600 °C for 8 hours. Lastly, CeO_2 was synthesized using the combustion method above, less the final calcination step.

3.2.2 Theoretical Methodology

The formation energy of each material was calculated using the atomization energy. Additionally, to achieve the most accurate energy calculations for elements with strongly correlated orbitals, the GGA+U method was employed.[8,9] Note that the formation energy is negative when favorable. This atomization energy can best be described by Eq. (1), where ΔE^f is the formation energy of a material which is equal to the total material energy, E^m, minus the sum of the individual atomic energies, E_i, for each species *i*.

$$\Delta E^f = E^m - \sum_i E_i \quad (1)$$

Since all calculations are done at 0 K, binding energies are calculated using Eq. (2). Here $\Delta H^{Absorbed}$ is the formation enthalpy of the surface with an adsorbed molecule, $E^{Surface+Molecule}$ is the total energy of the surface with the adsorbed molecule, $E^{Surface}$ is the total energy for the surface, and $E^{Molecule}$ is the molecule's total energy.

$$\Delta H^{Absorbed} = E^{Surface+Molecule} - E^{Surface} - E^{Molecule} \quad (2)$$

Furthermore, corrections must be adopted to account for the over-binding found in molecular oxygen.[6] This value is found to be a reduction of 1.36 eV to the oxygen total energy. Further over-binding in covalently bonded molecules, such as CO_x and NO_x, has also been observed. To correct for this, multiple atomically similar species were calculated and their DFT formation energies were compared to their empirically measured formation energies using the NIST-JANAF Tables for

Thermochemistry. To get accurate results, the zero-point energies were considered for each molecule. The charge state of each atom was examined to create a linear fit of over-binding vs charge density in an atomic radius. Finally, surface adsorbed molecular over-binding could then be corrected by using a linear fit to the charge state of various related molecules. Equation 3 describes how over-binding values were calculated by subtracting the empirically measured value from the GGA+U calculated value. Furthermore, the hybrid functional Heyd-Scuseria-Erzenhof (HSE06) was also used to correct for the over-binding found when using GGA.[10] However, even this approach showed over-binding issues for molecules adsorbed on a material surface. These over-binding values, zero-point energies, and the charge vs radius relationships along with the corresponding corrections are listed in the results and discussions section.

$$E^{OB} = \Delta H^{cf} + E^{zp} - \Delta H^{ef} \quad (3)$$

Here E^{OB} is the over-binding energy, ΔH^{cf} is the theoretical formation enthalpy, E^{zp} is the calculated zero-point energy, and ΔH^{ef} is the experimental value for formation enthalpy.

TPD is used to derive the activation energy of atoms on the surface of the material. Thus, this derived activation energy is considered to be the actual value and is used as a reference for the calculated energy. This procedure allows a comparison to be made between the GGA+U determined activation energy and the empirically derived energy. However, to obtain these activation energies from desorption temperatures, one must first consider the kinetics equation for reaction rates as seen in Eq. (4).[11] This equation will be used to describe all the TPD peaks found in this work, most second but some first order, and is shown as a second order equation as it is dependent on the surface coverage.[11] Small shifts in the desorption peak are shown between first and second order reactions with the same binding energy stemming from this surface dependence. Note that since desorption rates are

a kinetic process and not a thermodynamic property the kinetic barrier accurately describes the activation energy.

$$R(t) = \nu N(t) e^{-\frac{E_b}{k_B T(t)}} \quad (4)$$

where R(t) is the reaction rate, T(t) is the temperature as a function of time and the ramp rate ($T(t) = T_0 + \alpha t$), E_b is the activation energy, k_b is the Boltzmann constant, ν is the frequency of vibration, and N(t) is the number of molecular interactions per site for a reaction. N(t) is hence a function of the reaction rate integral, or the total number of adsorbed molecules. Thus, for desorption reactions where each site contains and releases only one molecule (environment during the reaction does not contain the molecules in the reaction) we can assume $\frac{dN(t)}{dt} = -R(t)$. Therefore, one can obtain the temperature dependent peaks through the local minimums and maximums found by taking the derivative of this reaction rate equation, Eq. (5), and solving for zeros:

$$\frac{\alpha E_b}{k_B T^2} = \nu e^{-\frac{E_b}{k_B T(t)}} \quad (5)$$

Lastly, the energies calculated were at 0 K thus bringing the zero-point energies (ZPE) into consideration. These energies were considered for all molecular desorption and over-binding calculations. For large supercells and their formation energies, these ZPE values have been proven to be negligible.[12,13]

3.3 Results and Discussion

3.3.1 X-Ray Diffraction and Rietveld Refinement

XRD was carried out on each sample to determine the crystalline phase. The XRD patterns are shown in Figure 3.1 for all eight samples: $SmMn_2O_5$, $PrMn_2O_5$, YMn_2O_5, $GdMn_2O_5$, $LaFeO_3$, $LaMnO_3$, $SmCoO_3$, and CeO_2 respectively. Figure 3.1 shows all the unit cell refinement data and

their corresponding fitting values. The results of the unit cell refinements done for each XRD spectrum has identified phase purities of 95% or greater for all samples when referenced against competing binary and other ternary oxides.

The unit cell refinement process was additionally used to calculate the average crystallite size. Although the crystallite size and particle size do not go hand in hand, it is not possible to have a large crystal with small particles. This is useful as it gives insight to the surface area, a material with larger particles will have less surface area for the same total mass. This is not critical for this experiment, however, it is important to have some understanding of the surface area, since a material with very low surface area may not produce enough gas phase molecules when heated for the RGA to measure. Note that broader peaks tend to resemble smaller crystallite sizes via the Scherrer relationship. The calculated average crystallite size is listed in Figure 3.1.

In addition to crystallite size, each sample had multipoint Brunauer–Emmett–Teller (BET) physisorption performed using N_2 at 77 K to identify the specific surface area (SSA). The process was carried out in an Autosorb iQ analyzer (Quantachrome Instruments). 200 mg of each sample was outgassed at 80 °C for 30 minutes followed by 300 °C for 2 hours under vacuum. The relative pressure (P/P_0) range was 0.05 to 0.35. The SSA values are also found in Figure 1.

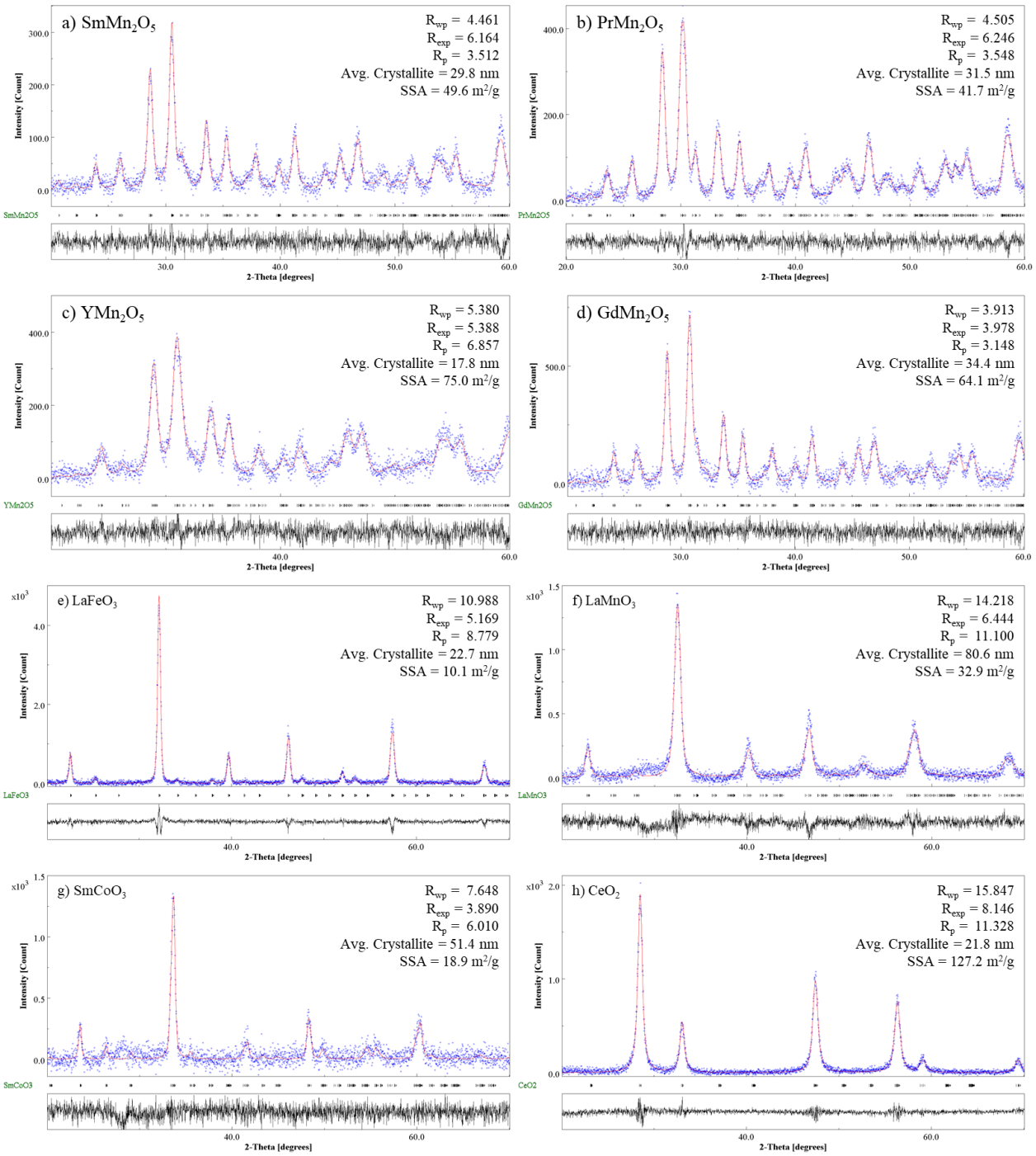

Figure 3.1. XRD spectra for a) $SmMn_2O_5$, b) $PrMn_2O_5$, c) YMn_2O_5, d) $GdMn_2O_5$, e) $LaFeO_3$, f) $LaMnO_3$, g) $SmCoO_3$, and h) CeO_2. The blue data points represent the experimental data while the red curve represents the refinement results. The fitting values are listed in black in each spectra's upper right corner along with the calculated crystallite size and specific surface area (SSA).

3.3.2 Temperature Programmed Desorption

Oxygen TPD was performed on all the samples to identify the surface oxygen activation energies and desorption peak temperatures. Given a specific desorption temperature peak and temperature ramp rate, the activation energy of that molecule on the material surface can be calculated for that peak using Eq. (5). However, since some noise exists in the TPD data, due to a smaller signal to noise ratio caused by the small partial pressure of surface oxygen, the data was smoothened, using a written program in Mathematica, and plotted to better identify the peak locations. Figure 3.2 shows the oxygen TPD spectrum for each material. Lastly, the activation energies for each temperature peak, derived with Eq. (5), are listed in Table 3.1 along with the peak temperature locations.

Furthermore, note that in each TPD spectrum, only the qualitative peak location matters, and that the quantitative pressure value between materials does not matter as different amounts of a sample may be needed to identify the surface oxygen based on the different surface areas of the materials. Therefore, some materials may cause an overall higher or lower oxygen pressure signal due to the sample having a large or small surface area respectively. However, the different relative peak magnitudes for the same material do give some insight to where the oxygen comes from. Furthermore, the decrease in oxygen pressure at the beginning of some of the TPD runs is noted. This is explained as coming from material amount and porosity. More material and pore volume will cause a longer evacuation time of gas from the chamber leading to initial decrease. This slope is consistent during the entire He pretreatment following oxygen exposure.

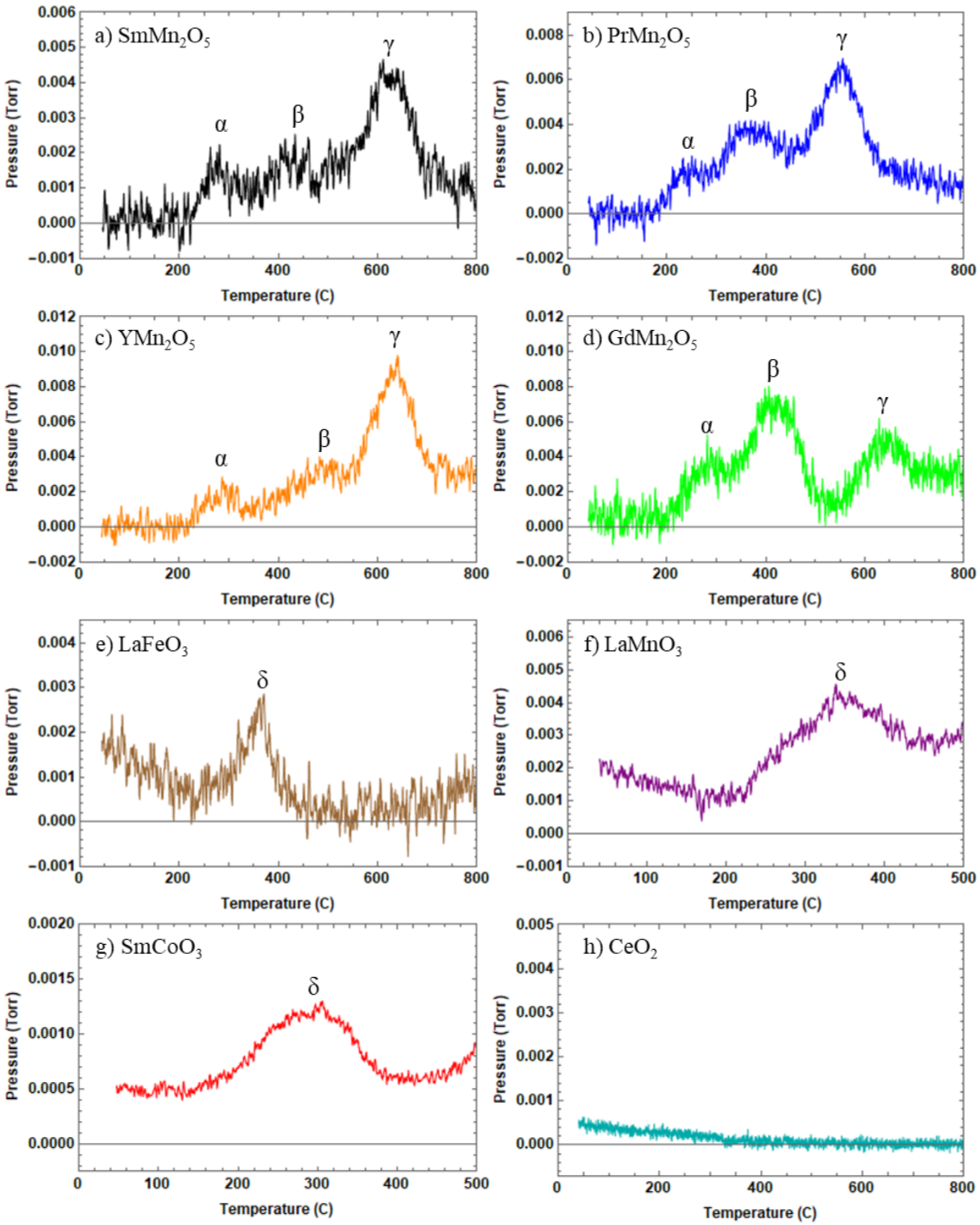

Figure 3.2. O_2 TPD plots are shown for a) $SmMn_2O_5$, b) $PrMn_2O_5$, c) YMn_2O_5, d) $GdMn_2O_5$, e) $LaFeO_3$, f) $LaMnO_3$, g) $SmCoO_3$, and h) CeO_2. These plots are smoothened to better identify the peak positions. The surface oxygen peaks for the $SmCoO_3$ and $LaMnO_3$ phases only go to 500 °C to avoid the large surface reconstruction peak.

Some of the broader peaks observed in Figure 3.2 may be indicative of multiple reactive sites, some which may stem for step edges between surface facets or other surfaces which may exist in smaller fractions. This may result in some error in the exact location of the TPD peak shifting the calculated activation energies.

Table 3.1. Oxygen desorption temperatures for each material are shown in degrees Celsius (°C) along with the activation energy in electron volts (eV) for each temperature calculated using Eq. (5).

Material	Oxygen Peak α (°C)	Activation Energy (eV)	Oxygen Peak β (°C)	Activation Energy (eV)	Oxygen Peak γ (°C)	Activation Energy (eV)
$SmMn_2O_5$	280	1.64	427	2.09	624	2.70
$PrMn_2O_5$	242	1.53	363	1.90	556	2.49
YMn_2O_5	295	1.69	486	2.28	636	2.74
$GdMn_2O_5$	285	1.66	426	2.09	645	2.77
$LaFeO_3$	371	1.92				
$LaMnO_3$	351	1.86	671	2.85		
$SmCoO_3$	300	1.71	670	2.85		
CeO_2	>800	>3.24				

These TPD results show unique oxygen peaks for each material. Although, the formation energy for all low index surfaces was examined, the perovskite and mullite-type oxide phases showed only one stable surface, being in good agreement with literature.[14,15] All mullite-type oxides have a characteristic three peaks (α, β, γ) in the oxygen TPD experiments. Mullite-type oxides are unique in that each oxygen TPD peak comes from a specific desorption site. The mullite surface and corresponding desorption sites are shown in Figure 3.3(a). For the perovskite phases, there is only one surface oxygen peak (δ) as expected from the symmetric surface atomic structure. This oxygen peak can come from any one of the lattice oxygen, such as the one labeled δ in Figure 3.3(b), provided there is only one desorbed oxygen per unit cell and they do not share an adjacent

metal ion. Additionally, $SmCoO_3$ and $LaMnO_3$ have a second, higher temperature, peak which is significantly larger than the first. Here, only the first peak comes from the surface while the larger peak (above 600 °C for both materials) comes from the bulk. The peaks produced from bulk oxygen produces a significantly stronger oxygen signal.[16] Surface desorbed peaks will often be similar in magnitude, within the same sample, since each peak represents one site per one or two unit cell surfaces. However, since a huge majority of the oxygen atoms, or all atoms in general, for a given sample are found in the bulk rather than the surface, bulk desorption for both perovskite samples release multiple oxygen simultaneously per surface unit. This bulk oxygen release produces a high partial pressure of oxygen at that temperature and a broad peak in the TPD spectrum. These peaks are shown in Figure 3.4.

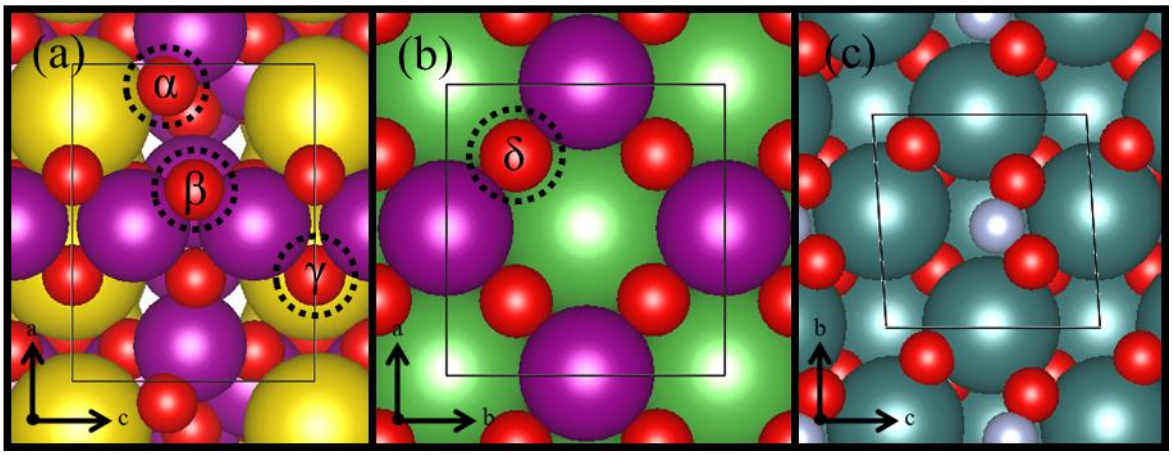

Figure 3.3. The oxygen desorption sites for (a) all mullite-type oxides are shown on the dominant (010) surface and (b) for all perovskite oxides on the (001) surface. For CeO_2, NO_x adsorption sites (c) are shown on its (100) surface. The A-site for mullite is represented by the yellow balls while the A-site for perovskite is represented by the light green balls. oxygen is represented as red, manganese as purple, nitrogen as light blue, and cerium as gray.

The full oxygen TPD scans are shown in Figure 3.4 for both $LaMnO_3$ and $SmCoO_3$. The larger peak comes from surface reconstruction and bulk oxygen.[16] As mentioned previously in this section, the peak magnitude shows some insight to the desorption location. Within the same spectra

we can draw conclusions as to whether a peak comes from the surface or the bulk of the material. We can assume that every unit cell has the same binding energy for a specific atom at a specific site. Therefore, significantly larger peaks would come from the bulk of the crystals rather than the surface. This is due to the availability of surface oxygen sites when compared to bulk oxygen sites.

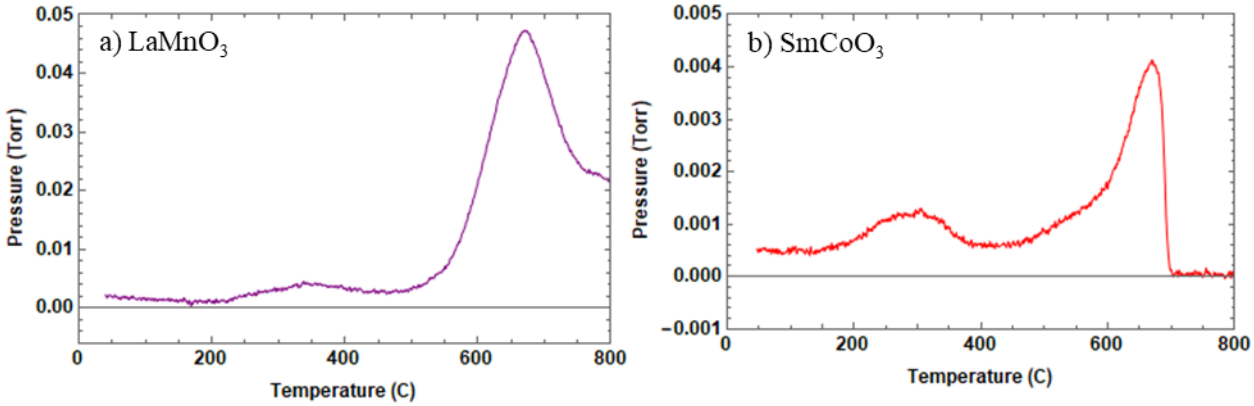

Figure 3.4. Full oxygen TPD profiles shown for (a) $LaMnO_3$ and (b) $SmCoO_3$.

The eighth sample, sample h) CeO_2, is unique in that no oxygen peaks are observed during TPD due to a lack of oxygen desorption from the sample surface. This is due to the more strongly bonded lattice oxygen in CeO_2 than that of the perovskite and mullite materials studied in this work. Other work has also shown CeO_2 to have the same characteristic behavior.[17] To overcome this limitation in investigating CeO_2 surface properties, NO TPD was performed to determine the surface chemistry. The CeO_2 NO TPD plot can be found in Figure 3.5 along with the activation energies and peak positions in Table 3.2. NO TPD was used identically to the oxygen TPD from the other samples to create the CeO_2 surface. The desorption energies were calculated using Eq. (5) and the nitrite locations, NO adsorption/desorption sites, for CeO_2 are shown in Figure 3.3(c).

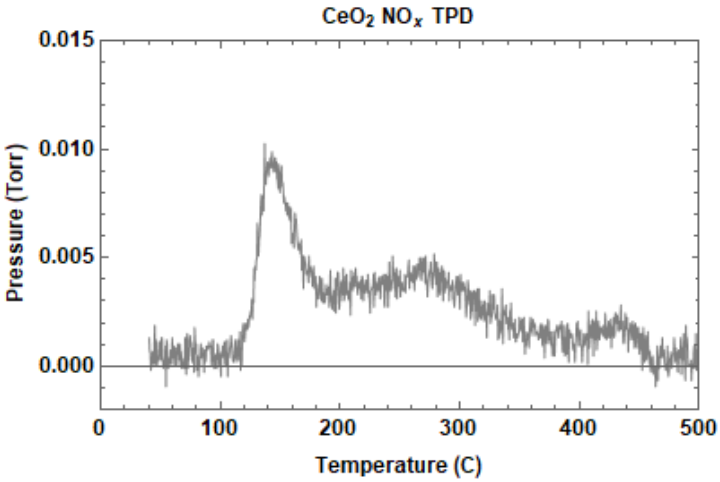

Figure 3.5. NO TPD for CeO_2.

The NO_x TPD performed on CeO_2 showed only the CeO_2 (100) surface to have consistent nitrite bonding responsible for the first peak. DFT calculations showed this first peak to come from bidentate nitrite formation on the (100) surface while the second broad peak comes from NO_x species adsorbed in vacancies on the (111), (110), and (100) surfaces resulting in the poor peak definition.

Table 3.2. NO desorption temperature peak, TPD determined binding energy, and DFT calculated binding energy for CeO_2.

Measured NO_x Peak Temperature (°C)	TPD Determined Activation Energy (eV)	DFT Determined Activation Energy (eV)
155	1.25	1.23

This surface construction process, further discussed in section 3.3.4., showed the perovskite materials to have a (001) exposed surface, mullite-type oxides to have the (010) exposed surface, and CeO_2 to have its (100) surface present, Figure 3.3 This is in good agreement with surface studies for each material.[14,15,18] Although the NO adsorption-desorption process for CeO2 was only observed on the (100) surface, both the stable (111) and (110) surfaces were also examined. DFT showed that the formation energy of NO on the (111) and (110) surfaces was extremely weak,

showing mainly a physical interaction between the surface and the NO molecule. This is in part due to the (111) and (110) being the closer packed, and dominant, surfaces which tend to be more inert. This may also be responsible for the weaker NO signal observed in TPD.

3.3.3 Molecular Over-Binding

Molecular over-binding must be considered before modeling the CO and NO reaction mechanisms on perovskite oxides and mullite-type oxides, as both GGA and HSE modeling showed issues with over-binding for all covalently bonded molecules. We found that NO_x, SO_x, CO_x, and N_2 and O_2 all had over-binding issues when using the GGA functional. To fix this issue, a relationship between the over-binding and charge density and bond length was analyzed. This analysis was done by measuring the charge density in a fixed spherical volume and relating that charge density to the over-binding energy in various molecules. The over-binding in molecules considered in this work is listed in Table 3.3 while the charge and over-binding relationship for NO_x molecules and surface adsorbed NO_x species is described by Figure 3.6. For the surface nitrite molecules, the charge density was identical to HNO_2, thus the over-binding was taken to be 1.29 eV. For the bridging nitrate, the charge was between HNO_3 and NO_3. Using the fractional difference in charge, the bridging nitrate had 2.12 eV of over-binding on the $PrMn_2O_5$ surface. This method was not employed for the CO oxidation process considered in this work on perovskite oxides since the over-binding of surface carbonate and CO_2 is similar to molecular CO_2. This is expected as carbonate and all CO_2 species contain the same charge state of carbon, 4+.

Table 3.3. Over-binding for all molecules considered in this work. For molecules with bonds between each oxygen, oxygen and nitrogen, oxygen and carbon, and oxygen and sulfur, only these bond lengths are listed in column 2 from the left. For instance, in H_2O_2 the calculated H – O bond length is not given. The DFT calculated formation enthalpy is in the 3rd column, the zero-point energy calculated by DFT is in column 4, the empirical formation enthalpy from the NIST-JANAF Tables of Thermochemistry is in the 5th column from the left, and the corresponding over-binding is listed in the far-right column. Note that Na-O bonds have under-binding, this was used when considering the over-binding in sodium carbonate.

Chemical Formula	Bond Distance (Å)	DFT Formation Enthalpy (eV)	Zero-point Energy (eV)	NIST-JANAF Value (eV)	Over-Binding (eV)
O_2	1.23414 Å	-6.10 eV	0.10 eV	-5.12 eV	-0.88 eV
H_2O_2	1.48190 Å	-12.10 eV	0.76 eV	-10.94 eV	-0.40 eV
H_2O	0.97252 Å	-10.10 eV	0.59 eV	-9.51 eV	0.00 eV
H_2	0.75527 Å	-4.53 eV	0.31 eV	-4.49 eV	0.27 eV
OH	0.98754 Å	-4.73 eV	0.24 eV	-4.40 eV	-0.09 eV
HO_2	1.34526 Å	-8.37 eV	0.38 eV	-7.30 eV	-0.69 eV
N_2	1.11481 Å	-10.39 eV	0.16 eV	-9.76 eV	-0.47 eV
NO	1.17036 Å	-7.27 eV	0.12 eV	-6.51 eV	-0.64 eV
NO_2	1.21287 Å	-11.49 eV	0.24 eV	-9.62 eV	-1.63 eV
NO_3	1.25144 Å	-14.57 ev	0.34 eV	-11.75 eV	-2.48 eV
N_2O_3	1.15785 - 1.93213 Å	-19.62 eV	0.47 eV	-16.50 eV	-2.64 eV
N_2O_5	1.20147 - 1.55662 Å	-26.98 eV	0.71 eV	-22.42 eV	-1.93 eV
HNO	1.23889 Å	-9.15 eV	0.44 eV	-8.61 eV	-0.1 eV
HNO_2	1.18414 - 1.46802 Å	-14.82 eV	0.54 eV	-12.99 eV	-1.29 eV
HNO_3	1.20981 - 1.44449 Å	-18.73 eV	0.70 eV	-16.08 eV	-1.95 eV
H_2SO_4	1.42742 - 1.61124 Å	-27.33 eV	1.03 eV	-22.18 eV	-4.12 eV
SO	1.49583 Å	-6.31 eV	0.08 eV	-2.51 eV	-3.72 eV
SO_2	1.44751 Å	-12.39 eV	0.20 eV	-8.17 eV	-4.02 eV
SO_3	1.43667 Å	-16.46 eV	0.33 eV	-11.72 eV	-4.41 eV
CO	1.14338 Å	-11.53 eV	0.14 eV	-11.11 eV	-0.28 eV
CO_2	1.17662 Å	-17.83 eV	0.31 eV	-16.56 eV	-0.96 eV
Na_2CO_3	1.30150 Å	-29.24 eV	0.12 eV	-28.93 eV	-0.89 eV
Na_2O	2.42274 Å	-8.50 eV	0.13 eV	-9.07 eV	0.70 eV
NH_3	1.00425 Å	-12.86 eV	0.94 eV	-12.00 eV	0.08 eV

The over-binding for surface nitrites and nitrates were calculated using a linear approximation from molecular nitrate over-binding. Here NO, NO_2, NO_3, HNO_2, and HNO_3 were all considered. The electron density versus radius of each species is plotted with each surface nitrite and nitrate in Figure 3.6. The difference in electron density between two molecules was used to make a linear fit to over-binding and electron density. From this figure, it is shown that Pr monodentate and bidentate nitrites have over-bindings very similar to HNO_2. It is also shown that the Pr bridging and monodentate nitrate have over-binding values that align with HNO_3. However, for the bridging lay down species mentioned in step 5 of the reaction process (Figure 3.11), the over-binding lies somewhere in between HNO_3 and NO_3. Using a linear approximation for the over-binding between HNO_3 and NO_3, the bridging nitrate shows a binding energy which is 2.12 eV too large. Note that bond distance cannot be used for surface nitrites and nitrates due to bond stretching when adsorbing on the surface.

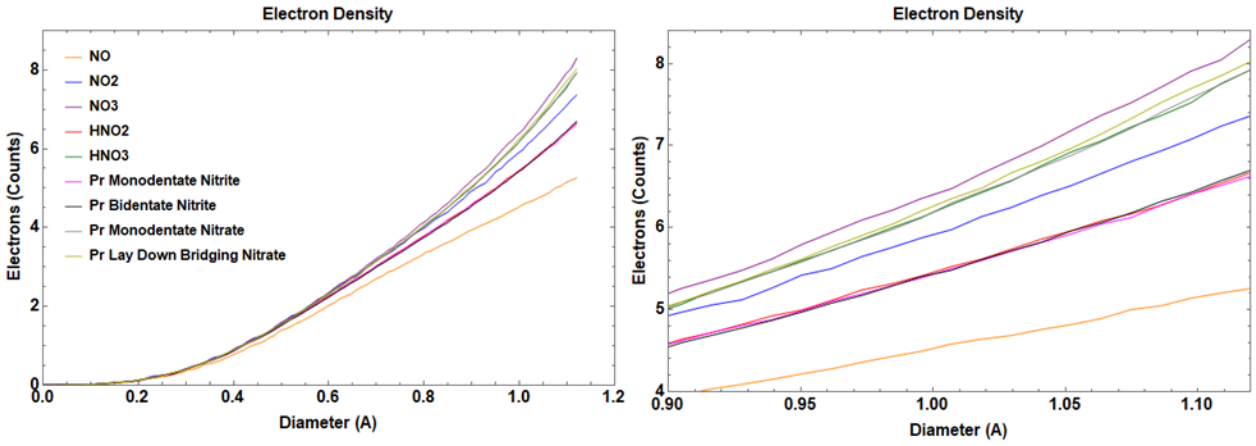

Figure 3.6. Plot of electron density with radius for all NO_x species considered in this work.

3.3.4 Surface Construction and Characteristics Using DFT

As mentioned in section 3.3.2, all mullite materials were found to have an active (010) surface, all perovskite materials were found to have an active (001) surface, and CeO_2 showed

adsorption/desorption of NO on its (100) surface. The oxygen desorption/adsorption sites are shown in Figure 3.3. These surfaces were found through a combination of processes. The binding energy of oxygen for all stable low index surfaces was calculated along with the surface formation energy. In addition, this data was compared to the observed stable surfaces for each material found in literature.[14,15,18] This yielded the surface terminations used in this study. Furthermore, oxygen and metal vacancy energies were calculated by removing and adding atoms to the surface and recalculating the formation energies of that surface.[19] Surfaces in which the vacancy energy was less than the reference energy, molecular O_2 for oxygen along with bulk Mn and Sm metal, were the most stable surfaces. This vacancy energy process yields the surface morphology found in Figure 3.3. Note that this vacancy energy is the binding energy for oxygen given the same reference and must match our experimental data.

DFT calculations were performed to determine the exposed surfaces and to match the surface (in this case, metal – oxygen) binding energies. For each desorption process, NEB (nudged elastic band) was performed to identify the activation energy. It should be noted that the desorption process for O_2 is direct in such a way that the activation energy is equal to the binding energy of the surface oxygen for all β, γ, and δ oxygen sites. This is due to the binding energy being larger than the migration barrier. However, for the α site, the activation energy is higher. In addition to this absolute binding and activation energy, the temperature difference between TPD peaks correlates to an activation energy difference through Eq. (5) which must match the corresponding DFT calculated energy difference. Additionally, the number of peaks in each TPD spectrum must match the number of different desorption sites calculated in DFT. This greatly reduces the number of surfaces likely to be present.

Furthermore, since all the materials in this study involve localized *d* or *f* shell orbitals, an effective interaction parameter, U_{eff}, must be applied to correct for their strong correlation interactions in DFT modeling. One initial concern was that some materials have multiple oxygen peaks and thus multiple binding energies, which could cause issues when trying to match a single Hubbard U_{eff} for the entire material surface sites. However, we found that a single U_{eff} generally matches to all the peaks of a specific material. This finding simplifies the analysis, as it signifies that the over-binding in *d* and *f* orbitals is material but not site dependent. Furthermore, applying the U_{eff} correction that best modeled the bulk properties for each material, often misrepresented the surface interaction energies.[7,20] Additionally, U_{eff} values are generally shown to be element specific in literature (e.g., 3.9 eV for Mn).[21] However, in order for the material surfaces to reliably explain the given reaction mechanism, the U_{eff} values must differ slightly between the same elements in different surface environments. Hence, the U_{eff} values are adjusted to best fit the surface oxygen binding energies over multiple surfaces (e.g., 4.5 eV for Mn on $SmMn_2O_5$ surface). The Bulk U_{eff} values for each element along with the U_{eff} values derived in this work are listed in Table 3.4.

Table 3.4. Desorption energies for each surface oxygen peak. NEB desorption energies are only shown if they are the reaction barriers. The bulk U_{eff} values are derived from the oxidation energies for each metal oxide while the surface U_{eff} values are derived from the oxygen binding energies calculated using TPD. Note that CeO_2 U_{eff} was calculated from NO TPD since there were no peaks in the oxygen TPD.

Material		U_{eff} Values (eV)	Oxygen 1 Formation Energy (eV)	Oxygen 1, NEB, Reaction Barrier (eV)	Oxygen 2 Activation Energy (eV)	Oxygen 3 Activation Energy (eV)
$SmMn_2O_5$	Bulk U_{eff}	3.9[21] for Mn 0[21] for Sm	1.38	1.91	2.27	3.01
	Surface U_{eff}	4.5 for Mn 0 for Sm	1.15	1.68	2.10	2.78

Table 3.4, continued

$PrMn_2O_5$	Bulk U_{eff}	3.9[21] for Mn 0[21] for Pr	1.42	2.17	2.27	2.97
	Surface U_{eff}	5.3 for Mn 0 for Pr	0.89	1.49	1.87	2.45
YMn_2O_5	Bulk U_{eff}	3.9[21] for Mn 0[21] for Y	1.25	1.77	2.28	2.89
	Surface U_{eff}	4.0 for Mn 0 for Y	1.20	1.73	2.24	2.76
$GdMn_2O_5$	Bulk U_{eff}	3.9[21] for Mn 0[21] for Gd	1.32	1.86	2.33	3.09
	Surface U_{eff}	4.6 for Mn 0 for Gd	1.07	1.68	2.12	2.82
$LaFeO_3$	Bulk U_{eff}	5.3[21] for Fe 0[21] for La	1.80			
	Surface U_{eff}	4.8 for Fe 0 for La	1.93			
$LaMnO_3$	Bulk U_{eff}	3.9[21] for Mn 0[21] for La	2.40			
	Surface U_{eff}	5.5 for Mn 0 for La	1.87			
$SmCoO_3$	Bulk U_{eff}	3.32[21] for Co 0[21] for Sm	1.13			
	Surface U_{eff}	2.3 for Co 0 for Sm	1.71			
CeO_2	Bulk U_{eff}	0[21] or 4.5[22] for Ce	3.83 or 3.48			
	Surface U_{eff}	6.0 for Ce	3.38			

The comparison of three desorption energy values (the experimentally determined binding energies, Exp, DFT binding energies using bulk U_{eff}, and DFT binding energies using surface determined U_{eff}) is made in Figure 3.7 for each TPD peak of each material. The bulk U_{eff} values are 0 eV for Sm, Pr, Y, Gd, and La, 3.9 for Mn, 3.32 eV for Co, 5.3 eV for Fe, and 0 and 4.5 eV for Ce.[21,22] The bulk U_{eff} values are derived from the oxidation energies for each metal oxide.[6] The surface U_{eff} values are derived from the oxygen binding energies calculated using TPD. Note that

for the perovskite and mullite phases, no A-site element is found to be on the most stable surfaces. This surface feature means a bulk U_{eff} correction can be used accurately for these A-site elements in both mullite-type and perovskite material surfaces. Thus, only the B-site U_{eff} is altered between each material surface. The varying U_{eff} values are listed inside each bar chart for each material along the element it was used for.

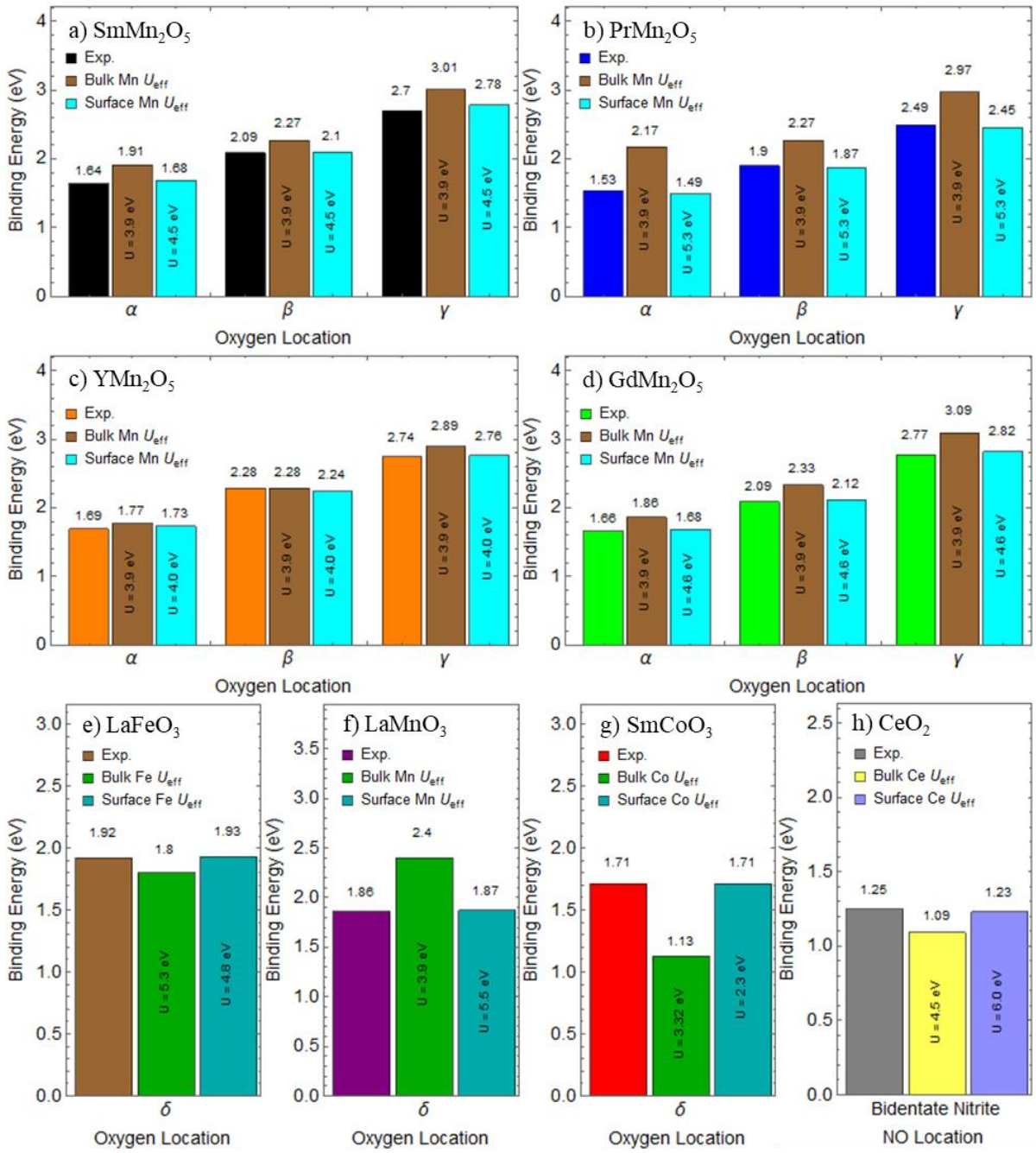

Figure 3.7. Oxygen Desorption energies for each surface oxygen is listed by location for a) $SmMn_2O_5$, b) $PrMn_2O_5$, c) YMn_2O_5, d) $GdMn_2O_5$, e) $LaFeO_3$, f) $LaMnO_3$, and g) $SmCoO_3$. Note that CeO_2 U_{eff} was calculated from NO TPD since there were no peaks in the oxygen TPD. Thus, the NO desorption energy is listed for h) CeO_2. Exp. is the experimentally determined binding energy, calculations done with the bulk U_{eff} are listed as bulk element U_{eff} for a particular element in that material, the surface U_{eff} are the calculations done with the U parameter found to best fit the material and its surface properties.

Lastly, it is important to note that all the NO and O_2 activation barriers are equivalent to their absolute binding energies, due to their simplistic molecular structure and desorption, except for the oxygen desorption barrier at α (Oxygen 1 in Table 3.4) for mullite-type oxides. This peak comes from the surface migration barrier of single atom oxygen to form O_2 dimers. The largest barrier for oxygen 1 is not in its desorption from its lattice site but in its migration to forming surface O_2 before desorbing from the surface. This unique feature of the α sites is due to the fact that the surface reaction barrier in forming the surface bound O_2 is larger than the binding energy of the single atom oxygen to the surface. Because of this energy difference, NEB calculations were performed to identify the desorption energies from the α sites. This migration energy is listed separately from the binding energy of the first oxygen in Table 3.4.

Furthermore, as listed in theoretical methodology, over-binding exists in oxygen molecules. Because of this strong electron correlation effect, we must address the oxygen dimers that form on the mullite surface before desorption. Since some of the binding energy comes from the oxygen metal bonds and some of the binding energy coming from the oxygen to oxygen bonds, the over-binding changes depending on the bonding environments. We found that a solution to this variability is relatively simple. Since bond strength can be estimated by bond length, the over-binding between oxygen atoms for other oxides and superoxides can be calculated and applied to the oxygen dimer, migration barrier, of the mullite materials. This is done by calculating the formation energy of molecules such as H_2O_2 and HO_2 and subtracting the empirically known formation energy. Note that H-O bonds are nearly exact as seen by OH and H_2O in Table 3.3. The bond distance can be measured from the relaxed structure in DFT, Table 3.3 for the molecules and

Table 3.5 for the dimers, and a linear approximation can be made between the bond distance and the over-binding amount, seen in Figure 3.8. This over-binding can then be subtracted off the oxygen dimer. The results from this technique yielded accurate desorption energies for each reaction which involved an oxygen dimer. The over-binding values and bond lengths calculated for each mullite material is listed in Table 3.5.

Table 3.5. Oxygen dimer bond lengths and over-binding values for each mullite material used for NEB calculations.

Material Dimer	Bond Distance	Over Binding
$SmMn_2O_5$ Dimer	1.41038 Å	-0.55 eV
$PrMn_2O_5$ Dimer	1.38454 Å	-0.61 eV
YMn_2O_5 Dimer	1.42188 Å	-0.53 eV
$GdMn_2O_5$ Dimer	1.41856 Å	-0.53 eV

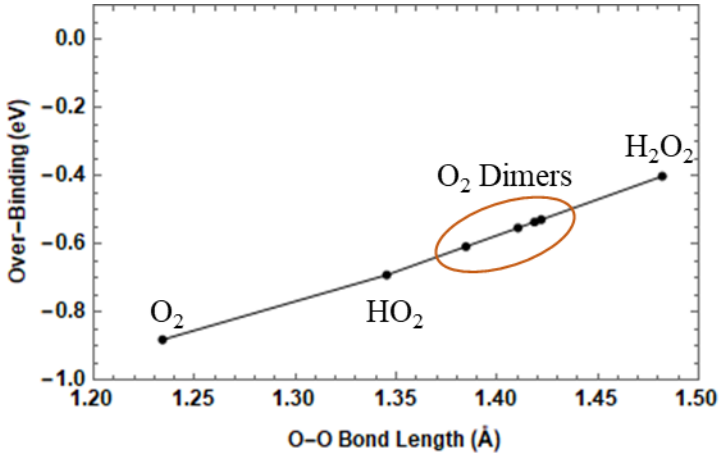

Figure 3.8. Relationship between oxygen-oxygen bond length and over-binding used to approximate the corresponding mullite O_2 dimer over-binding. It should be noted that the references used to calculate the O-O dimer over-binding on the surface were all molecules with O-O bonds. These molecules give the most accurate depiction of the surface dimer over-binding as they are chemically similar. Thus O_2, HO_2, and H_2O_2 references are shown above.

3.3.5 Reaction Modeling

Following the surface construction, CO oxidation was modeled on all three perovskites, $LaFeO_3$, $LaMnO_3$, and $SmCoO_3$, and compared to the CO/CO_2 TPD reported in literature to demonstrate

the reliability of this method. CO oxidation was chosen for perovskite oxides due to the abundance of data on this reaction mechanism that can be found in literature.[23-26] $LaFeO_3$ has a CO_2 peak at 150 °C.[23] Reduced $LaMnO_3$, at 300 °C, showed a CO peak at 102 and 625 °C and fresh $LaMnO_3$ had a CO_2 peak at 341 °C.[24,25] Lastly, $SmCoO_3$ reduced at 500 °C has been reported to have a CO peak at 575 °C.[26] Since all the reduction temperatures were below the threshold for surface reconstruction for each material, a reduced surface can be made and modeled using DFT. Using the surfaces created with oxygen TPD, a reduced surface can easily be made by removing unfavorable surface oxygen atoms. Each of the four surface models were kept consistent with our oxygen TPD results such that if a sample was reduced at 300 °C in H_2 gas, the surface constructed in DFT was reduced by removing unstable oxygen exposed to H_2 on the surface at binding energies corresponding to 300 °C. The respective CO oxidation mechanism was then modeled by placing CO on this model surface. The corresponding binding energies can be seen in Table 3.6 for the CO_x mechanisms. The calculated binding energies using the constructed surface from oxygen TPD matched well with reported experimental values. This is shown for all four perovskite surfaces modeled in the work. The CO oxidation process is further illustrated in Figure 3.9. This process is simple compared to the NO oxidation process and consequently has only one main CO_2 peak in TPD studies. The process follows four steps. First is the adsorption of CO onto the perovskite surface to form a carbonate with two oxygen atoms being shared with the surface. This is followed by a rotation to a standing CO_2, step 3, and then an easy desorption from the surface shown by the small 0.13 eV binding energy in step 4. All fresh samples follow this process, however, since $SmCoO_3$ showed weaker oxygen surface bonds, the carbonate species was raised up higher from the surface.

Table 3.6. CO_x binding energies determined from DFT (Left) and Eq. (5) with CO_x TPD (Right) for each perovskite compound.

Material	Calculated Binding Energy for CO_x	TPD Binding Energy for CO_x[23-26]
$LaFeO_3$ – Fresh	1.36 eV/CO_2	1.28 eV/CO_2
$LaMnO_3$ - Fresh	1.75 eV/CO_2	1.83 eV/CO_2
$LaMnO_3$-Reduced	1.09, 2.78 eV/CO	1.12, 2.76 eV/CO
$SmCoO_3$-Reduced	2.73 eV/CO	2.61 eV/CO

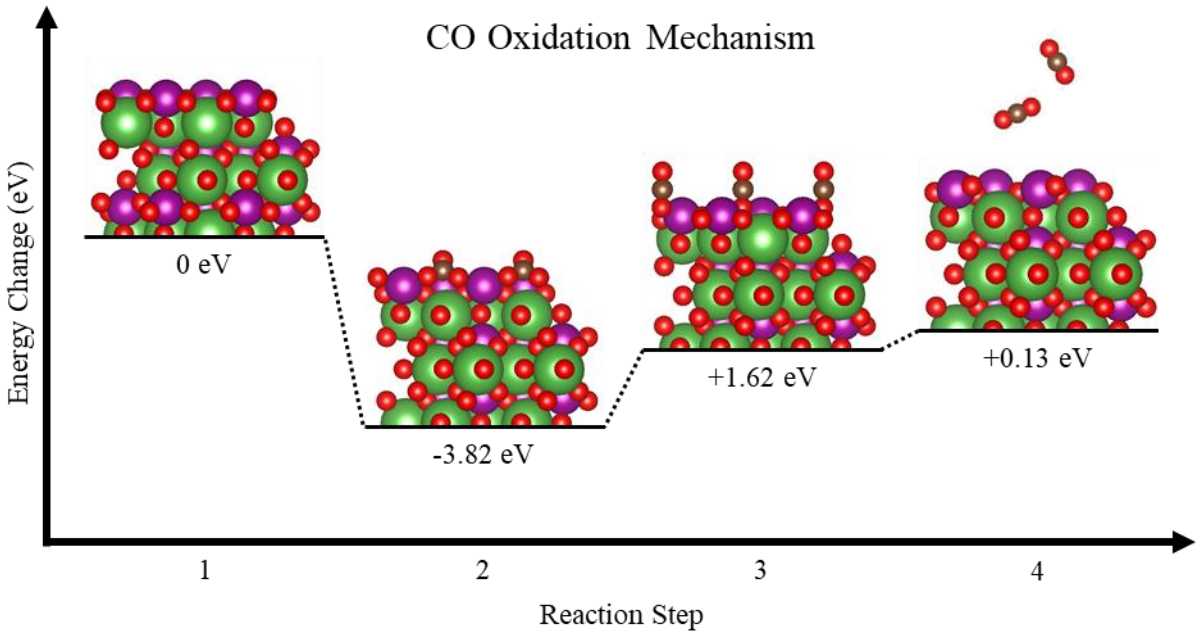

Figure 3.9. CO oxidation mechanism on a fresh $LaMnO_3$ perovskite surface. La is represented by green balls, Mn by purple balls, O by red balls, and C by the brown balls.

Furthermore, NO TPD was performed on $PrMn_2O_5$ mullite-type oxide to verify the surface construction reliability as well as model the NO reaction process within this work. NO was chosen for mullite-type oxides due to the high NO oxidation performance and well studied mechanism.[27,28] The TPD data is shown in Figure 3.10. Unlike the CO oxidation mechanism on perovskites, the NO oxidation process on mullite-type oxides is quite complex. This is shown by the three NO peaks in the TPD results, which are located at 130, 193, and 347 °C (similar to oxygen TPD but at lower temperatures).

DFT calculations were also used to study this NO oxidation process. Using the data gathered from oxygen TPD, the NO oxidation mechanism was modeled on $PrMn_2O_5$. The DFT results proved to be consistent with the TPD data as shown by the binding energies in Table 3.7. These different DFT binding energies come from desorption locations shown in the NO adsorption and desorption processes in Figure 3.11. NO molecules are adsorbed to the Mn rich (010) surface where they form three types of nitrites, two bidentates and a monodentate as shown in step 2. This step is followed by the desorption of the monodentate nitrite (NO-1) resulting in the lowest temperature TPD peak. Half the bidentate locations are then desorbed, step 4 (NO-2), allowing for the rotation of the remaining bidentate nitrites to form a bridging nitrate. This rotation is not energetically favorable without the desorption of half the bidentate nitrites. This is due to the rotation barrier of the bidentate nitrite to bridging nitrate being equal to the desorption barrier for the bidentate nitrate. This step is responsible for the second NO peak seen in TPD. The final NO forms a laying down bridging nitrate between the chain and connection sites of the mullite-type oxides, seen in step 5. This nitrate can then be desorbed at around 350 °C causing the last NO (NO-3) peak. This multi-step mechanism yields three desorption energies which are consistent with those determined by TPD.

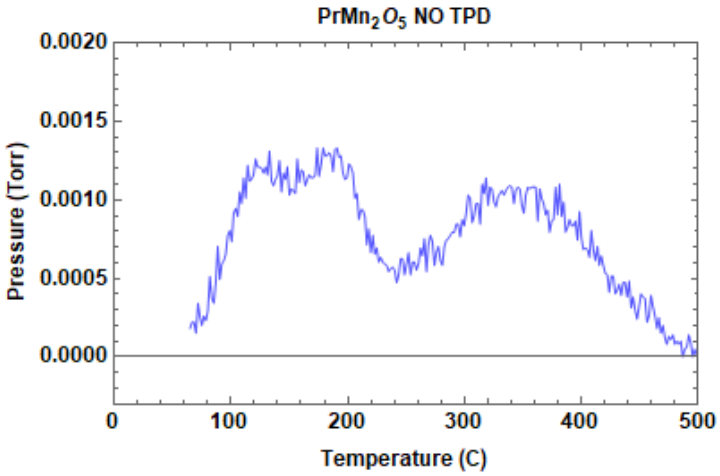

Figure 3.10. NO TPD for $PrMn_2O_5$ with peak positions located at 130, 193, and 347 C.

Table 3.7. NO binding energies for $PrMn_2O_5$ calculated by DFT (left) and through Eq. (5) with NO_x TPD (right).

NO Peaks	Calculated Binding Energy	TPD Binding Energy
NO-1	1.03 eV	1.18 eV
NO-2	1.24 eV	1.38 eV
NO-3	1.78 eV	1.85eV

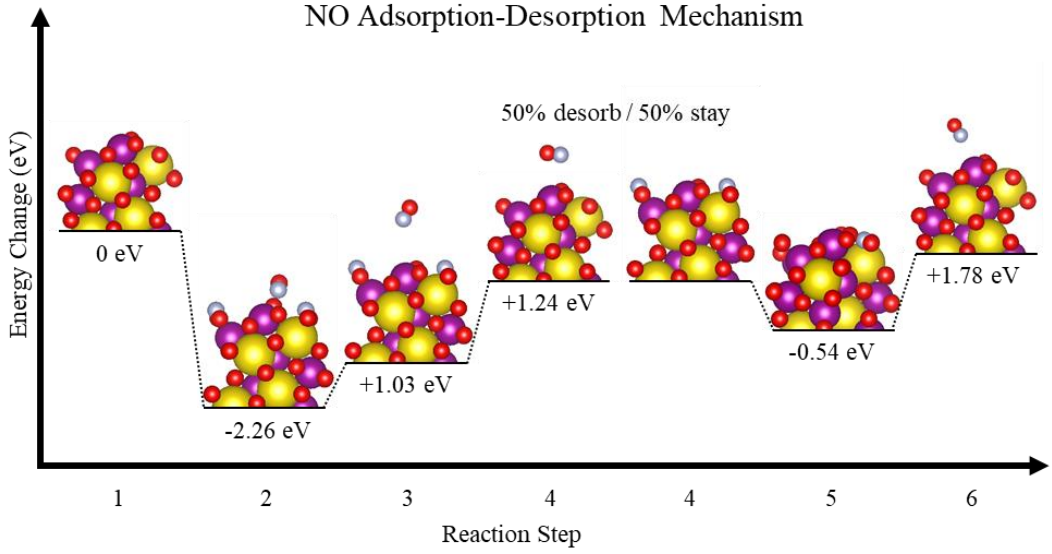

Figure 3.11. The NO adsorption-desorption mechanism on $PrMn_2O_5$ is shown above. Pr is represented by the yellow balls, Mn by the purple balls, O by the red balls, and N by the light blue balls.

Lastly, FTIR was performed to verify the surface nitrate species used in the DFT calculations, which is shown in Figure 3.12 and Table 3.8. The vibration modes for surface absorbed NO_x species where both experimentally determined and theoretically calculated. This data was used to help verify that the surface adsorbed NO_x species and calculated NO_x species were the same. As shown in in Table 3.8, both the experimental and theoretical vibration modes correlate closely.

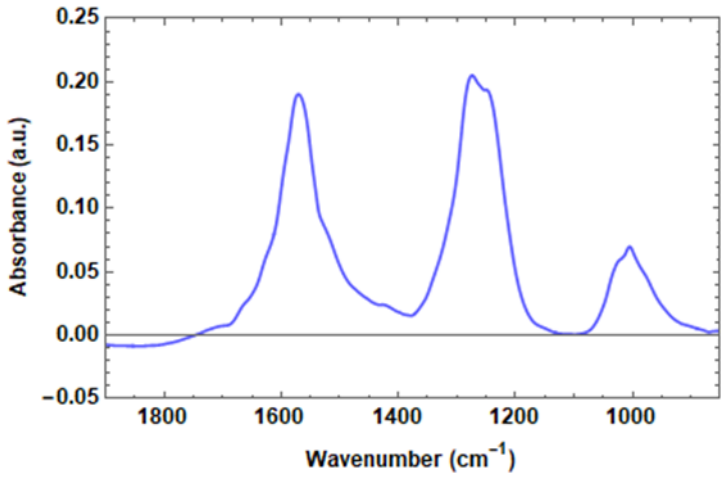

Figure 3.12. FTIR scan of $PrMn_2O_5$ at 40 °C after 7 min of 99.5% NO gas exposure.

Table 3.8. Observed NO_x vibrations states are listed in row 2 while the calculated vibration states for the most stable NO_x configuration on the surface are listed in row 3.

Nitrate	Vibration 1	Vibration 2	Vibration 3
Observed	1570 cm^{-1}	1250 cm^{-1}	1004 cm^{-1}
Calculated	1564 cm^{-1}	1143 cm^{-1}	968 cm^{-1}

3.4 Discussions of Drawbacks and Applications

The TPD process is reliable and accurate in determining binding energies using Eq. (5), however, minor issues do exist with this method. The attempt frequency, ν, is a constant commonly considered to be around 10^{13} s^{-1}. However, this may differ for different surface adsorbed molecules

and thus cause errors of up to 0.2 eV.[11] Furthermore, there are errors that arise from a low signal to noise ratio in the TPD plots. This noise is due to a very small partial pressure of gas coming from the surface. Additional errors in the TPD data stem from the broadness of some of the peaks which makes it hard to single out individual surface and reactive site contributions. It is worthwhile to note that the methodologies discussed in this work are for idealized cases where one active surface contributes to a vast a majority, if not all, of the catalytic activity. However, as shown in this work, some of the TPD peaks are broad making it difficult to identify all possible reaction sites. It is possible for various step edges, surfaces, and amorphous phases to all contribute to some degree to the broader TPD peaks shown in this work. It should also be said that the desorption of molecular species from the surface is modeled with the assumption that there is uniform surface coverage where the binding energy is consistent between similar sites. Small coverage dependent changes in the binding energy create small shifts in the TPD peak which are not considered.

Furthermore, conventional DFT simulation errors also exist in calculating molecule binding energies on a material surface. As mentioned before, over-binding exists in many covalently bonded molecules. This over-binding is estimated and corrected as best as possible for each environment. However, no ideal approximation can be made when using molecules or solids to derive surface adsorption energy and bonding characteristics. These issues lead to small deviations between the TPD and DFT binding energies: < 0.1 eV for oxygen TPD as shown in Figure 3.7, ~0.1 eV for CO_x TPD (Table 3.6), and < 0.15 eV for NO TPD (Table 3.7).

Although the peak locations are not in perfect agreement between the DFT and TPD data, they are consistent. Furthermore, the binding energy differences between DFT and TPD differ by no more than 0.2 eV, within typical DFT calculation errors. This agreement shows that the

mechanisms adopted in DFT for both the NO and CO surface mechanisms are consistent with the identified oxide surface structures. This agreement helps validate the use of TPD in creating the correct surface morphology for different materials. Additionally, DFT shows the same relationships between samples as TPD, e.g. the $GdMn_2O_5$ has higher oxygen binding energies then $SmMn_2O_5$ in both TPD and DFT. The NO and CO binding energies are also close showing a good relationship between the TPD and DFT data. This comparison verifies the surface chemistry model made with oxygen TPD and allows for accurate CO and NO oxidation mechanisms to be studied. This process can be used to reliably model surface reactions since both the CO and NO mechanisms matched up well with the TPD results.

This matching process is only applied to oxides in this work. This choice is due to the relative simplicity of using oxides (similarly for nitrides, sulfides, or hydrides) which allow the use of O_2, (correspondingly N_2, S_2, H_2) TPD without the adsorption of a gas. However, it may be applied to pure metals through the adsorption and desorption of molecules. This overall process of determining surface binding energetics thus has two main approaches: the first is the desorption of intrinsic surface oxygen, nitrogen, etc.; and the second is a molecular adsorption, that when heated will release those molecules at various temperatures dependent on the binding strength. Using these quantitative TPD measurements in comparison with DFT modeling with Hubbard U corrections will enable accurate modeling of surface reactions on strongly correlated *d* and *f* shell electron materials.

3.5 Conclusions

In summary, we have developed a comparative experiment-theory procedure to accurately identify the present material surfaces and to create the electron correlation corrected model surface

chemistry (Hubbard U values) using oxygen TPD as experimental input data. These results differ significantly from bulk material bonding characteristics. From this identification of specific surface chemical features, the material's surface and gas reaction process can be accurately modeled. This model analysis is done through the adsorption and desorption of various molecules, NO and CO. For $PrMn_2O_5$ the NO TPD peak locations are shown to correlate closely with those from the NO mechanism described by DFT, differing by no more than 0.2 eV. This agreement verifies the accuracy and reliability of the calculations based on surface Hubbard U values. The CO binding mechanisms for the perovskite oxides also showed consistent results when compared to the TPD data. Furthermore, for the first time, this work shows an accurate solution to the over-binding issues found in many covalently bonded molecules. This correction is crucial for many gas reaction catalysts including CO and NO oxidation, and CO_2 reduction to alcohols. Since the surface chemistry of materials is important to modeling and understanding the reaction mechanisms on a catalyst surface, the process of creating the correct surface morphology is crucial. Thus, this work conveys an accurate and reliable process for determining surface chemistry for reaction modeling using DFT and TPD.

References

(1) Suntivich, J.; Gasteiger, H. A.; Yabuuchi, N.; Nakanishi, H.; Goodenough, J. B.; Shao-Horn, Y. Design Principles for Oxygen-Reduction Activity on Perovskite Oxide Catalysts for Fuel Cells and Metal–Air Batteries. *Nature Chemistry* **2011**, *3* (7), 546–550.

(2) Rasul, S.; Anjum, D. H.; Jedidi, A.; Minenkov, Y.; Cavallo, L.; Takanabe, K. A Highly Selective Copper–Indium Bimetallic Electrocatalyst for the Electrochemical Reduction of Aqueous CO_2 to CO. *Angewandte Chemie* **2014**, *127* (7), 2174–2178.

(3) Korotcenkov, G.; Cho, B. Instability of Metal Oxide-Based Conductometric Gas Sensors and Approaches to Stability Improvement (short survey). *Sensors and Actuators B: Chemical* **2011**, *156* (2), 527–538.

(4) Thampy, S.; Ashburn, N.; Martin, T. J.; Li, C.; Zheng, Y.; Chan, J. Y.; Cho, K.; Hsu, J. W. P. Effect of R-Site Element on Crystalline Phase and Thermal Stability of Fe Substituted Mn Mullite-Type Oxides: $R_2(Mn_{1-x}Fe_x)_4O_{10-\delta}$ (R = Y, Sm or Bi; x = 0, 0.5, 1). *RSC Advances* **2018**, *8* (1), 28–37.

(5) Li, C.; Thampy, S.; Zheng, Y.; Kweun, J. M.; Ren, Y.; Chan, J. Y.; Kim, H.; Cho, M.; Kim, Y. Y.; Hsu, J. W. P. Thermal Stability of Mullite RMn_2O_5 (R = Bi, Y, Pr, Sm or Gd): Combined Density Functional Theory and Experimental Study. *Journal of Physics: Condensed Matter* **2016**, *28* (12), 125602.

(6) Wang, L.; Maxisch, T.; Ceder, G. Oxidation Energies of Transition Metal Oxides Within the GGA+U Framework. *Physical Review B* **2006**, *73* (19), 195107.

(7) Jain, A.; Hautier, G.; Ong, S. P.; Moore, C. J.; Fischer, C. C.; Persson, K. A.; Ceder, G. Formation Enthalpies by Mixing GGA and GGA + U calculations. *Physical Review B* **2011**, *84* (4), 045115.

(8) Kresse, G.; Furthmüller, J. Efficiency of Ab-Initio Total Energy Calculations for Metals and Semiconductors Using a Plane-Wave Basis Set. *Computational Materials Science* **1996**, *6* (1), 15–50.

(9) Langreth, D. C.; Mehl, M. J. Beyond the Local-Density Approximation in Calculations of Ground-State Electronic Properties. *Physical Review B* **1984**, *29* (4), 2310–2310.

(10) Vydrov, O. A.; Scuseria, G. E. Assessment of a Long-Range Corrected Hybrid Functional. *The Journal of Chemical Physics* **2006**, *125* (23), 234109.

(11) Redhead, P. A. Thermal Desorption of Gases. Vacuum 1962, 12 (5), 274.

(12) Wang, L.; Maxisch, T.; Ceder, G. A First-Principles Approach to Studying the Thermal Stability of Oxide Cathode Materials. *Chemistry of Materials* **2007**, *19* (3), 543–552.

(13) Lany, S. Semiconductor Thermochemistry in Density Functional Calculations. *Physical Review B* **2008**, *78* (24), 245207.

(14) Sun, L.; Li, G.; Chen, W.; Luo, F.; Hu, J.; Qin, H. Adsorption of CO on the $LaCoO_3$ (001) Surface by Density Functional Theory Calculation. *Applied Surface Science* **2014**, *309*, 128–132.

(15) Yang, J.; Zhang, J.; Liu, X.; Duan, X.; Wen, Y.; Chen, R.; Shan, B. Origin of the Superior Activity of Surface Doped $SmMn_2O_5$ Mullites for NO Oxidation: A first-principles Based Microkinetic Study. *Journal of Catalysis* **2018**, *359*, 122–129.

(16) Kumar, S.; Teraoka, Y.; Joshi, A. G.; Rayalu, S.; Labhsetwar, N. Ag Promoted $La_{0.8}Ba_{0.2}MnO_3$ Type Perovskite Catalyst for N_2O Decomposition in the Presence of O_2, NO and H_2O. *Journal of Molecular Catalysis A: Chemical* **2011**, *348* (1-2), 42–54.

(17) Laachir, A.; Perrichon, V.; Badri, A.; Lamotte, J.; Catherine, E.; Lavalley, J. C.; Fallah, J. E.; Hilaire, L.; Normand, F. L.; Quéméré, E.; Sauvion, G. N.; Touret, O. Reduction of CeO, by Hydrogen Magnetic Susceptibility and Fourier-transform Infrared, Ultraviolet and X-Ray Photoelectron Spectroscopy Measurements. *J. Chem. Soc., Faraday Trans.* **1991**, *87* (10), 1601–1609.

(18) Fronzi, M.; Soon, A.; Delley, B.; Traversa, E.; Stampfl, C. Stability and Morphology of Cerium Oxide Surfaces in an Oxidizing Environment: A first-principles investigation. *The Journal of Chemical Physics* **2009**, 131 (10), 104701.

(19) Thampy, S.; Ashburn, N.; Dillon, S.; Liu, C.; Xiong, K.; Mattson, E. C.; Zheng, Y.; Chabal, Y. J.; Cho, K.; Hsu, J. W. P. Critical Role of Mullite-Type Oxides' Surface Chemistry on Catalytic NO Oxidation Performance. The Journal of Physical Chemistry C **2019**, 123(9), 5385-5393.

(20) Aykol, M.; Wolverton, C. Publishers Note: Local Environment Dependent GGA+U Method for Accurate Thermochemistry of Transition Metal Compounds [Phys. Rev. B90, 115105 (2014)]. Physical Review B **2014**, 90 (11), 119904.

(21) Jain, A.; Ong, S. P.; Hautier, G.; Chen, W.; Richards, W. D.; Dacek, S.; Cholia, S.; Gunter, D.; Skinner, D.; Ceder, G.; Persson, K. A. Commentary: The Materials Project: A Materials Genome Approach to Accelerating Materials Innovation. *APL Materials* **2013**, *1* (1), 011002.

(22) Graciani Jesús; Márquez Antonio M.; Plata José J.; Ortega, Y.; Hernández Norge C.; Meyer, A.; Zicovich-Wilson, C. M.; Sanz, J. F. Comparative Study on the Performance of Hybrid DFT Functionals in Highly Correlated Oxides: The Case of CeO_2 and Ce_2O_3. *Journal of Chemical Theory and Computation* **2011**, *7* (1), 56–65.

(23) Corberan, V. C.; Tejuca, L. G.; Bell, A. T. Surface Reactivity of Reduced $LaFeO_3$ as Studied by TPD and IR Spectroscopies of CO, CO_2 and H_2. *Journal of Materials Science* **1989**, *24* (12), 4437–4442.

(24) Tejuca, L. G.; Bell, A. T.; Fierro, J. L. G.; Tascón, J. M. D. Temperature-Programmed Desorption Study of the Interactions of H_2, CO and CO_2 with $LaMnO_3$. *Journal of the Chemical Society, Faraday Transactions 1: Physical Chemistry in Condensed Phases* **1987**, *83* (10), 3149.

(25) Zhan, H.; Li, F.; Gao, P.; Zhao, N.; Xiao, F.; Wei, W.; Sun, Y. Influence of Element Doping on La–Mn–Cu–O Based Perovskite Precursors for Methanol Synthesis from CO_2/H_2. *RSC Adv.* **2014**, *4* (90), 48888–48896.

(26) Arakawa, T.; Takada, K.-I.; Tsunemine, Y.; Shiokawa, J. Temperature Programmed Desorption of CO from Reduced Perovskite Oxides $LnCoO_{3-x}$ (Ln=La, Sm). *Materials Research Bulletin* **1989**, *24*(4), 395–402.

(27) Wang, W.; Mccool, G.; Kapur, N.; Yuan, G.; Shan, B.; Nguyen, M.; Graham, U. M.; Davis, B. H.; Jacobs, G.; Cho, K.; Hao, X. Mixed-Phase Oxide Catalyst Based on Mn-Mullite (Sm, Gd)Mn_2O_5 for NO Oxidation in Diesel Exhaust. *Science* **2012**, *337* (6096), 832–835.

(28) Yang, J.; Zhang, J.; Liu, X.; Duan, X.; Wen, Y.; Chen, R.; Shan, B. Origin of the Superior Activity of Surface Doped $SmMn_2O_5$ Mullites for NO oxidation: A First-Principles Based Microkinetic Study. *Journal of Catalysis* **2018**, *359*, 122–129.

CHAPTER 4

AREA SELECTIVE DEPOSITION OF CO FILMS FOR CU REPLACEMENT IN BACK END OF LINE APPLICATIONS

4.1 Introduction

This chapter is written and based on work to be submitted for publication in a peer reviewed journal. The author wrote the text and performed the DFT calculations with help and input from Sumeet Pandey, Steven Wolf, Steve Kramer, John Smythe, Gurtej Sandhu, Charles Winter, Andrew Kummel, and Kyeongjae Cho. Nickolas Ashburn wrote this section as well as performed all the DFT calculations at UTD under Dr. Kyeongjae Cho and Micron Technology under Sumeet Pandey. Steven Wolf, a member of Andrew Kummel's group at UCSD, took the XPS data. Charles Winter and group contributed experimental knowledge to aid in the model development.

4.1.1 Background

The area selective atomic layer deposition and chemical vapor deposition, AS-ALD and CVD, of many 3d transition metals and other materials is becoming increasingly more important as devices scale down in size.[1] ALD has grown in popularity for its capabilities in depositing films with atomic level control, high conformality on three dimensional surfaces, and selectivity towards the chemical environments of certain surfaces.[2] In addition to the favorable growth properties, AS-ALD aids in overcoming multiple issues stemming from the use of etchants, lift-off chemicals, and resist films found in conventional lithographic patterning processes. Furthermore, to achieve the high selectivity required for patterning films using AS-ALD, the ALD precursors and reactants must exhibit characteristics including high inherent selectivity towards the target substrate (against surrounding substrates) and a higher thermal stability than the ALD deposition temperature.

Additionally, the use of a thermally driven ALD process is important as plasma enhanced ALD can damage the surface of the substrate and result in the poor coverage uniformity of high aspect ratio features.[3]

The use of ALD for Co based films has grown in popularity because of the high substrate selectivity for certain precursors as well as high conformality and thermal stability. Additionally, the Co deposition is important in many applications in microelectronics including vias, interconnects, contact materials, liners, caps, and magnetic materials.[4-8] Co has extensively been considered as a replacement for copper interconnects, an aid in the nucleation and growth of Cu on SiO_2 substrates, and a barrier for interconnect lines.[1,9,10] These metal films have typically been grown by physical and chemical deposition methods.[11-13] Recently, 1,4-di-tertbutyl-1,3-diazadiene, $Co(^{tbu2}DAD)_2$ or $(N_2C_{10}H_{20})_2Co$, has been used as an ALD precursor for the low temperature thermal AS-ALD deposition of Co to assist in Cu nucleation.[14-17] Although many Co precursors have been studied for the ALD growth of Co films, $Co(^{tbu2}DAD)_2$ has been shown to grow highly conformal, selective, and self-limiting films below 250 °C; with the precursor-reactant combination of $Co(^{tbu2}DAD)_2$ + HCOOH or TBA (tert-butyl amine), an ALD growth occurs readily on metals surface, but is inhibited on insulators such as SiO_2. While many experimental studies have been done showing the selectivity and growth characteristics of Co films on various substrates, there has been little work describing the fundamental driving forces that promote and inhibit the reaction process at ALD growth temperature on these substrate surfaces. This work investigates the underlying mechanisms of surface selective growth and describes the fundamental thermodynamic and electronic properties which affect this surface selectivity.

During the AS-ALD growth of Co(^{tbu2}DAD)$_2$ a reactant is used to facilitate the reaction kinetics of Co(^{tbu2}DAD)$_2$ to Co metal without having to exceed the molecule's decomposition temperature. It has been shown that reducers play an important role in assisting in the growth of Co films.[14-17] This work therefore studied the growth of Co films on α-quartz SiO_2 (001) and the close packed planes of metals Cu, Pt, and Co as well as the role of a reactant, NH_3, and its effect on the reaction mechanism between Co(^{tbu2}DAD)$_2$ and the substrate surface. The inherent selectivity of the precursor and reactant are examined along with the electronic properties of the precursor and its interaction with the surface during deposition. These reaction limiting characteristics are shown to dictate the growth of Co on various substrates.

4.2 Theoretical Methodology

Computational studies were performed through density functional theory using the Hubbard-U-corrected spin-polarized generalized gradient approximation (GGA) for exchange-correlation interactions in the Vienna *ab-initio* Simulation Package (VASP) with plane-wave basis with an energy cutoff of 500 eV and projector augmented-wave pseudopotentials.[18-20] The pseudopotential valence-electron configurations are $3d^74s^2$ for Co, $3d^94s^2$ for Cu, $5d^86s^2$ for Pt, $2s^22p^3$ for N, $2p^22s^2$, and $1s^1$ for H. Accurate energy calculations for elements with strongly correlated orbitals were achieved through the application of the GGA+U method.[18,19] Each supercell calculation was relaxed to a force convergence of 0.001 $eV \cdot nm^{-1}$. The k-space sampling of the Brillouin zone was done using a Monkhorst-Pack grid with a mesh density of 0.003 nm^{-1}. Each calculation was done on a supercell with surface dimensions ranging from 8x8 to 16x16 Å depending on the reaction process. Additionally, the top and bottom surfaces in each periodic supercell were spaced to a 15 Å distance in vacuum to prevent any periodic image interaction. To achieve more accurate total energies, the magnetic state of

each material was considered and relaxed in its most preferable configuration. The energies calculated were at 0 K thus bringing the zero-point energies (ZPE) into consideration. For large supercells and their formation energies, these ZPE values have been proven to be negligible.[21,22]

The formation energy of each reaction step was calculated by subtracting the substrate and gas phase reactants from the reacted supercell. Note that the formation energy is negative when the reaction is favorable. This definition can best be described by Eq. (1), where ΔE^f is the formation energy of a reaction step which is equal to the total energy of the reacted supercell, E^r, minus the substrate total energy, E^s, and the sum of the individual reactant energies, E_i, for each species *i*.

$$\Delta E^f = E^r - E^s - \sum_i E_i \quad (1)$$

4.3 Results and Discussions

The Co(^{tbu2}DAD)$_2$ molecule's charge state was first analyzed to identify the molecular characteristics as well as provide insight to possible decomposition mechanisms. It is shown in Table 4.1 that the Co atom donates one electron to each ligand, and this finding agrees well with experimental data.[1] The magnetic moment of the Co atom along with Bader charge analysis was used to identify these charge states. The magnetic moment for Co^{2+} is caused by the loss of the s orbital electrons thus leaving three unpaired d electrons in the higher energy d_{xy}, d_{xz}, and d_{yz} orbitals. Thus, the lower energy e_g states are fully occupied with four electrons. Co^{1+} shows a lower spin state due to the transfer and pairing of an s orbital electron to the d orbital after the donation of a single s electron to the remaining ^{tbu2}DAD ligand. Lastly, neutral Co should have a magnetic moment of approximately three which is verified by this data.

Table 4.1. Charge state analysis for the Co atom in the Co(^{tbu2}DAD)$_x$ complex.

Molecule	**Magnetic Moment**	**Bader Charge Density**	**Charge State**
Co(^{tbu2}DAD)$_2$	2.6	7.85	2+

Co(^{tbu2}DAD)	2.0	8.40	1+
Co	2.5	9.00	Neutral

The decomposition of Co(^{tbu2}DAD)$_2$ was further studied and the decomposition in gas phase is shown in Figure 1. Nudged elastic band (NEB) was performed to estimate the barriers during decomposition. Since the ^{tbu2}DAD ligands are thermodynamically stable even when not part of the metal complex, it was found that the removal of these ligands is the lowest energy decomposition pathway.[1,11] The thermodynamic energy for ^{tbu2}DAD removal from the Co(^{tbu2}DAD)$_2$ complex is listed in Figure 1. Here it is shown that a 2.489 eV barrier must be overcome to initiate the thermal decomposition of Co(^{tbu2}DAD)$_2$ in atmosphere while the total formation enthalpy of Co(^{tbu2}DAD)$_2$ when referenced to ^{tbu2}DAD and single atom Co is 3.539 eV. Therefore, ignoring any ligand-surface interactions which are mentioned later in the text, the Co atom binding energy to a substrate should be larger than 3.539 eV to make the Co(^{tbu2}DAD)$_2$ decomposition, and Co adsorption to the substrate with DAD ligand desorption.

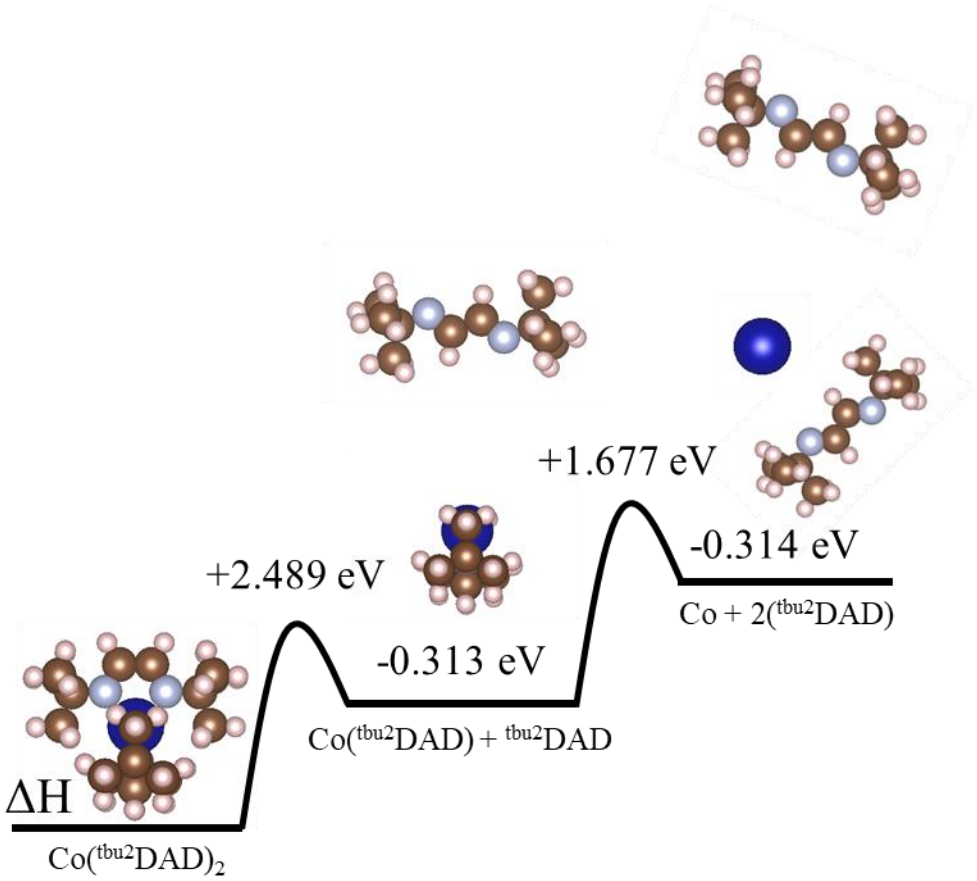

Figure 4.1. Decomposition energy and pathway for $Co(^{tbu2}DAD)_2$ in gas phase. Note there is a s-cis to s-trans change in the DAD configuration as a process during the decomposition. The change in energy dissociating the $Co(^{tbu2}DAD)_2$ molecule is linear showing a constant increase in enthalpy as the DAD and Co bonds break. However, once the DAD molecule is removed its geometry may change from s-cis to s-trans resulting in a decrease in the formation enthalpy close to -0.3 eV.

Furthermore, the formation energy of Co atom deposition on various substrates is listed in Figure 4.2. Up to seven Co atoms were used to plot the atom number dependence versus formation energy as seven atoms is required to maximize the number of nearest neighbors of initial Co clusters as illustrated in Figure 4.3 for Cu surface. For the metal substrates there is a gradual increase in formation energy with the subsequent adsorption of atoms on the surface. The small difference in the formation the energy of Co on the Pt, Cu, and Co substrates is due to the different physical dimensions of the materials. Since Pt has the largest radius, followed by Cu, the Co-Co

bonds on the surface become stretched, slightly reducing the formation energy of each Co atom. The surface chemical reactivity also follows the same trend of Co > Cu > Pt, agreeing with increasing Co binding energies on more reactive metal surfaces.

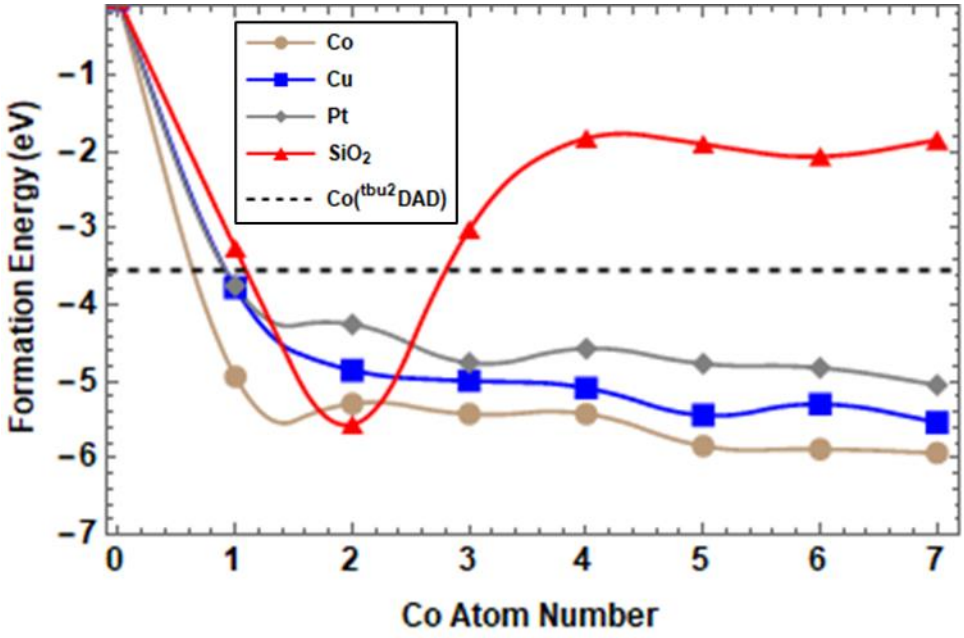

Figure 4.2. The formation enthalpy of single Co atom adsorption on Co, Cu, Pt, and SiO_2 substrates are listed for the first 7 Co atoms. Formation energies greater than the decomposition energy of $Co(^{tbu2}DAD)_2$ (3.541 eV as indicated by the horizontal dashed line) will yield Co metal growth on the substrate surface.

The Co deposition locations on the Cu metal substrate are shown in Figure 4.3 This arrangement and order of adsorption sites proved to be the most favorable on all three metal substrates. Thus, the Pt and Co substrates showed the same arrangement of Co atoms on the surface at each step, 1-7, with the exception of the Co-Co distance being smaller for the Co substrate and larger for the Pt substrate.

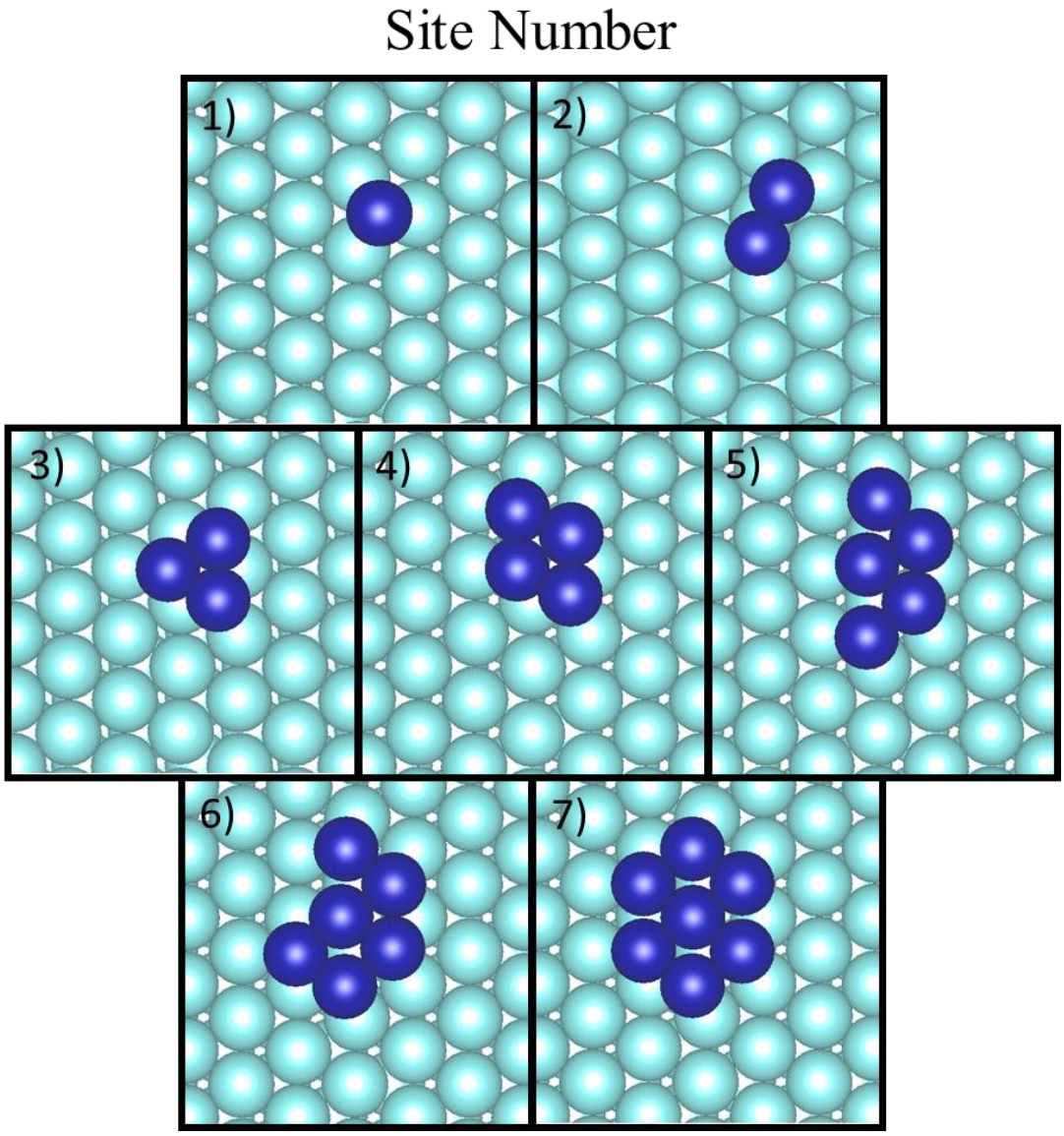

Figure 4.3. Atom by atom Co growth on the Cu surface in the most thermodynamically favorable location for each step.

Co adsorption on the SiO_2 surface is described by its own unique characteristics where continuous Co atom adsorption does not result in a steady increase in formation energy. The increase in formation energy at the beginning results from the formation of CoO_x on the surface through the consumption of weaker bound surface lattice oxygen and hydroxyl groups on defect sites. The interaction with surface hydroxyl groups can result in the formation of water as a

byproduct as H atoms migrate from one lattice oxygen to another allowing the formation of Co-O bonds and H_2O. In addition, certain sites may lack a -OH termination leading to a more reactive surface site. Therefore, as Co deposits and interacts with the surface, the binding energy decreases as the shared surface oxygen and removal of subsequent hydroxyl groups decrease the oxidation state of the surface. This results in the eventual decrease in formation energy of Co on the surface of SiO_2 as seen in the Figure 4.2. These later Co atoms no longer chemically bond to the surface oxygen, as these sites are all consumed, but rather form a layer of Co that interacts weakly with the surface while chemically bonding only to its Co neighbors. It is important to note that this mechanism occurs given the limited oxygen supply, and if O_2 gas was present in the system, this drop in formation enthalpy would not be present. For comparison, Co deposited on the SiO_2 surface with and without CoO_x formation is shown in Figure 4.4. It is shown that without allowing for CoO_x formation on the surface, Co deposition is thermodynamically unfavorable when compared to the formation enthalpy of the $Co(^{tbu2}DAD)_2$ alone. Note that this does not include the interaction between the surface and the ligands, later shown to be energetically favorable even on SiO_2.

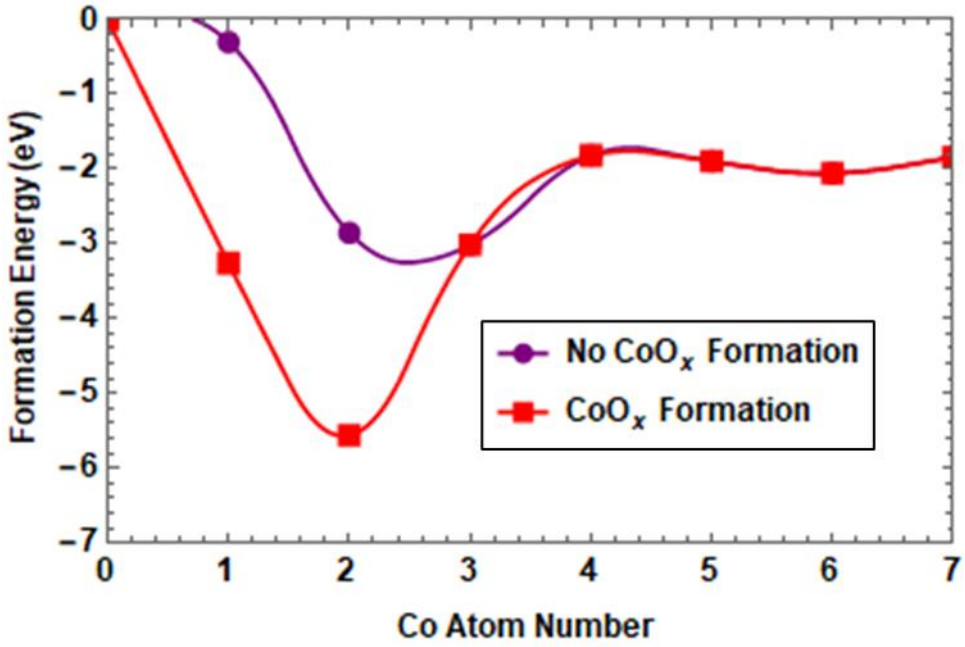

Figure 4.4. The formation energy of Co atoms deposited one by one on the SiO_2 substrate are plotted comparing the energy of Co deposition with and without CoO_x formation. Atoms 3 through 7 are shown to be the same energy because all reactive surface oxygen are already consumed where available in this particular model.

The electronic density of states (DOS) for the first two Co atoms deposited on Pt, Cu, and SiO_2 are shown in Figure 4.5. The DOS for the Co atoms deposited on Pt and Cu substrates shows a small magnetic moment for Co and lack of any energy gap, both expected characteristics for Co metal. However, Co deposited on SiO_2 shows a DOS with discrete states and the formation of energy gaps. This is indicative of two characteristics for Co adsorption on SiO_2 which vary from the Co deposition on the metal substrates. First, the energy gap is caused by the formation of the insulating CoO_x phase through the consumption of oxygen and surface hydroxyl groups which are comparatively weakly bound to the surface. This reaction yields CoO_x and some H_2O as byproducts. Second, the discrete nature of the band structure results from the poor hybridization of the Co orbitals and thus the formation of molecular-like complexes on the surface and not an

extended solid. This lack of cohesive bonding characteristics best explains the poor affinity of Co for the SiO_2 surface.

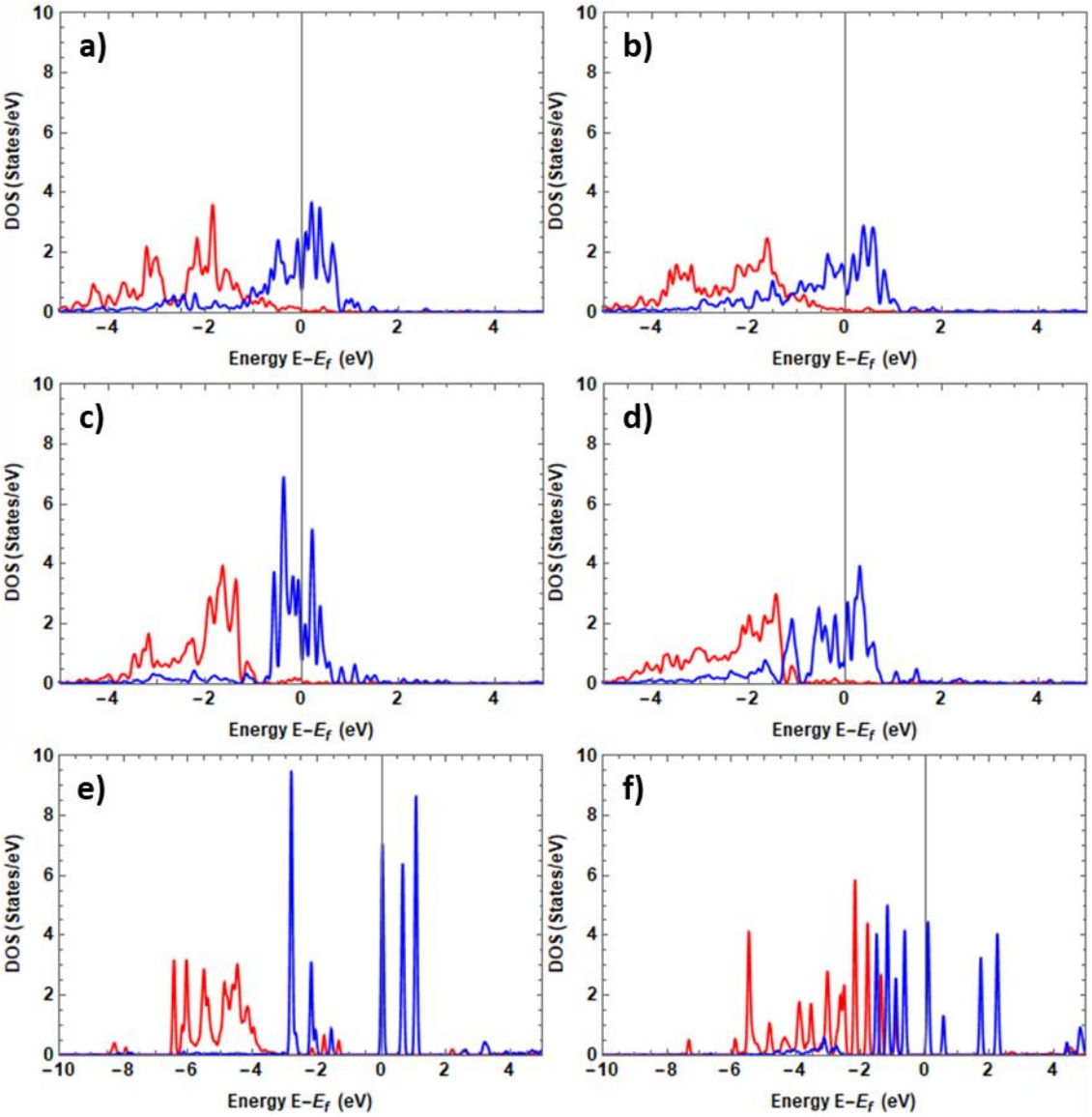

Figure 4.5. DOS for the first 2 Co atoms deposited on Pt, Cu, and SiO_2. These plots are all normalized to 1 Co atom so that the electronic structure is directly comparable. Red and blue represent spin up and down respectively. The first 2 Co atoms on Pt are shown in a) and b) respectively while the first 2 atoms on Cu are shown in c) and d), and the first 2 atoms on SiO_2 are shown in e) and f).

To study the experimental growth of Co on SiO_2 and metal substrates, and verify the predictions drawn from the theoretical work, X-ray photoelectron spectroscopy (XPS) data was

taken for the SiO_2 and Pt substrates before and after $Co(^{tbu2}DAD)_2$ exposure in ALD cycles. The XPS data are shown in Figure 4.6. Scans were taken at 0, 50, 100, and 150 cycles of the Co precursor. It is shown by the data that while Co grows well on Pt (Figure 4.6C), it only deposits small concentrations on the SiO_2 surface. Additionally, all this deposition is done within the first 50 ALD cycles, and additional ALD cycles do not change the Co concentration (Figure 4.6A). XPS further highlights the chemical species of Co on each surface. While there is a clean Co metal peak on Pt substrates (778 eV in Figure 4.6D), the SiO_2 surface yields the growth of a CoO_x film with the corresponding Co cation peak (782 eV in Figure 4.6B). This finding strongly correlates with the role lattice oxygen plays in the Co nucleation on the CoO_x surface proposed by the theoretical findings previously mentioned. Since only CoO_x is formed on SiO_2, and no subsequent growth of Co is observed, the consumption of surface lattice oxygen explains the lack of Co metal films. Once all the weakly bound hydroxyl groups react with the Co precursor during the initial ALD cycles, there no longer exists a catalyst for $Co(^{tbu2}DAD)_2$ decomposition. This depletion of labile surface oxygen terminates the nucleation of further Co sites and prevents any expansion of the already deposited CoO_x seeds. For the Pt substrate, the metal surface acts as a significantly better catalysts, which provides stable and favorable deposition energetics for Co metal growth which are not dependent on the consumption of surface oxygen species.

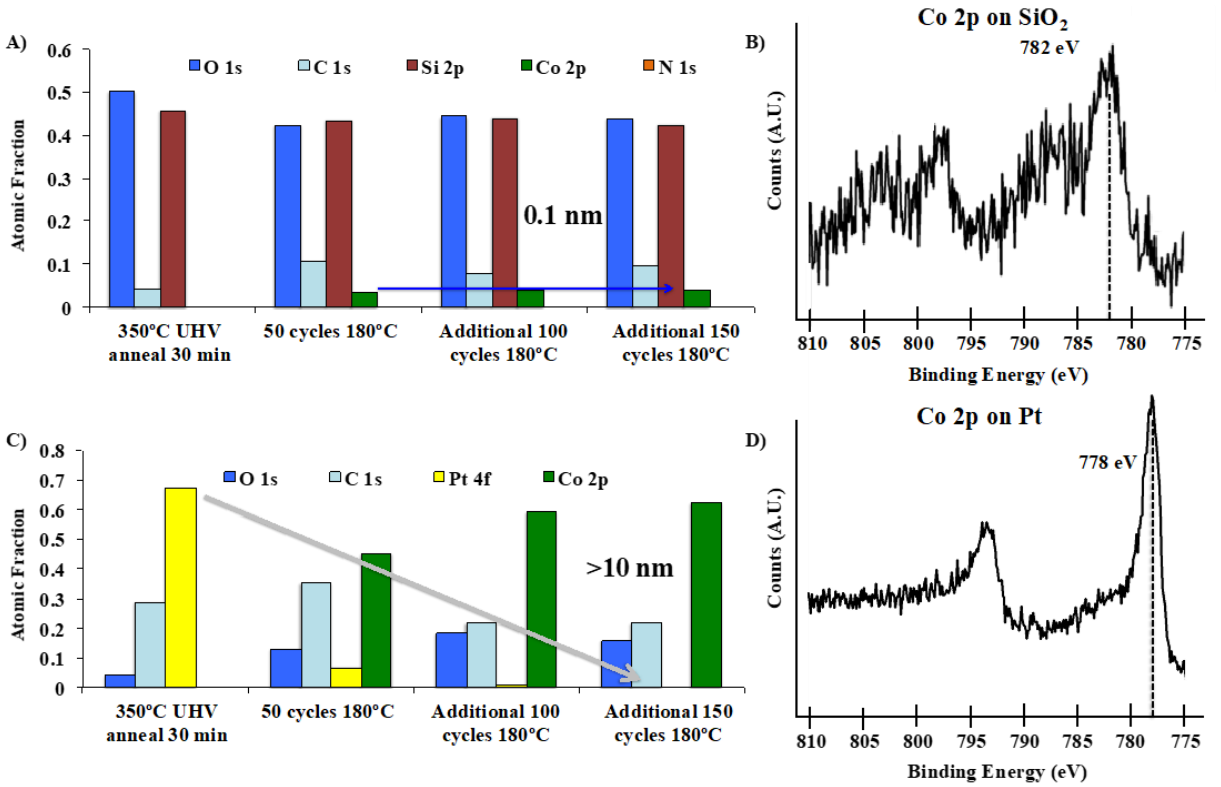

Figure 4.6. The concentration of O, C, Si, Co, and N are shown in A) for the SiO_2 surface. The XPS spectrum for the SiO_2 surface with Co deposition is shown B) followed by the elemental concentration of species on the Pt surface C) and corresponding XPS spectrum D).

It is also important to note the concentrations of the ligand elemental species in the Co films. C, N, and H are all prevalent in the precursor ligands. It is shown that little N exists in the films on both substrates. For SiO_2 this may be attributed to the limited growth. However, on the Pt substrate this trend may be best described by the desorption of N_2 gas from the film surface. The carbon is shown to exist in the films via the XPS data from Figure 4.6. Unlike N, C desorption is not as simplistic. C must interact with other species, usually O to be desorbed from a surface. The production of hydrocarbons is also possible, however, unlikely due to a low formation energy. This may explain the higher C concentrations than N in the films.

Even though the Co atomic cluster formation energies on metal and SiO_2 surfaces (Figure 4.2) are consistent with the experiment data in Figure 4.6, which shows the Co growth on Cu surface, but no Co growth on SiO_2 surface after initial CoO_x formation, there is a required activation step in the ALD experiment. Without such an activation step, Co film growth does not happen even on metal surfaces, and the role of the activation step is yet to be explained. The activating agent (or reductant) is typically a molecule with $-NH_2$ group (e.g., $(CH_3)_3CNH_2$, NH_3), and this functional group is known to play the critical activation of Co ALD reactions on metal surfaces. Since the same activating agent does not enable the Co ALD growth on SiO_2 surface which is not thermodynamically favorable, one can speculate that the role of $-NH_2$ group may provide kinetic pathways for Co precursor reactions on metal surfaces. To examine the role of such reductant, we have investigated the effects of NH_3 interaction with the metal surface during the Co ALD growth as we discuss now. We first examine the initial precursor and an intermediate reaction product as well as reactant's interaction with metal and SiO_2 surface. The formation enthalpies of $Co(^{tbu2}DAD)_2$, $Co(^{tbu2}DAD)$, and NH_3 (ammonia) are listed in Table 4.2 on the same surfaces as the single atom Co (the final ALD reaction product) formation energies. It is shown that for all the Co complex molecules as well as Co metal atom (in Figure 4.2), the surface interaction is very strong on metal substrates. Furthermore, the exothermic decomposition of NH_3 on the metal substrates induces a spontaneous reaction between ammonia and the substrate surface providing atomic hydrogens on the metal surfaces. However, on SiO_2 surface, the decomposition of $Co(^{tbu2}DAD)_2$ to molecular (^{tbu2}DAD) and surface adsorbed $Co(^{tbu2}DAD)$ is thermodynamically unfavorable. It is expected that the OH groups on the SiO_2 surface may react with the precursor to help facilitated the reaction mechanism. However, in considering the OH interaction with the

precursor, a 1.942 eV barrier was observed to reduce the ^{tbu2}DAD ligands and remove them from the Co complex. The primary reason for this large thermodynamic barrier is the relatively weak reduction of the Co(^{tbu2}DAD)$_2$ precursor in comparison to that of OH. This is one reason for the suppression of ALD reaction and the selectivity of Co(^{tbu2}DAD)$_2$ growth on metal substrates. Additionally, the decomposition of the reductant, NH_3, on the surface of SiO_2 is highly endothermic indicating that the reductant does not dissociate on the surface. The reductant is found to play an important role in the growth of Co using Co(^{tbu2}DAD)$_2$ as we discuss now. Due to this catalyzing role of the reductant, the lack of reactant affinity to the surface is another limiting step by itself in the ALD growth of Co on SiO_2.

Table 4.2. The adsorption energies of the precursor Co(DAD)$_2$ and the reactant NH_3 are listed for Pt, Cu, SiO_2, and Co.

	Co(^{tbu2}DAD)$_2$	**Co(^{tbu2}DAD)**	**NH_3**
Pt	-7.01 eV	-4.69 eV	-1.27 eV
Cu	-4.58 eV	-1.84 eV	-0.59 eV
SiO_2	-3.07 eV	+0.36 eV	+3.68 eV
Co	-4.85 eV	-2.48 eV	-1.11 eV

In addition to the reactant's, NH_3, endothermic dissociation on the SiO_2 surface, it may also play a role in passivating the SiO_2 and correspondingly weaken the precursor-surface interaction.[24] NH_3 was observed to interact with the surface hydroxyl groups in the form of hydrogen bonding resulting in a surface binding energy of -1.335 eV. This relatively strong hydrogen bonding may be responsible for blocking certain reaction sites passivating the surface and limiting the Co(^{tbu2}DAD)$_2$ interaction. This mechanism would also result in the limited nucleation observed in Figure 4.6.

The reaction enthalpies for Co(^{tbu2}DAD)$_2$ growth steps on a Cu substrate (both with and without a reductant, NH_3) are shown in Figure 4.7. The thermodynamic analysis in Figure 4.2 showed the initial and final energies of Co(^{tbu2}DAD)$_2$ decomposition to Co + 2(^{tbu2}DAD) and Co adsorption to Cu surface with overall binding energy of -0.2 eV. The red energy bar in step 10 in Figure 4.7 corresponds to this final state of the ALD reaction for a Co(^{tbu2}DAD)$_2$ molecule on Cu surface. These reaction pathways show the important role of the reductant in Co metal deposition using Co(^{tbu2}DAD)$_2$. For the Cu substrate with NH_3 used as a reactant, NH_3 has reacted with the surface prior to the adsorption of Co(^{tbu2}DAD)$_2$ such that the surface was terminated with H and NH_x species. Although most experimental processes expose the surface to Co(^{tbu2}DAD)$_2$ first, this would have no effect on the model, since the Co(^{tbu2}DAD)$_2$-bare surface interaction was also modeled and it was found to have only a physical interaction without a thermodynamically stable decomposition pathway. After 1 ALD cycle, the substrate would be exposed to reducing molecules, and subsequent cycles happen on the reductant-modified surfaces.

Figure 4.7 shows the reaction steps in three separate sections, 1) the long range molecular-surface interaction, 2) the molecular chemical reaction and dissociation on the surface, and 3) the desorption of physically bonded ^{tbu}DAD ligands on the surface. The first section, the molecule-surface interaction, shows the energies for the reference, step 1, which is the molecule and surface infinitely far away, or no interaction, followed by a molecule-surface spacing of 3-0 Å, steps 2-5, in one Å increments. Long range interactions were considered in these calculations, and it can be seen that significant attraction between the surface and molecule exist at distance without direct atomic interactions. It is also important to note that the use of a reductant, once dissociated on the substrate surface, reduces the surface-molecule interaction compared to the clean surface.

Following step 5, the molecule dissociates on the metal surface, steps 6 – 9. The step 7 marks the first ligand loss of the precursor on the surface and the divergence of the two pathways. For the clean surface, the formation enthalpy increases for every subsequent step ($5 \rightarrow 7 \rightarrow 9$). This can be described best by the bonding energy loss between the ligands and Co. While the Co atom bonds strongly to the Cu surface (~3.7 eV), the ligands have a weaker physical interaction (~1.2 eV per ligand) with the substrate surface. This physical interaction is responsible for the energy jump in the desorption step 9-10 for both surfaces. However, for the NH_3 reacted surface, there is a significant change in enthalpies during the chemical reaction steps. Step 6 is the first step in the reduction of ^{tbu2}DAD through the donation of H from the Cu surface. This step has a small increase in formation enthalpy, 0.8 eV, as the molecule transitions from the Co bonds to the two H bonds, one to each N. Step 7 is the first ligand desorption. There is an observed drop in energy here as the Co bonds to the surface and available NO_x groups that exist on the substrate. Furthermore, there is a relatively strong physical attraction between the dissociated ligand and the Cu surface, around 1.4 eV. This results in a significant drop in formation enthalpy for step 7. Step 8 and 9 are the dissociations of the last Co ligand in the same fashion. However, this time the ligand removal has no barriers to overcome as the surface-Co interaction weakens the Co-^{tbu2}DAD bonds. Finally, step 10 is simply the desorption of the ligands into atmosphere. It is important to note that the formation enthalpy plotted here is not activation energy. For the plot of activation energies at each step using the Gibbs Free Energy at 180 °C, please see Figure 4.8.

It is also important to note the role of a reductant acting on the metal surface. First, the reduction of the ^{tbu2}DAD ligands stabilizes the ^{tbu2}DAD molecule in atmosphere. This stability comes from the N-H bonds that form as surface H migrate to the Co(^{tbu2}DAD)$_2$ molecule. This

bond formation facilitates the breaking of the Co-N bonds in the molecule. There is also significant stabilization that stems from the Co atom and its interaction with NH_x groups on the surface. These NH_x groups satisfy the broken bonds created during the ligand desorption process. In combination, both these processes create an environment which reduces the activation energy steps for Co deposition on the metal surface leading to Co adatom deposition from the $Co(^{tbu2}DAD)_2$ molecule with a minor activation energy step of 0.8 eV (step 6). However, without the reductant reaction on the Cu surface, the Co adatom deposition from the $Co(^{tbu2}DAD)_2$ molecule requires ~2.2 eV (steps 5 – 7 – 9), and the ALD reaction will stop at step 5 with physically adsorbed $Co(^{tbu2}DAD)_2$ molecules on Cu surface. Without the reductant cycle, the initial ALD precursor cycles will fully cover the metal surface with the physically adsorbed $Co(^{tbu2}DAD)_2$ molecules and block the subsequent ALD cycles. At the final step 10, the Co adatom on the Cu surface is more stable on reductant-modified surface by ~4 eV due to the adatom Co-H interactions. As the ALD cycles repeats and more Co adatoms are added on Cu surface, Co clusters will form as shown in Figures. 4.2 and 4.3 and the H atoms will bond to the surface of the Co clusters playing the role of a reductant in the Co film deposition and growth.

While the ligand-surface interaction was studied, dissociation on the surface was not considered in depth. Ligand dissociation is often energetically favorable on a substrate surface acting as a catalysis for precursor decomposition. Additionally, it is shown that the metal substrates can dissociate NH_3. Consequently, the dissociation of the precursor on the metal substrates may be more favorable than reflected in this work. The desorption of the surface species may also vary and entail many different chemical specie reactions. This makes this interaction complex for large molecules like $Co(^{tbu2}DAD)_2$. However, this reaction would only serve to better facilitate Co

growth and Co(^{tbu2}DAD)$_2$ decomposition on the Pt surfaces. As for SiO_2 it is shown that the interaction is weak, and even simple decomposition steps encompass large barriers to overcome.

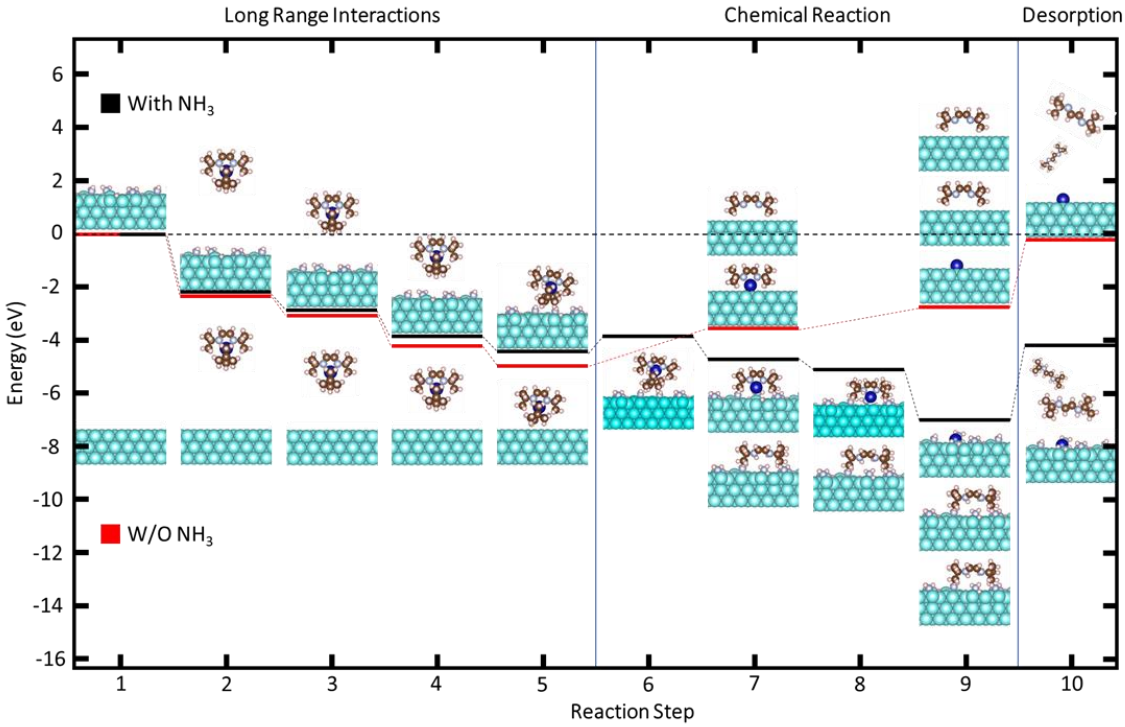

Figure 4.7. Step by step reaction energetics for Co(^{tbu2}DAD)$_2$ with the Cu surface both with and without a reducing reactant, NH_3. The red dashes represent the energy states for the Co reaction with the surface without NH_3 while the black dashes represent it with NH_3.

Figure 4.8 is the plot of activation energies for each step which includes the entropy contributions from temperature and pressure at 180 °C in addition to the enthalpies shown in Figure 4.7. Additionally, the energy difference for transition phases, reaction steps 4-5, 6-7, and 8-9, are the kinetic barriers. The largest barrier is approximately 1.1 eV at step 5, making this the limiting step in the reaction process.

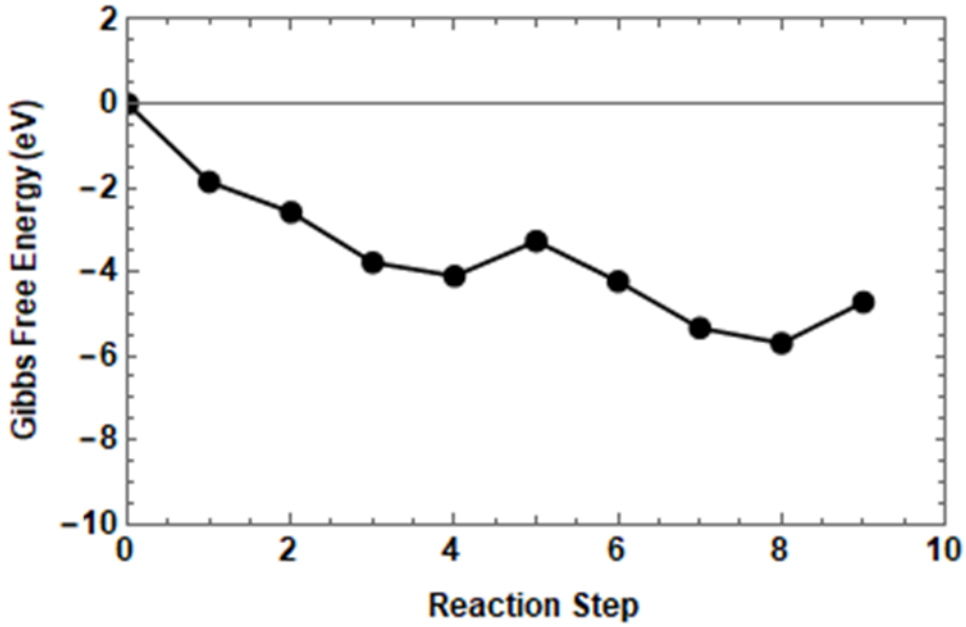

Figure 4.8. The activation energy for the NH_x passivated Cu substrate and Co(^{tbu2}DAD)$_2$ reaction is shown above for the same 10 reaction steps shown in Figure 4.7.

Furthermore, it is important to note the impact of surface migration on the ability for Co to nucleate as well as surface contaminants such as N, O, C, and H to migrate and form molecules which can potentially leave the surface. For the migration of N, O, C, and H, only the Co surface was considered as the Cu, Pt, and SiO_2 substrate surfaces are only interacted with during the first layer of growth. The migration barriers of Co on each surface were calculated using NEB to aid in understanding the limiting steps in Co nucleation. For each metal surface the migration of Co is relatively small, showing barriers below 0.6 eV, these are easily overcome at the deposition temperature. This supports the strong nucleation seen on the metal substrates during the Co deposition process. However, for the SiO_2 surface, migration can be very difficult depending on the surface local environment. For surface sites which are well passivated, each surface site is bonded to a hydroxyl group, the migration barriers are small. This is largely due to the weak interaction with Co adsorbed on the surface stemming from the lack of chemical bonding between

the surface and the Co atoms. However, provided a defect, a surface site which contains a reactive oxygen, the Co-surface interaction is comparatively strong. This 2.8 eV barrier is caused by the strong Co-O bonds which form on the surface. As significant energy is required to break these surface Co-O bonds, nucleation would occur at specific sites where reactive surface oxygen exists. As it relates to Figure 4.4, the surface selective nucleation sites correspond to the selectivity in adsorption sites. Figure 4.9 shows the migration barriers for Co on each surface broken down into five steps between identical periodic sites on the supercell. One may expect the initial and final state to be equivalent in energy in Figure 4.9 as the Co atom migrates between identical sites, this is generally true with the exception CoO_x formed on SiO_2. This drastic difference between the initial and final states comes from the surface model and how the migration barriers are calculated. However, the difference between step zero and step four does not affect the magnitude of the migration barrier as this is given by step two. This energy gap stems from the adsorption of Co to the surface. During deposition, significant surface reconstruction exists that facilitates the formation of CoO_x. This surface reconstruction is not conveyed in the migration barriers as the reaction is too complex and yielded erratic results. It should also be noted that the energy difference nears zero when examining a fully relaxed final step.

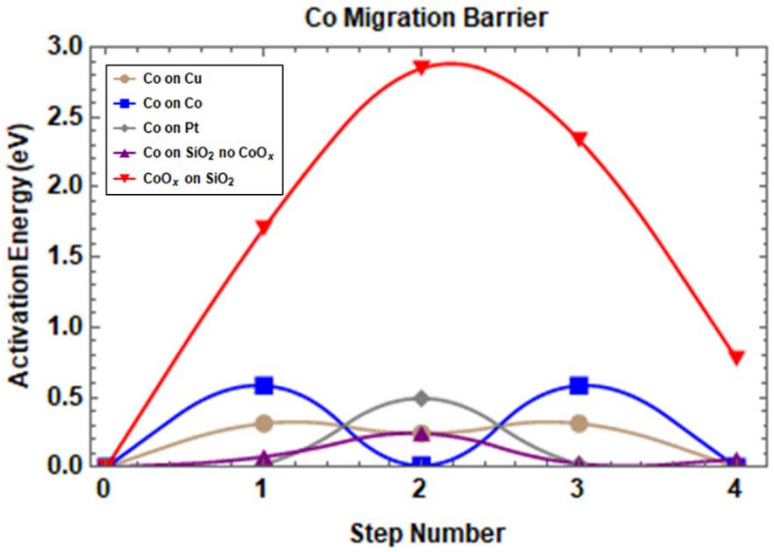

Figure 4.9. The migration barriers for Co on Cu, Co, Pt, and SiO_2 surfaces are shown over five steps. Lines are drawn to guide the eye between calculated migration images.

The migration of C and H were also calculated on the Co surface. As H plays a crucial role in the reduction and reaction processes for $Co(^{tbu2}DAD)_2$ adsorption and decomposition, it is important to consider the migration barriers. Figure 4.10 shows the migration barrier for H which is easily overcome at the reaction temperature, less than 0.2 eV, and is not a limiting reaction step. This would allow H produced from the dissociation of NH_3 to migrate easily on the surface to specific reaction sites. In addition to H, the C migration is also shown. Although, C does not play a role in the growth of Co, it is a byproduct of the ^{tbu2}DAD decomposition, which may occur on the surface. It is known that many reaction pathways exist for C that can remove them from the surface, including the formation of hydrocarbons, carbonyls, and CO_2. Since oxygen is not available in any of the reactants, the formation of carbonyls and CO_2 is limited. In addition, many reaction pathways leading to the formation of hydrocarbons exist. C can additionally be left on the surface and correspondingly in the Co film as it is deposited as shown in Figure 4.6. Due to the

numerous hydrocarbon possibilities and significant C left in the Co film, only the migration of C was calculated.

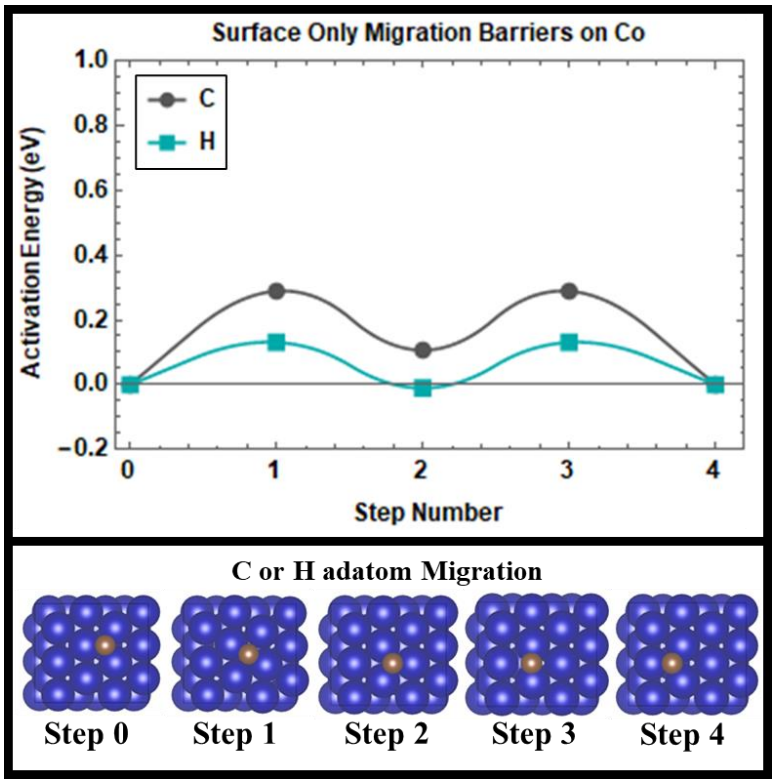

Figure 4.10. The migration barriers of adatom C and H on the surface of Co between identical sites on the supercell. The brown spheres represent C while Co is shown as dark blue. Since the migration pathway is identical for C and H on the Co surface, the images for steps 0-4 can be used to describe both C and H migration. Lines are drawn to guide the eye between calculated migration images.

Lastly, N and O migration was calculated on the Co surface. In Figure 4.11 steps 0-2 are equivalent to steps 0-4 in Figure 4.10. These five steps are shown as three do to symmetry, where only the largest reaction step is shown in the figure. In addition to adatom migration, the N-N and O-O dimer formation and desorption was also considered. O_2 gas formation was only considered to estimate the thermal energy needed to remove oxygen contaminates from the surface. The calculated O_2 migration pathway reveals the barrier to be the adsorption energy, with the removal

of oxygen from the surface being the largest energy step. The 2.6 eV barrier is substantial, making low temperature desorption slow and improbable. When relating this barrier to the methods in chapter 3, the O_2 TPD peak would exist above 900 K. The N_2 desorption kinetics where also calculated as a biproduct of NH_3 dissociation on the Co surface and subsequent reaction with $Co(^{tbu2}DAD)_2$. As H plays a large role in the reaction with ^{tbu2}DAD, N is primarily left on the surface. Figure 4.11 shows step 3 to be the desorption barrier for N_2 gas at 1.98 eV. This barrier occurs at the transition between adatom N and the formation of N-N dimers on the Co surface. Using the method from chapter 3, the temperature programmed desorption (TPD) peak can be approximated and compared to experimental data.[23] From this data, the 700 K TPD peak corresponds to a 2.09 eV barrier, which is similar to the calculated barrier of 1.98 eV. This aids in validating the accuracy of the Co-N interaction. After the N-N dimer formation, the subsequent desorption is trivial, as the remaining reaction steps have a significantly lower activation energy.

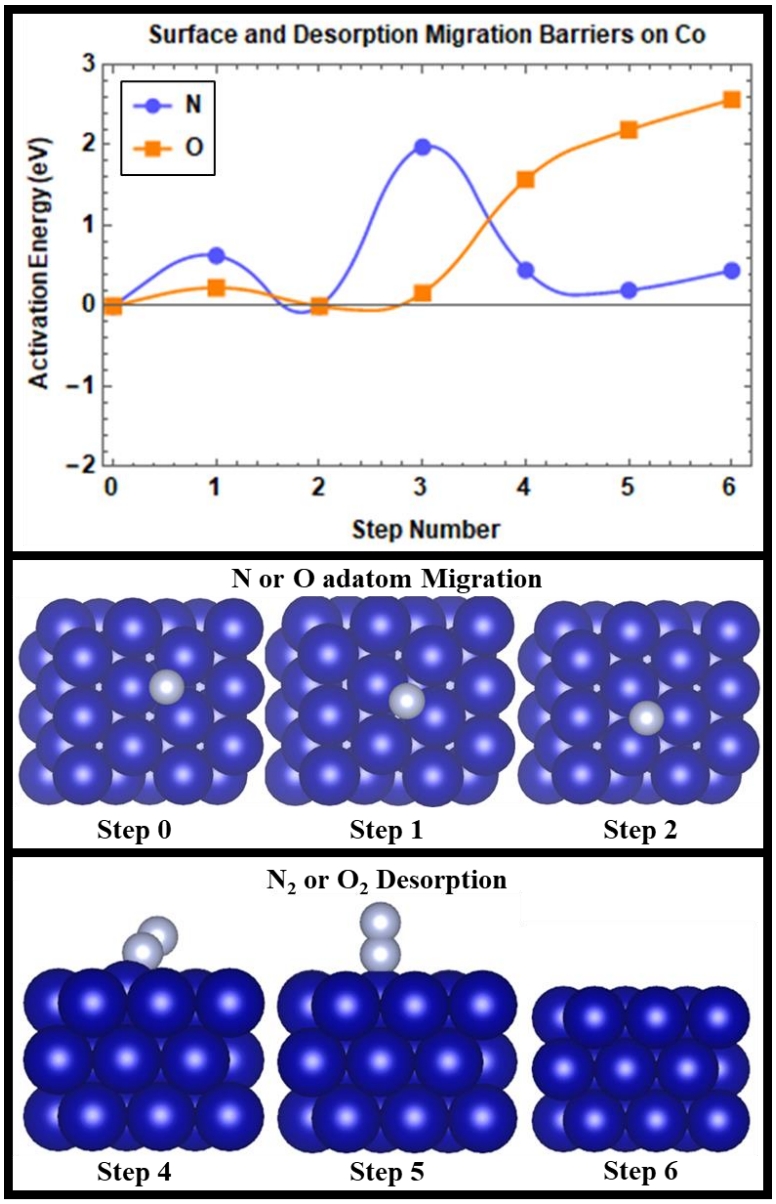

Figure 4.11. The migration barriers of N and O on Co surface are shown for adatom N and O (steps 0-2) and dimer N and O (steps 3-6). N or O is represented by the light blue spheres while Co atoms are represented in dark blue. Lines are drawn to guide the eye between calculated migration images.

4.4 Conclusions

As device features scale down in size, effective AS-ALD methods become increasingly important for nanoscale feature size control. From an application perspective, AS-ALD of Co metal serves

to address a multitude of issues in the current device fabrication process including the nucleation of Cu and the lining of Cu lines for increased electromigration resistance. Developing an effective AS-ALD process involves identifying both a precursor and a reducing reactant which react favorably with a given meal surface with high selectivity against oxide surfaces. Therefore, it is important to identify the roles of the precursor, surface, and reactant, and understand how they interact during the ALD cycles to grow highly selective and uniform films.

Using the precursor, $Co(^{tbu2}DAD)_2$, Co growth on metal substrates was well supported in experimental studies but showed poor nucleation on SiO_2. This selectivity was in part due to the role of a reductant on the metal surface when reacting with the Co precursor and ligands. Without complete thermal decomposition, the $Co(^{tbu2}DAD)_2$ molecule showed a weak dissociation energy on the SiO_2 surface. However, the removal of these ligands being catalyzed by the metal substrate, showed a much more thermodynamically favorable process. This inherent selectivity of the precursor is important to the initial deposition of precursor molecules for the subsequent reactions to form Co films. In addition to the precursor selectivity, it is also seen that NH_3 is inherently selective to the metal substrates in that it readily dissociates providing reactive atomic H on the metallic surfaces. In addition, NH_3 may serve to passivate the SiO_2 surface through strong hydrogen bonding that reduces the surface-precursor interaction. Although only one of these, the precursor or the reactant, needs to be selective to allow selective growth, the combination of inherent selectivity characteristics of both the precursor and the reactant inhibit growth on SiO_2 while facilitating the deposition on Pt, Cu, and Co.

In understanding the precursor chemistry, it is important to note the decomposition reaction pathways on the surfaces. Particularly, the precursor decomposition was catalyzed by hydrogen

bonding (provided NH_3 reductant) from the surface, as well as a strong ligand-surface interaction. Furthermore, fundamental reaction properties must be met to readily facilitate surface-selective growth. These include small enough activation barriers which can be overcome with the thermal energy at the growth temperature as well as favorable thermodynamic properties. Additionally, selective deposition without surface modification must have intrinsic selectivity that stems either from the precursor or the reactant, provided that the precursor is depended on the reactant to deposit, or both. This $Co(^{tbu2}DAD)_2/NH_3$ ALD reaction had both, with the reductant and the precursor favoring the metal substrates over the SiO_2 surface. With the addition of all these properties, area selective ALD was achieved for Co growth on metal surfaces.

In addition to the thermodynamic of adsorption, the migration kinetics of Co and various elemental species were calculated. Here Co was seen to be difficult to move on SiO_2. This in addition to the poor thermodynamics for deposition further limited the ability of $Co(^{tbu2}DAD)_2$ to deposit Co metal films on the crystalline SiO_2 surface. The migration and desorption of N adsorbed on the surface from NH_3 dissociation was also seen to have barriers which need sufficient thermal energy to overcome. However, at the 180 ˚C deposition temperature slow N_2 is feasible. The remaining H on the surface was shown to migrate easily allowing it to move quickly on the surface to interact with the Co precursor facilitating its decomposition.

While the formation enthalpy for Co metal on a conductive surface is innately favorable, there are significant activation barriers to overcome. These activation barriers stem from the removal of volatile ligands from the Co atom to the metal surface and then to atmosphere. While using a reductant, the ^{tbu2}DAD ligands can accept two H atoms from the metal surface, each bonding to one of the two N. These H atoms stabilize the ligand allowing it to be readily removed

from the Co, and the substrate surface at lower activation energies and thus lower the growth temperatures. Furthermore, the reductant has shown to increase the formation energy of Co atom deposition on the surface. The NH_x surface groups bond to the highly reactive Co atom, both stabilizing it and aiding in the reduction of the ^{tbu2}DAD ligand. The selectivity principle of precursor/reductant pairs can provide a rational understanding on diverse selective ALD growth processes on different surfaces. Such rational understanding can elucidate the underlying difficulties of some unsuccessful attempts of AS-ALD as well as providing a guiding design principle to identify promising combination of precursor/reductant/surface pair to facilitate focused experimental developments.

References

(1) Knisley, T. J., Saly, M. J., Heeg, M. J., Roberts, J. L., & Winter, C. H. (2011). Volatility and high thermal stability in mid-to late-first-row transition-metal diazadienyl complexes. Organometallics, 30(18), 5010-5017.

(2) Mackus, A. J. M., Bol, A. A., & Kessels, W. M. M. (2014). The use of atomic layer deposition in advanced nanopatterning. Nanoscale, 6(19), 10941-10960.

(3) Profijt, H. B., Potts, S. E., Van de Sanden, M. C. M., & Kessels, W. M. M. (2011). Plasma-assisted atomic layer deposition: basics, opportunities, and challenges. Journal of Vacuum Science & Technology A: Vacuum, Surfaces, and Films, 29(5), 050801.

(4) Lutsev, L. V., Stognij, A. I., & Novitskii, N. N. (2009). Giant magnetoresistance in semiconductor/granular film heterostructures with cobalt nanoparticles. Physical Review B, 80(18), 184423.

(5) Vo-Van, C., Kassir-Bodon, Z., Yang, H., Coraux, J., Vogel, J., Pizzini, S., Bayle-Guillemaud, P., Chshiev, M., Ranno, L., Guisset, V. and David, P. (2010). Ultrathin epitaxial cobalt films on graphene for spintronic investigations and applications. New Journal of Physics, 12(10), p.103040.

(6) Zhu, S., Van Meirhaeghe, R. L., Detavernier, C., Cardon, F., Ru, G. P., Qu, X. P., & Li, B. Z. (2000). Barrier height inhomogeneities of epitaxial CoSi2 Schottky contacts on n-Si (100) and (111). Solid-State Electronics, 44(4), 663-671.

(7) He, M., Zhang, X., Nogami, T., Lin, X., Kelly, J., Kim, H., ... & Zhao, L. (2013). Mechanism of Co liner as enhancement layer for Cu interconnect gap-fill. Journal of The Electrochemical Society, 160(12), D3040-D3044.

(8) Yang, C. C., Flaitz, P., Wang, P. C., Chen, F., & Edelstein, D. (2010). Characterization of selectively deposited cobalt capping layers: Selectivity and electromigration resistance. IEEE Electron Device Letters, 31(7), 728-730.

(9) Yang, C. C., Baumann, F., Wang, P. C., Lee, S. Y., Ma, P., AuBuchon, J., & Edelstein, D. (2011). Characterization of copper electromigration dependence on selective chemical vapor deposited cobalt capping layer thickness. IEEE Electron Device Letters, 32(4), 560-562.

(10) He, M., Zhang, X., Nogami, T., Lin, X., Kelly, J., Kim, H., Spooner, T., Edelstein, D. and Zhao, L. (2013). Mechanism of Co liner as enhancement layer for Cu interconnect gap-fill. *Journal of The Electrochemical Society*, *160*(12), D3040-D3044.

(11) Xu, W. Z., Xu, J. B., Lu, H. S., Wang, J. X., Hu, Z. J., & Qu, X. P. (2013). Direct copper plating on ultra-thin sputtered cobalt film in an alkaline bath. Journal of The Electrochemical Society, 160(12), D3075-D3080.

(12) Ago, H., Ito, Y., Mizuta, N., Yoshida, K., Hu, B., Orofeo, C.M., Tsuji, M., Ikeda, K.I. and Mizuno, S. (2010). Epitaxial chemical vapor deposition growth of single-layer graphene over cobalt film crystallized on sapphire. Acs Nano, 4(12), pp.7407-7414.

(13) New, R. M. H., Pease, R. F. W., & White, R. L. (1994). Submicron patterning of thin cobalt films for magnetic storage. Journal of Vacuum Science & Technology B: Microelectronics and Nanometer Structures Processing, Measurement, and Phenomena, 12(6), 3196-3201.

(14) Klesko, J. P., Kerrigan, M. M., & Winter, C. H. (2016). Low temperature thermal atomic layer deposition of cobalt metal films. Chemistry of Materials, 28(3), 700-703.

(15) Kerrigan, M. M., Klesko, J. P., Rupich, S. M., Dezelah, C. L., Kanjolia, R. K., Chabal, Y. J., & Winter, C. H. (2017). Substrate selectivity in the low temperature atomic layer deposition of cobalt metal films from bis (1, 4-di-tert-butyl-1, 3-diazadienyl) cobalt and formic acid. The Journal of chemical physics, 146(5), 052813.

(16) Kerrigan, M. M., Klesko, J. P., & Winter, C. H. (2017). Low temperature, selective atomic layer deposition of cobalt metal films using Bis (1, 4-di-tert-butyl-1, 3-diazadienyl) cobalt and alkylamine precursors. Chemistry of Materials, 29(17), 7458-7466.

(17) Kerrigan, M. M., Klesko, J. P., Blakeney, K. J., & Winter, C. H. (2018). Low Temperature, Selective Atomic Layer Deposition of Nickel Metal Thin Films. ACS applied materials & interfaces, 10(16), 14200-14208.

(18) Kresse, G.; & Furthmüller, J. (1996). Efficiency of Ab-Initio Total Energy Calculations for Metals and Semiconductors Using a Plane-Wave Basis Set. Computational Materials Science, 6 (1), 15–50.

(19) Langreth, D. C.; Mehl, M. J. (1984). Beyond the Local-Density Approximation in Calculations of Ground-State Electronic Properties. Physical Review B, 29 (4), 2310–2310.

(20) Dudarev, S. L.; Botton, G. A.; Savrasov, S. Y.; Humphreys, C. J.; & Sutton, A. P. (1998). Electron-Energy-Loss Spectra and the Structural Stability of Nickel Oxide: An LSDA+U study. Physical Review B, 57 (3), 1505–1509.

(21) Wang, L.; Maxisch, T.; & Ceder, G. (2007). A First-Principles Approach to Studying the Thermal Stability of Oxide Cathode Materials. Chemistry of Materials, 19 (3), 543–552.

(22) Lany, S. (2008). Semiconductor Thermochemistry in Density Functional Calculations. Physical Review B, 78 (24), 245207.

(23) Baiker, A., & Monti, D. (1983). Interaction of ammonia with metallic copper, nickel and cobalt catalysts studied by temperature programmed desorption. *Berichte der Bunsengesellschaft für physikalische Chemie*, *87*(7), 602-605.

(24) Mohimi, E., Zhang, Z. V., Liu, S., Mallek, J. L., Girolami, G. S., & Abelson, J. R. (2018). Area selective CVD of metallic films from molybdenum, iron, and ruthenium carbonyl precursors: Use of ammonia to inhibit nucleation on oxide surfaces. *Journal of Vacuum Science & Technology A: Vacuum, Surfaces, and Films*, *36*(4), 041507.

CHAPTER 5

RU PRECURSORS AND GROWTH CHARACTERISTICS FOR SURFACE SELECTIVE – ATOMIC LAYER DEPOSITION

5.1 Introduction

This chapter is based on a work to be submitted for publication in a peer review journal. The author wrote and performed all the calculations for the work shown below with experimental input from collaborators Andrew Kummel and group which aided in the model development and precursor selection.

5.1.1 Background

Ru metal has shown promise as a replacement for Cu lines in back end of line applications (BEOL) to reduce line resistance.[1,2] As line dimensions shrink below a 10 nm half-pitch, Ru shows performance improvements over Cu. For both dense and porous low-κ dielectrics, Ru lines shown no need for a diffusion barrier. This is in part due to Ru having significantly stronger interatomic bonding than Cu and hence weaker characteristics facilitating dielectric diffusion.[3] Correspondingly, Ru is also shown to have a higher melting point as well as higher electromigration barriers and longer lifetime.[4] Due to the stronger interatomic bonding of Ru and lack of thick barriers and liners used to prevent dielectric diffusion, the effective conductive cross-section of Ru metal lines is thus larger than that of Cu. This contributes to the improved electrical properties of Ru when compared to Cu and even Co in the sub 10 nm range. As the metals for BEOL applications have evolved, the use of atomic layer deposition (ALD) as an aid in patterning features has also grown in interest.

The ALD of metals has grown in importance to aid in the patterning of device features.[5] ALD is known for its capabilities in depositing films layer by layer with high conformality and even selectivity towards certain chemical environments.[6] Due to these favorable properties ALD can aid in device patterning by replacing some of the etching steps. As devices scale down in size and feature dimensions drop below 10 nm, alternatives to ArF immersion are needed. Extreme ultraviolet, 13.5 nm, (EUV) lithography is a promising technique to replace multiple patterning ArF at these smaller dimensions.[7] However, EUV has issues including stochastic defects, edge roughness, and low power output and thus longer exposure times.[8] ALD is thus introduced as a support for these lithography techniques in places where ALD can be deposited selectively on a specific surface making it area selective ALD (AS-ALD). ALD is unique from other chemical vapor deposition (CVD) techniques in that its layer-by-layer growth and atomic level control gives it the property of selectivity on surfaces that interact favorably with the precursor molecules. This is in part achieved by the deposition temperature, which remains below the decomposition temperature of the precursors, making the primary driving force for reaction the thermodynamic processes responsible for adsorption and decomposition of the reactants on the substrate surface. This makes the ALD process self-limiting as saturation of available surface sites is achieved.[9]

Ru ALD has been accomplished with multiple different precursors and shown successful results.[10–18] In addition to the promising resistivities and ability to deposit Ru using ALD, some precursors and methods have demonstrated substrate specific selectivity allowing them to be used in AS-ALD applications which avoid primarily oxide or treated surfaces.[12,13,17,19] This work aims to investigate and understand the underlying mechanisms and characteristics that facilitate surface selective deposition from a thermodynamic perspective. Hence, the investigation of multiple Ru

precursors are considered including bis(ethylcyclopentadienyl)ruthenium(ii) or $Ru(EtCp)_2$, RuO_4, and carish or $Ru(C_7H_{11}O_2)_2(CO)_2$. Each of these precursors have been shown to grow high quality conductive Ru films.

Each precursor was modeled on various surfaces in addition to the ligand – Ru binding energies, Ru atom migration energies, Ru atom – surface binding energies, and the C, H, O, N, and CO migration barriers. The Ru atom and surface interaction energetics were modeled both in terms of binding energy and migration kinetics on Ru, Cu, and SiO_2 surfaces to aid in understanding nucleation. For RuO_4, the precursor was examined on three surfaces including Ru, Si, and SiO_2. This was done to be consistent with literature reports of selective RuO_4 deposition on Si over SiO_2.[12] For $Ru(EtCp)_2$, the deposition process was studied on three different SiO_2 surface chemistries as well as clean Ru, and Ru with O_2 as a reactant. The Ru surfaces were examined to understand growth after the initial layer as for RuO_4. Additionally, $Ru(EtCp)_2$ was also studied on SiO_2 with labile surface O, -OH, and $-CH_3$ groups. These surfaces were studied to understand the effects surface defects can play on the growth mechanisms and the role passivation has in limiting growth. Lastly, carish was studied on Ru, with and without the reactant O_2 dissociated on the surface, and -OH terminated SiO_2.

This work aims to help elucidate a process for selecting precursor and reactant chemistries as well as surface passivation techniques to achieve selective deposition. Through the use of density functional theory (DFT) each reaction mechanism is explained. The role the reactants and precursor chemistries have on the deposition process is analyzed to better understand and predict the selectivity of ALD mechanisms. This work uses the energetics, kinetics, and local electronic

structure explain how certain precursor – reactant chemistries can be used to deposit Ru films selectively on metallic and Si surfaces.

5.2 Theoretical Methodology

Computational studies were performed with the Vienna *ab-initio* Simulation Package (VASP) using projector augmented-wave pseudopotentials. This density functional theory approach used the Hubbard-U-corrected spin-polarized generalized gradient approximation (GGA) for exchange-correlation interactions. An energy cutoff of 500 eV and projector augmented-wave pseudopotentials were utilized.[20–22] The pseudopotential valence-electron configurations are $3d^7 4s^2$ for Co, $3d^9 4s^2$ for Cu, $5d^8 6s^2$ for Pt, $2s^2 2p^3$ for N, $2p^2 2s^2$, and $1s^1$ for H. Accurate energy calculations for elements with strongly correlated orbitals were achieved through the application of the GGA+U method.[20,21] Each supercell calculation was relaxed to a force convergence of 0.001 $eV \cdot nm^{-1}$. The k-space sampling of the Brillouin zone was done using a gamma centered grid with a mesh density of 0.003 nm^{-1}. Each calculation was done on a supercell with surface dimensions ranging from 8x8 to 16x16 Å depending on the reaction process. Additionally, the top and bottom surfaces in each periodic supercell were spaced to a 25 Å distance in vacuum to prevent any periodic image interaction. The long-range interactions for each cell were calculated using dispersion corrections with the DDsC method so that the molecule-surface interaction could be best calculated. To achieve more accurate total energies, the magnetic state of each material was considered and relaxed in its most preferable configuration. The energies calculated were at 0 K thus bringing the zero-point energies (ZPE) into consideration. However, for these types of calculations the ZPE values have been proven to be negligible.[23,24] The migration barriers were

calculated using the nudged elastic band (NEB) method with the incorporation of the VTST code for the climbing image method.[25,26]

The formation energies for each reaction are calculated by Eq. (1) where ΔE^f is the formation energy of a reaction step which is equal to the total energy of the reacted supercell, E^r, minus the substrate total energy, E^s, and the sum of the individual reactant energies, E_i, for each species i.

$$\Delta E^f = E^r - E^s - \sum_i E_i \quad (1)$$

5.3 Results and Discussions

5.3.1 Ru Surface Interactions and Migration

For each of the three precursors considered, the dissociation into adatom Ru was considered. This step was done to create a reference for the thermodynamic interaction of the precursors with the different surfaces. The references for this dissociative reaction are molecular oxygen, EtCp, CO, and $C_7H_{11}O_2$. These dissociation energies are shown in Table 1. It is important to note that these are not necessarily the decomposition pathways for the molecules and only the binding energy of the individual ligands to the Ru atom is measured. These results will be used to compare to the ligand-surface interactions. Additionally, the dissociation of $Ru(EtCp)_2$ and RuO_4 can proceed in only one direction. However, for the carish precursor, the ligands are different and can be lost in various orders. Correspondingly, the lowest energy order is shown in Table 5.1 with the carbonyl loss happening first before any $C_7H_{11}O_2$ is removed from the Ru atom.

Table 5.1. The formation energy of precursor dissociation into atomic Ru and gas phase O_2, CO, $C_7H_{11}O_2$, and EtCp. The ligand lost is shown left of the dissociation energy.

	Ligand (eV)	**Ligand (eV)**	**Ligand (eV)**	**Ligand (eV)**

RuO_4	O (2.903)	O (2.644)	O (3.789)	O (1.722)
Carish	CO (0.06)	CO (2.345)	$C_7H_{11}O_2$ (4.498)	$C_7H_{11}O_2$ (3.498)
$Ru(EtCp)_2$	EtCp (4.846)	EtCp (3.919)	N/A	N/A

The binding energy of atomic Ru to various surfaces was also examined for reference with that of the precursors. The material surfaces examined were the close packed planes of Ru, Cu, Pt, H terminated Si (111), and three α-quartz (001) SiO_2 surfaces.[27] In multiple studies it has been shown that Ru growth is either inhibited or delayed on SiO_2 surfaces.[12,16,17,28] This interesting characteristic is also shown to be dependent on the surface and precursor chemistry. Thus, three SiO_2 surface chemistries are modeled along with their Ru atom interactions as Ru nucleates on the surface. These SiO_2 surfaces are as follows: SiO_2 defect is a surface with available labile oxygen, SiO_2-OH contains only -OH groups on all surface oxygen sites, and SiO_2-CH_3 is CH_3 terminated believed to result from surface treatments such as dimethylamino-trimethylsilane (DMA-TMS) to passivate SiO_2 defects and chemically reactive surfaces.[29,30]

Figure 5.1 shows the Ru-surface interaction data over a small nucleation of seven Ru atoms in a limited supercell with a surface area of roughly 80 $Å^2$. The formation enthalpy of $Ru(EtCp)_2$ is shown for reference although no ligand-surface interactions were included. It can be seen that the Ru atoms react most favorably with the metallic, Si, and un-passivated SiO_2 surfaces. The strongest interactions come from the Si and SiO_2 defect surface. For the Si surface, this is due to the Ru atoms bonding in plane with the Si (111) surface. The Si atoms exhibit a tetrahedral bonding geometry and a low atomic packing factor when compared to the metallic surfaces. This creates a porous like surface which allows the Ru atoms to embed themselves forming a layer of mixed Ru and Si. For the SiO_2 defect surface, the strong binding energy is due to the formation of RuO_x on the surface which is highly exothermic. The formation enthalpy of RuO_2 is calculated to be -3.406

eV with Ru metal and O_2 gas references which aligns closely with experimental work.[31] It should be noted that the drop in formation enthalpy of Ru on the SiO_2 surface is due to the model's limited surface oxygen supply which would not be the case in the actual environment for Ru deposition. After consuming the available labile oxygen, the subsequent Ru atoms form Ru metal on a surface that has both a different atomic arrangement and RuO_x clustering. On the metallic surfaces the formation of Ru is very closely grouped and consistently around 6 eV when referenced to atomic Ru. This clustering forms hexagonal closest packed (HCP) Ru on the surface as the metallic surfaces are atomically ordered to accommodate this grouping. This results in deposition that is more exothermic than the passivated SiO_2 surfaces. Furthermore, the surfaces of SiO_2-OH and SiO_2-CH_3 exhibit poor Ru bonding characteristics. This is expected as the interactions between Ru and crystalline SiO_2 with surface Si-OH and Si-CH_3 is weak in comparison. The model used in this figure demonstrated no chemical bonding between Ru and these passivated surfaces.

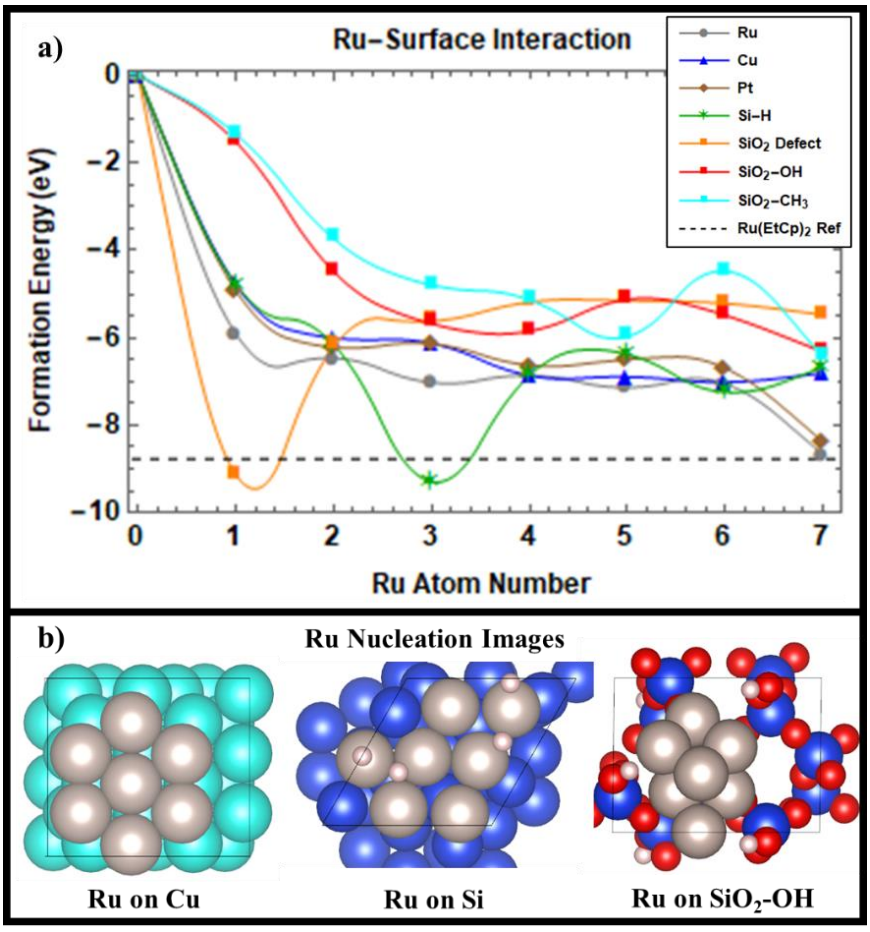

Figure 5.1. Ru adatom adsorption energies on Ru, Cu, Pt, hydrogen terminated Si, and the SiO_2 surfaces with the formation energy of $Ru(EtCp)_2$ for reference are shown in a). The SiO_2 surface is shown with three different terminations: defect (which contains reactive O), OH, and CH_3. The nucleation of Ru (silver) on Cu (teal), Si (blue), and SiO_2 (red for O) is depicted in b).

The Migration of Ru between identical sites was also calculated on Cu, Ru, and SiO_2 surfaces with and without RuO_x formation. Similar to Co, the migration of Ru when oxidized on the SiO_2 surface is comparatively large making migration difficult. The migration barrier also shows different energies between the initial and final step due to the relaxation issues in the final step as mentioned in Chapter 4. The migration barriers on SiO_2 when Ru is not oxidized are very small and mirror those of the energies found on the Cu and Ru surfaces. This result indicates quick migration on the metal substrates that allows for easy nucleation. However, the preferable binding

of Ru to oxygen on the SiO_2 surface and large migration barrier would result in clustering on the SiO_2 surfaces.

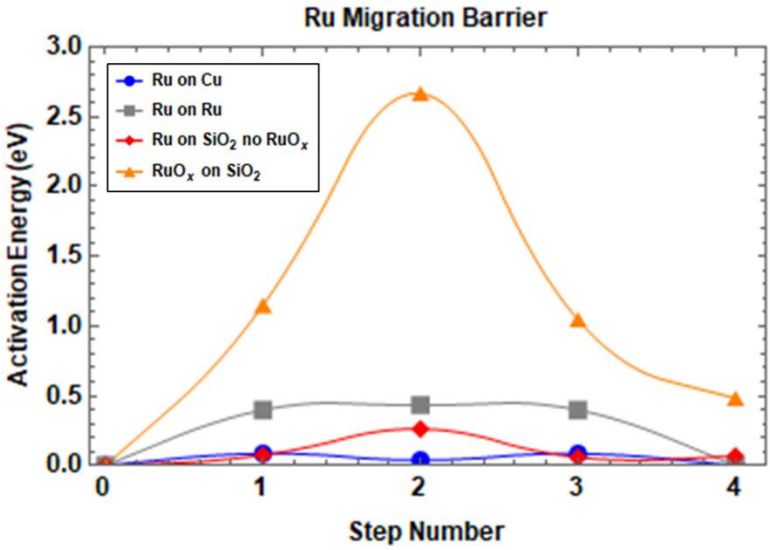

Figure 5.2. The migration of Ru is shown on Cu, Ru, and SiO_2 with and without RuO_x formation. Lines are drawn to guide the eye between calculated migration images.

In addition to the Ru migration on different surfaces, the migration of O and N on Ru is shown in Figure 5.3. The migration of N is shown to have a comparatively small kinetic barrier in the transition between atomic and molecular surface nitrogen. However, the oxygen migration is large similar to that of Co in chapter 4. The migration of O to O_2 sees its largest kinetic barrier at desorption making it the same as the overall reaction energy. This barrier is 2.56 eV which corresponds closely to experimental temperature programmed desorption (TPD) data when the molecular over-binding of O_2 is included.[32,33] This desorption barrier is particularly important to the Ru deposition processes studied in this work as many of the reaction chemistries incorporate oxygen in the precursor or as the reactant. The large desorption barrier would indicate a difficult and slow reaction process for oxygen desorption without the use of a catalyst. Oxygen in conductive films is known to lower the conductivity of the material as the formation of oxides is

generally less conductive. This is true for Ru and RuO_x. Correspondingly, this increases the importance of surface treatments and reactants that aid in Ru deposition without the incorporation of oxygen. Additionally, this large desorption barrier for O_2 makes the annealing and post treatment processes increasingly important as these steps can have large effects on the conductivity of the Ru film.[34]

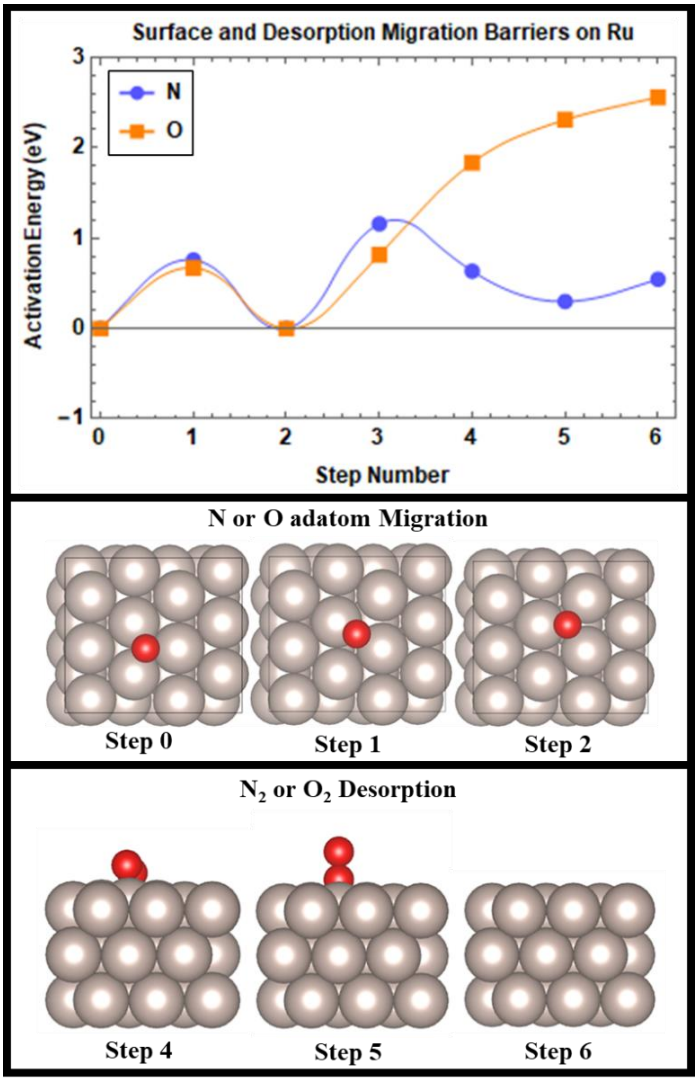

Figure 5.3. The kinetic barriers for adatom N and O surface migration (steps 0-2), N-N and O-O surface dimer formation (3), and N_2 and O_2 desorption (4-6). The silver balls are Ru atoms while the red are O atoms. The pathway for O_2 and N_2 desorption are very similar so pictorial diagram for steps 0-6 can be used as reference for both N and O migration. Lines are drawn to guide the eye between calculated migration images.

Additional migration barriers were calculated for species commonly found in the precursor chemistries considered, RuO_4, $Ru(EtCp)_2$, and carish. These are carbon, hydrogen, and carbon monoxide. The migration barriers for these species are shown in Figure 5.4. C and H are found in most of the precursor chemistries used in Ru deposition, even those not considered here. Due to this, C and H migration are crucial in understanding the growth of Ru films, impurities, and conductivity. Small migration barriers are important as it allows these atoms to migrate quickly and at low temperatures on the Ru surface. This quick movement along the surface can contribute to the efficient desorption of various species including water, carbonyls, CO_2, and hydrocarbons. Figure 5.4 shows the H atom migration to be very trivial, however, the C migration barrier is somewhat larger. This 0.66 eV barrier for C is easily overcome at deposition temperatures and even at room temperature. Additionally, carbonyl groups are found in carish as well as may other precursors for Ru deposition such as triruthenium dodecacarbonyl ($Ru_3(CO)_{12}$).[28] Therefore, the migration of CO was also considered. The migration of CO on the surface is similar to that of H and proceeds along the same path. The smaller migration of CO when compared to C can be attributed to the C-surface bonding. Since C may create four surface bonds, possibly all to different atoms, the migration along the path shown in Figure 5.4 results in the coordination of C changing from three to two and back to three (steps 0-2 and 2-4). The effect this has on the CO molecule is reduced as the bond order is also reduced due to the shared O=C double bond.

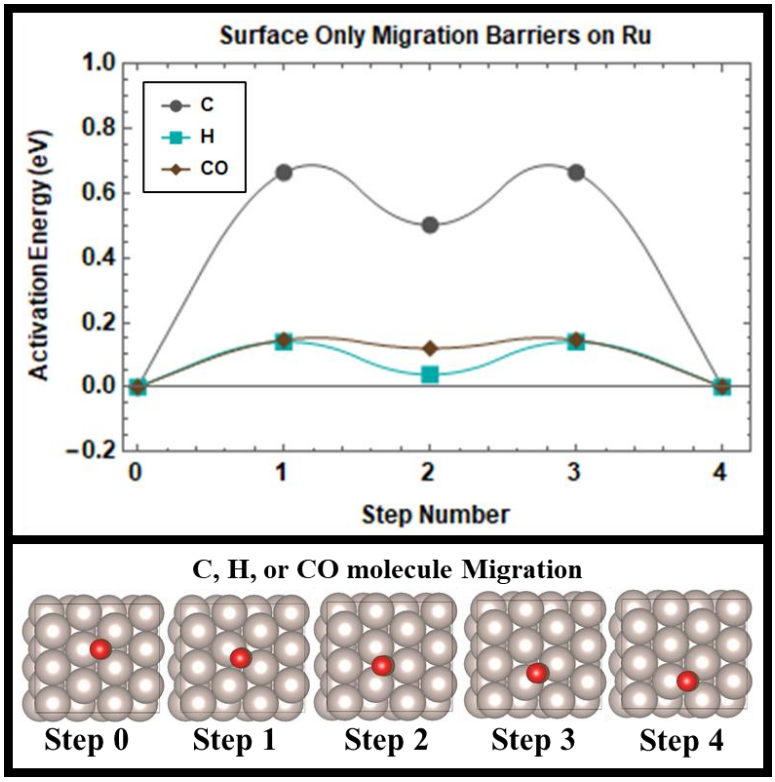

Figure 5.4. Migration of C, H, and CO along the Ru surface between symmetric sites 0 and 4. The silver spheres represent Ru while the red spheres represent O atoms. The brown balls, which can be vaguely seen underneath the red, are C atoms. Although CO is shown in steps 0-4, the migration pathway is identical for each species. Lines are drawn to guide the eye between calculated migration images.

5.3.2 RuO_4

The deposition of RuO_4 has been shown to be selectively deposited on Si while avoiding SiO_2.[12] This observed property makes it an excellent candidate for the selective deposition of Ru on metallic substrates as well. Correspondingly, RuO_4 was studied to better understand the underlying mechanisms that limit growth on the unmodified SiO_2 surface. RuO_4 is a relatively volatile precursor with a decomposition temperature of 125 ˚C.[35] This mean RuO_4 has to be deposited at lower temperatures than most precursors which can have negative effects on the electrical properties. However, despite this RuO_4 shows promise as a selective precursor as its

strong oxidative properties make it difficult to dissociate on certain oxide materials. RuO_4 is commonly deposited with H_2 gas as a reactant. Hence the impact of H_2 on the Ru and SiO_2 surfaces is examined as way of removing O in the form of H_2O. This will aid in lowing the resistivities of the deposited films as well as catalyze the precursor decomposition.

The formation enthalpy for the deposition of RuO_4 on Ru, H terminated Si, and OH terminated SiO_2 is shown in Figure 5.5. Each step corresponds to the reaction of one O with H to form H_2O from the RuO_4 precursor. For RuO_4 gas step 0 and 1 are identical in which no surface interaction is observed and no O is lost (the energetics follow Table 5.1). The formation enthalpy of Ru on Ru and Si surfaces is shown to be exothermic given H_2O as a product of H_2 gas and RuO_4. However, on the SiO_2 surface the reaction is more challenging as significant increases in energy are observed. The deposition of RuO_4 on SiO_2 was found to interact poorly with the surface. In order to facilitate the dissociation of the RuO_4 on the surface, the surface bound -OH groups would be required to react forming H_2O. This would create a vacancy on the surface, if H_2O was desorbed from the surface, or an available labile surface O, if H_2O was desorbed from RuO_4. This process is endothermic and results in an increase in the system enthalpy of 2.3 eV (steps 1-2). This would be unlikely to be overcome at the deposition temperature of 100 ˚C.

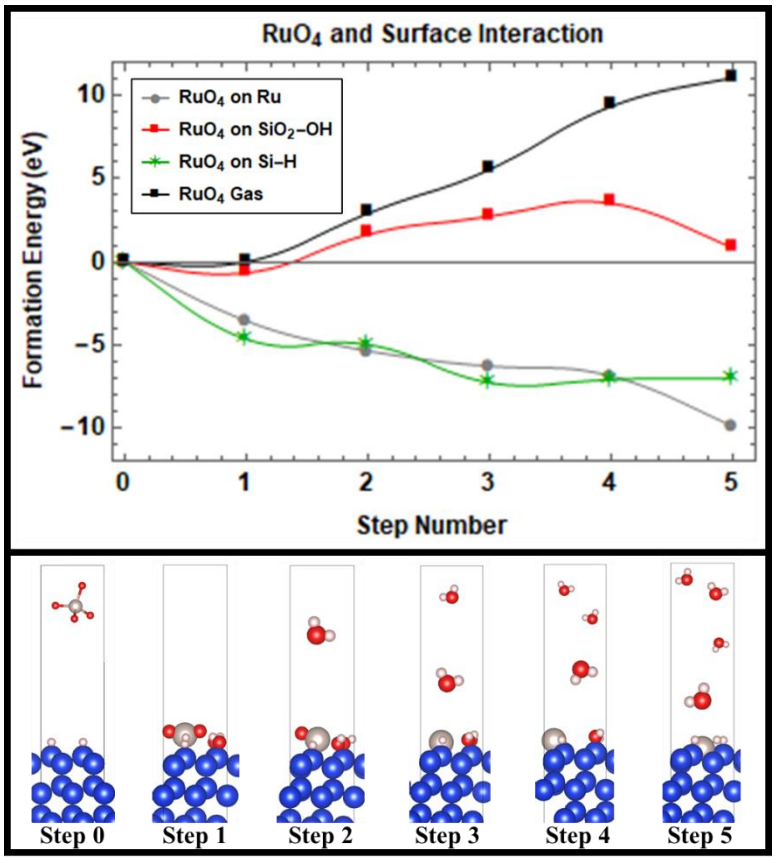

Figure 5.5. The formation enthalpy of each step for the deposition process of RuO_4 on Ru, H terminated Si (111), and SiO_2-OH is shown with the dissociation of RuO_4 in gas phase for reference. Depictions of each reaction step are shown for Ru on Si where the spheres colored silver, red, blue, and white represent Ru, O, Si, and H atoms respectively.

The dissociation of Ru on H terminated Si is shown to be highly exothermic. From initial adsorption to final dissociation, RuO_4 on Si results in an enthalpy change of -7.042 eV. Unlike SiO_2, the Si surface is readily oxidized making the adsorption and dissociation trivial on Si. However, this also creates a barrier when breaking the newly formed surface Si-O bonds. When RuO_4 is adsorbed it is energetic favorable to dissociate, forming RuO_x and surface Si-O and Si-O-H bonds. For deposition on Si, steps 2 and 3 form H_2O as a product of H_2 gas and the remaining oxygen bonded to Ru. It can be seen that these steps are exothermic. However, for steps 4 and 5, O is taken from the surface. These surface O are more difficult to remove as small increases in

enthalpy are observed. Part of this is due to the comparatively weak interaction between the Si surface and H_2O. This may result in a small fraction of oxygen being left behind in the interface between the Si substrate and the Ru film.

Furthermore, the growth of Ru on Ru is shown to be the most exothermic. For Ru, the dissociation on the surface is spontaneous, similar to Si. The RuO_4 molecule once adsorbed creates surface – O bonds as well as Ru – Ru bonds which facilitate the RuO_4 dissociation and allow O to migrate on the surface away from the RuO_4. Additionally, Ru displays a stronger H_2O interaction with the surface. This creates a larger overall change in the formation enthalpy for Ru deposition when the H_2O – surface interaction is considered. Therefore, we do not see any steps which result in an increase in enthalpy. Table 5.2 shows the reaction step energies which are plotted in Figure 5.5.

Table 5.2. The change in enthalpy from step 0 (no interaction) between RuO_4 and the substrate surface for each reaction step is shown below.

Change in Reaction Step Enthalpy ΔH (eV)			
Reaction Step	Clean Ru Surface	Si-H Surface	SiO_2-OH Surface
1	-3.553	-4.655	-0.665
2	-5.359	-4.985	+1.635
3	-6.275	-7.269	+2.733
4	-6.874	-7.091	+3.515
5	-9.892	-7.042	+0.839

The impact of the reactant H_2 on the reaction process as well as its ability to remove native oxygen from the substrate surface is important to the film's growth and electrical properties. Multiple H_2 and O interactions were thus studied on each surface including the H_2 – surface interaction, H_2O formation from surface oxide and H_2 gas, H_2 dissociation energy on the surface, O dissociation energy, and the H_2O binding energy to the surface. These values are listed in Table 5.3 where the binding energy is the molecular – surface interaction and

dissociation energy is the energy of a gas phase molecule dissociating into atomic species on the surface (e.g. O_2 gas to lattice O). As mentioned above, the interaction between H_2O and the Si surface is weak when compared to that of Ru or SiO_2. Additionally, the formation of H_2O from surface adsorbed O is more endothermic than Ru but less than that of SiO_2. This is largely due to stronger surface Si-O binding energy when compared to Ru. Table 5.3 also shows the impact of saturation on the O binding energy to the Ru surface. When Ru is close to saturation with native oxide, the binding energy of O is reduced. This is expected, and results in easier H_2O formation but a weaker H_2O interaction with the surface.

Table 5.3. The binding energy of H_2 and H_2O to each surface without dissociation (Van der Waals or long-range interaction), along with the H_2 dissociation energy and H_2 to H_2O formation energy. Each energy is referenced to the molecule total energy and surface total energy independently. For the oxidized surfaces, the O_2 dissociation energy is calculated when O vacancies exist to avoid saturation. Similarly, H_2 dissociation on Si is calculated from a H terminated Si surface with H vacancies.

	Ru Clean	Ru With Native O	Si-H	SiO_2-OH
O_2 Dissociation Energy (eV)	-6.492	-4.814	-7.034	-8.208
H_2 Binding Energy (eV)	-0.059	-0.063	-0.086	-0.412
H_2O Binding Energy (eV)	-0.617	-0.215	-0.136	-1.127
H_2 Dissociation Energy (eV)	-1.232 (Ru-H)	-0.613 (O-H)	-2.322 (Si-H)	-0.226 (H_2O)
H_2 to H_2O Formation (eV)	+0.043	-0.791	+0.314	+0.901

5.3.3 $Ru(EtCp)_2$

$Ru(EtCp)_2$ has been shown in multiple cases to exhibit selective properties to metals over oxides.[11,36] In addition, $Ru(EtCp)_2$ has been shown to achieve further selectivity from surfaces when passivated with CH_3.[13] These selective properties along with a high thermal stability above

350 ˚C and lower volatility when compared to RuO_4 make $Ru(EtCp)_2$ a promising candidate for AS-ALD.[37] Due to this, $Ru(EtCp)_2$ was modeled on five different surfaces, clean Ru, Ru with surface adsorbed oxygen, -OH passivated SiO_2, -CH_3 passivated SiO_2, and surface defect model for SiO_2 exhibiting both Si and O with dangling bonds. Figure 5.6 shows the formation energy associated with the surface interaction with $Ru(EtCp)_2$. Step 0 is the reference point where no interaction is present, followed by the adsorption of $Ru(EtCp)_2$ to the surface in step 1. Correspondingly, this means step 0 and 1 are the same for $Ru(EtCp)_2$ dissociation in gas phase as no surface interaction is present. Step 2 and 3 are the first and last ligand loss respectively, where for the RuO_x surface with combustion (solid purple line) the EtCp reacts with the surface oxygen to yield CO_2, H_2O, and a clean Ru surface. However, it should be noted that during actual growth oxygen is generally left in the Ru films in small concentrations when used as a reactant or in the precursor which differs from the model's ideal combustion. Lastly, for all reaction processes the reactant-surface interactions were also calculated and considered in each step. These interaction energies are listed in Table 5.4.

Table 5.4. The binding energies in eV for molecules considered in the reaction process and each of their relevant surfaces. The binding energies are calculated in reference to the molecule itself in gas phase and the undisturbed surface slab (e.g. Ru atom binding is equal to the energy of a Ru atom adsorbed on the clean Ru surface minus the addition of the clean Ru surface and Ru adatom energies). Note the binding energy of O_2 on RuO_x and SiO_2-OH is weaker than Table 5.3. This is due to these surfaces being completely oxidized with no vacancies before the O_2 interaction was measured.

		Surface				
		Clean Ru	Ru with Native oxygen	SiO_2-OH passivation	SiO_2 Surface Defect	SiO_2-CH_3 Passivation
Molecule	$Ru(EtCp)_2$	-3.004 (eV)	-2.252 (eV)	-1.447 (eV)	-2.412 (eV)	-1.499 (eV)
	Ru(EtCp)	-6.721 (eV)	-5.496 (eV)	-2.107 (eV)	-5.801 (eV)	-1.882 (eV)
	EtCp	-4.249 (eV)	-1.275 (eV)	-0.839 (eV)	-4.423 (eV)	-0.902 (eV)

Table 5.4, continued

Molecule	Ru Atom	-5.916 (eV)	-2.845 (eV)	-1.526 (eV)	-9.245 (eV)	-1.347 (eV)
	CO_2	-0.241 (eV)	N/A	-0.379 (eV)	N/A	N/A
	H_2O	-0.617 (eV)	N/A	-1.127 (eV)	N/A	N/A
	O_2	-6.492 (eV)	-0.099 (eV)	-0.084 (eV)	-5.758 (eV)	N/A

The Binding energies for CO_2 and H_2O are not shown on surface models for SiO_2 defect, SiO_2-CH_3 and Ru with surface oxygen. This is because the reaction on Ru with surface oxygen will ideally consume a majority of the surface oxygen leaving small quantities left in the film, therefore the interaction with the clean Ru surface was considered in the combustion process. The SiO_2-CH_3 surface did not show favorable combustion and therefore the CO_2 and H_2O energies are not considered. For the SiO_2 defect surface, similar to Ru with native oxygen, the interaction between the products and the surface was assumed to be largely happening on the dominant -OH terminated surface area while Ru would nucleate and bond to these defect sites. Additionally, the O_2 binding energy was considered on saturated surfaces for RuO_x and SiO_2 to measure the interaction between the O_2 reactant and the intrinsic surfaces. It can be seen that for the clean Ru and SiO_2 defect surfaces, O_2 binding is very strong. However, while the strong O_2 interaction is needed for O_2 adsorption and dissociation, it also has drawbacks in that the O are harder to remove. This tradeoff is common in many catalytic processes for oxygen reduction reaction.[38] Using Table 5.3, this is partially responsible for the weaker surface oxygen interaction exhibited on the SiO_2-OH surface.

Furthermore, Figure 5.6 shows that the combustion process and reduction of surface RuO_x to Ru and CO_2 and H_2O is slightly more exothermic than the clean Ru surface binding and dissociating the EtCp ligands. This is due to the combined interaction of CO_2 and H_2O with the

Ru surface as well as the formation enthalpy of CO_2 and H_2O from EtCp and surface O. For the clean Ru surface, a large formation energy of 6.12 eV is shown at the peak for Ru deposition from $Ru(EtCp)_2$. This energy largely stems from the binding of Ru and EtCp to the surface. Furthermore, the large EtCp binding energy of -4.249 eV would serve to poison the surface with dissociated hydrocarbons if no reactant was provided. This serves to emphasize the importance of O_2 gas as a reactant, as it provides a combustion pathway for the removal of the hydrocarbons left on the surface. Furthermore, the surface oxygen is shown to diminish the surface ligand interaction. It is seen that without the combustion of the EtCp ligands to CO_2 and H_2O, the reaction is endothermic. This is due to the near saturation of the oxygen p orbital on the Ru surface when only one layer of oxygen is present. This further serves to aid in the desorption of the reaction products from the $Ru(EtCp)_2$ deposition process as the EtCp ligands are less likely to stick to the surface. In addition, only the Ru surface with oxygen is capable of combusting the ligands as the clean Ru surface has no available oxygen and the SiO_2 is perfectly terminated with OH groups which proved to be endothermic in reacting with the EtCp. This is in disagreement with other experimental studies, however, the DFT calculations show that -OH removal from the crystalline SiO_2 surface exceeded 3.756 eV (using O_2 reference) which is larger than the corresponding formation enthalpy of CO_2 and H_2O from the hydrocarbon ligands.[13] However, this discrepancy may stem from the model being ideal in that all the dangling bonds on the surface are saturated and no excess -OH groups are left on the surface. Additionally, this characteristic was only true for perfectly terminated SiO_2, as it is shown later in Figure 5.7, any labile surface oxygen create a highly exothermic deposition process on the surface.

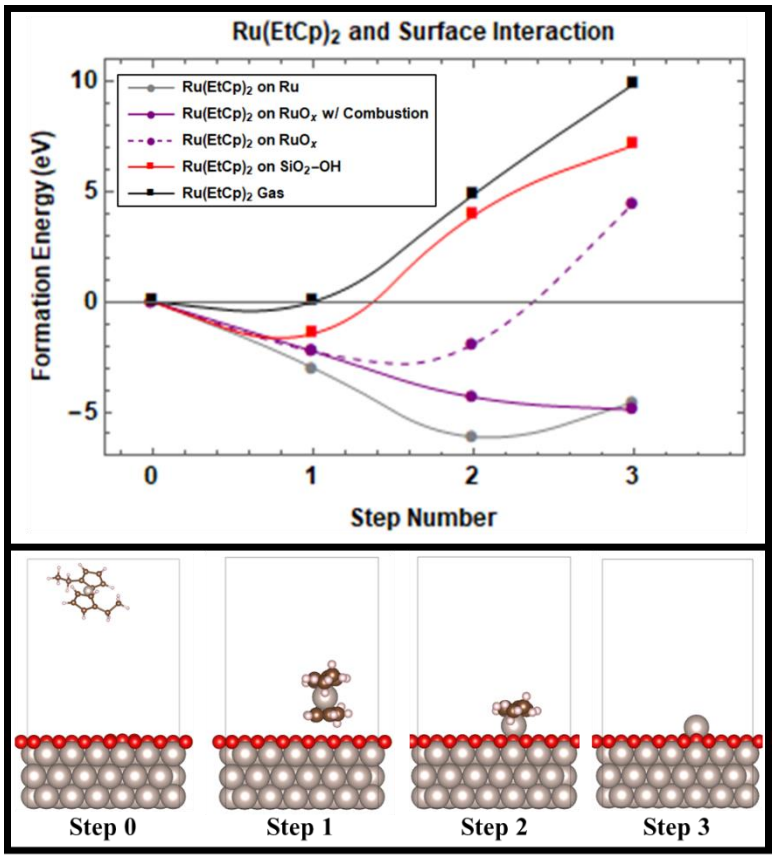

Figure 5.6. The formation enthalpy of each step for the deposition process of $Ru(EtCp)_2$ on Ru, Ru with surface O (RuO_x) , and SiO_2-OH is shown with the dissociation of $Ru(EtCp)_2$ in gas phase for reference. Depictions of each reaction step are shown for Ru on RuO_x where the spheres colored silver, red, brown, and white represent Ru, O, C, and H atoms respectively.

The comparison between the three SiO_2 surface terminations is shown in Figure 5.7. It can be seen that any labile surface O that may exist on defect sites along the surface can react with the $Ru(EtCp)_2$ precursor resulting in a highly exothermic reaction. As these types of surface sites may be scattered across the surface nucleation would be expected to be sporadic, only growing on sites which the precursor can react with. This rational may serve to explain the growth characteristics of Ru on SiO_2. Ru growth on SiO_2 is often slow to nucleate and can be seen to nucleate in large clusters scatters on the substrate surface.[16,28,36] As more defects sites are formed the nucleation of Ru on SiO_2 may accelerate and become more homogeneous. In contrast, surface exposures to

molecules such as DMA-TMS or ammonia gas may prove to passivate the surface by bonding to these reactive sites and depositing CH_3 and NH_x.[28–30] This would inhibit the interaction between Ru and the surface. Correspondingly, Figure 5.7 shows a similar result, where the passivation of the SiO_2 surface with -CH_3 leads to a reduction in the formation energy of Ru from $Ru(EtCp)_2$. Furthermore, for Figures 5.6 and 5.7, the formation energy at each step is included in Table 5.5 with reference to the initial step where no interaction is present.

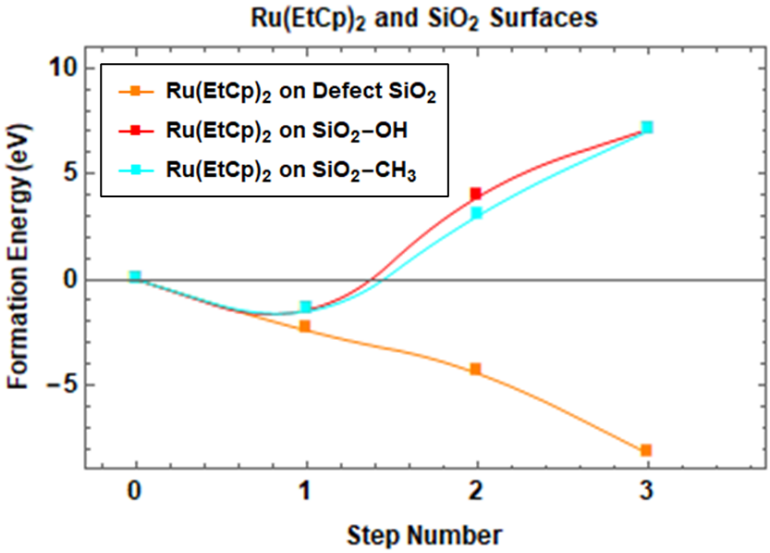

Figure 5.7. The formation enthalpy of the reaction steps shown in Figure 5.6 between $Ru(EtCp)_2$ and each SiO_2 surface, SiO_2-OH, SiO_2 defect, and SiO_2-CH_3.

Table 5.5. The formation energy of each reaction step for each surface at 0 K. Each energy is referenced to step 0 where no interaction is present. Step 1 is the adsorption of $Ru(EtCp)_2$ to the surface, followed by one ligand dissociation at step 2 and 3 respectively.

Change in Reaction Step Enthalpy ΔH (eV)					
Reaction Step	Clean Ru Surface	RuO_x Surface	SiO_2-OH Surface	SiO_2 Defect Surface	SiO_2-CH_3 Surface
Step 1	-3.004	-2.252	-1.447	-2.412	-1.499
Step 2	-6.124	-4.324	+3.891	-4.442	+2.998
Step 3	-4.554	-4.902	+7.090	-8.231	+7.023

The surface oxygen p orbital density of states (DOS) was calculated for surface oxygen on RuO_x, SiO_2-OH, and the SiO_2 defect surface. The local DOS for these oxygen is shown in Figure 5.8. Here the local DOS shows the p orbital of the surface oxygen on the SiO_2-OH surface to be completely occupied. This is responsible for the reduced reactivity of the SiO_2 surface when compared to the other surfaces in this model. However, the SiO_2 defect surface shows unoccupied nonbonding states above the fermi level. These oxygen atoms have an unsaturated p orbital which is advantageous for Ru deposition as the surface – precursor interaction is strengthen through the oxidation of Ru and the EtCp ligands. Furthermore, the RuO_x surface contains oxygen with a p orbital occupancy between the SiO_2 surfaces. As mentioned above, this near saturation reduced the surface interaction with the $Ru(EtCp)_2$ precursor when compared to the clean Ru surface.

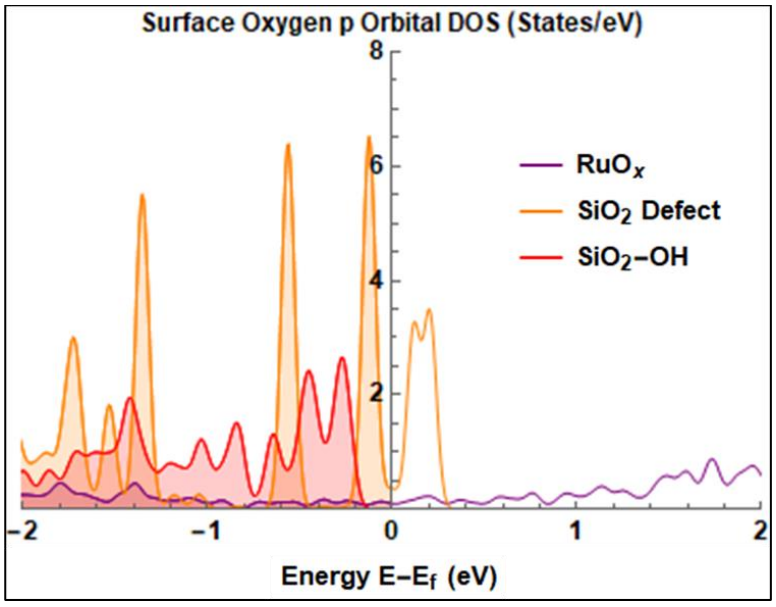

Figure 5.8. The local DOS of surface oxygen on RuO_x, SiO_2 defect, and SiO_2-OH surfaces.

5.3.4 Carish

The carish precursor is unique out of the three precursors considered here in that it has many different decomposition pathways via its two different ligands, CO and $C_7H_{11}O_2$. Carish is

not as well studied for the selective deposition of Ru as RuO_4 and $Ru(EtCp)_2$. However, other carbonyl precursors have shown to be selective in certain environments.[28] The unique chemistry of carish provide multiple decomposition pathways which may result in different energetics at different reaction steps. Thus, each pathway must be considered to account for the most thermodynamically feasible reaction mechanism. Table 5.6 shows the reaction pathways as well as the change in enthalpy for each step. Furthermore, for the Ru surface with native oxide (RuO_x), the ligands can react with the O atoms on the surface to create CO_2 and H_2O. This is shown to be favorable when compared to the reaction processes missing combustion. As for $Ru(EtCp)_2$, for each reaction step, the interaction of the products with the surfaces are included such that the dissociation of the removed ligands and long-range interaction of H_2O and CO_2 with the surfaces are accounted for.

Table 5.6. The reaction enthalpies for each step along with the reaction pathway is shown for each of the surfaces considered. The reference energy is the previous step to highlight the different decomposition orders.

	Clean Ru Surface	RuO_x Surface	SiO_2-OH Surface
Surface Adsorption	-5.360	-5.082	-1.842
1st Ligand Dissociation (eV)	-3.339 ($C_7H_{11}O_2$)	-2.150 ($C_7H_{11}O_2$)	-0.160 (CO)
2nd Ligand Dissociation (eV)	-0.052 (CO)	+0.729 (CO)	+0.777 (CO)
3rd Ligand Dissociation (eV)	+0.454 (CO)	+0.120 (CO)	-2.924 ($C_7H_{11}O_2$)
Last Ligand Dissociation (eV)	+0.292 ($C_7H_{11}O_2$)	-2.354 ($C_7H_{11}O_2$)	-2.580 ($C_7H_{11}O_2$)

The reaction energies are further plotted in Figure 5.9 with and without the combustion process for RuO_x as done for $Ru(EtCp)_2$. It can be seen that the deposition of Ru is favorable on SiO_2-OH unlike $Ru(EtCp)_2$ and RuO_4. This favorable deposition, however, only includes the

thermodynamics and the kinetic barriers for dissociation were not calculated due to the complexity and size of the molecules. This may hinder some of the explanation for growth characteristics beyond the thermodynamic understanding. However, the energetics still offer valuable insight into the deposition mechanisms indicating that the growth of Ru from carish would proceed unselectively provided the kinetic barriers were met. This indicates little to no surface affinity from the carish precursor. The exothermic deposition of carish on SiO_2 stems from two main causes. These are the ability of the $C_7H_{11}O_2$ to strip H from the surface -OH groups and the carbonyl's strong interaction with the surface O. This reaction results in a ΔH of -2.714 eV facilitating the nucleation of Ru. In addition, this is for a surface with no labile oxygen as shown for $Ru(EtCp)_2$.

Like the Ru surfaces, the SiO_2 surface is shown with and without O_2 in the environment. This is different from previous sections as O_2 is now able to react with vacancies created on the surface from the CO and $C_7H_{11}O_2$ interaction with the surface -OH groups. O_2 can dissociate on the vacancies exothermically, replacing the Si dangling bond with O which is supplied as the reactant. This leads to the formation of a SiO_2 surface which has many reactive O and few -OH groups making it highly reactive for further deposition steps, similar to that shown on the SiO_2 defect surface with $Ru(EtCp)_2$.

It is also seen that different surfaces provide different pathways for dissociation. These dissociation pathways are influenced by the ligand interactions with the surface and the Ru interaction with the surface. For the Ru surfaces, the $C_7H_{11}O_2$ ligand is the first to be removed. This allows the Ru to bond to the surface, as the strong Ru-O bonds limit the surface interaction. Once this bonding is broken, the Ru precursor can chemically, bond to the Ru surface. With the removal of CO first, the precursor – surface interaction is reduced to a long-range interaction.

However, in gas phase and on SiO_2, this CO is the first to desorb. The CO – Ru binding energy, -1.23 eV, is weaker than that of the other ligand, -3.998 eV, which makes it easier to remove. Since the gas phase consists of no surface interaction CO is the first to remove. However, for SiO_2, the CO is desorbed first due to the difficulty of removing a ($C_7H_{11}O_2$) ligand and the lack of available bonding sites. Once the CO ligands are removed, the Ru interaction with -OH groups become exothermic as the ($C_7H_{11}O_2$) can react with the -OH groups creating surface vacancies and reactive O for the CO to form CO_2 and Ru to form Ru – O bonds.

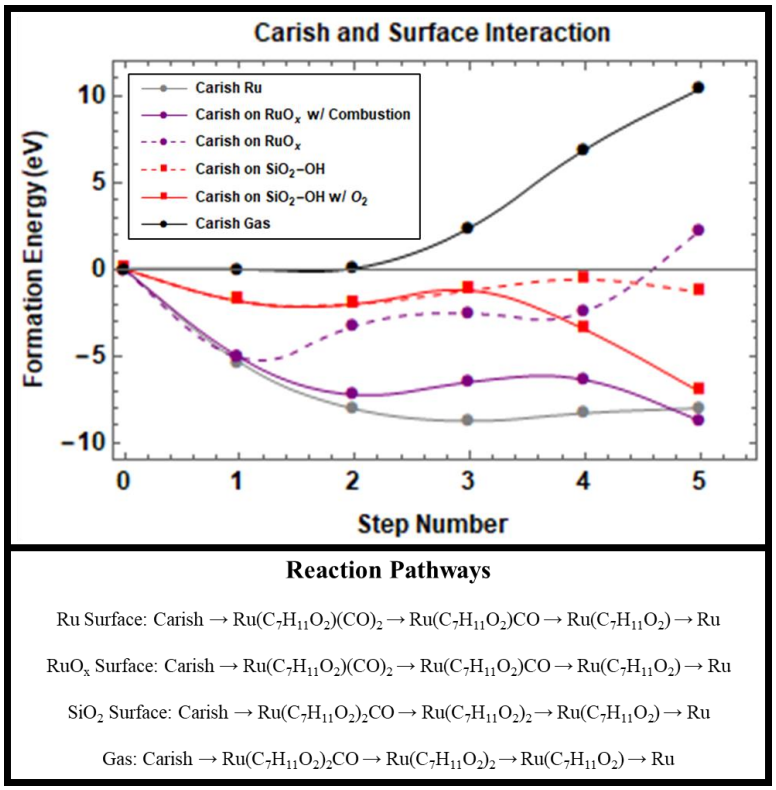

Figure 5.9. The reaction energies and pathways for carish on each surface.

5.4 Conclusions

The deposition mechanisms for AS-ALD are important to understanding and creating selective precursors and reactants. As devices continue to scale, new patterning techniques will

become increasingly important. Deposition techniques which deposit selectively on specific surfaces promise effective ways to accelerate and improve certain lithography steps. As the size of features continues to decrease and lithography processes such as EUV become increasing common, AS-ALD can be used to aid in reducing the lithography steps needed as specific features such as vias and interconnects are patterned through their deposition processes. The use of Ru in these processes compliments this type of fabrication, as better performing materials are required with the continued scaling. Ru shows promise as an improved conductor for small line cross-sections. The strong interatomic bonding of Ru gives it good thermal stability and increases its resistance to dielectric diffusion. This allows Ru to be deposited in BEOL application with little to no barrier or liner, increasing the effective conducting area.

This work showed the deposition properties of three precursors, two which are selective in deposition, avoiding SiO_2, and one which was not. The migration and nucleation characteristics of Ru and C, H, N, O, and CO were also examined. This data showed low migration barriers on clean metal surfaces while exhibiting high Ru migration for oxidized Ru on SiO_2. These barriers indicate the growth of large clusters of Ru on the surface during the nucleation process as Ru targets the thermodynamically favorable sites and is limited in its ability to migrate along the surface. The migration and desorption of O was also seen to be difficult without a catalyst or reactant such as H_2. The O binding energy was shown to be above 2.56 eV which would limit and slow the desorption as O_2 gas. With O_2 commonly used as a reactant, this emphasizes the importance of reductants and annealing steps such as H_2 treatments to reduce the RuO_x formation in deposited films and increase the film's conductivity.

The deposition of RuO_4 was shown to be selective on Si and Ru when compared to SiO_2. This stemmed from the precursor's strong oxidative properties resulting in weak chemical bonding to the SiO_2 surface. Additionally, the reactant H_2 was shown to dissociate poorly on SiO_2 further complicating the deposition process. For Si and Ru, H_2 dissociated readily as the RuO_4 binding and interaction with the surface was exothermic. In addition, H_2 gas showed to be a viable treatment for removing O from the Ru films.

The $Ru(EtCp)_2$ precursor was also examined and shown to be selective in ideal environments. Similar to RuO_4 the thermodynamics of Ru deposition on Ru were favorable while on α-quartz SiO_2 passivated with -OH or $-CH_3$, the interaction between the $Ru(EtCp)_2$ precursor and the surface was shown to be endothermic. Additionally, without surface vacancies, the O_2 interaction with SiO_2 was also shown to be weak in which dissociation was endothermic. This creates a need for O vacancies, either from the precursor – surface interaction or from thermal desorption, to facilitate a strong interaction with the reactant. However, provided labile oxygen or surface defects, the reaction became exothermic. This could explain the more radical clustering and nucleation delays on SiO_2 when compared to clean metallic surfaces. The small availability of nucleation sites limits the initial growth. Additionally, the effects of surface treatments to passivate the SiO_2 surface were examined. When $-CH_3$ groups are attached to the Si atoms on the surface, the surface – precursor interaction is weakened. The $-CH_3$ groups limited the EtCp ligand and Ru bonding to the surface facilitating selective deposition.

The non-selective precursor, carish, was shown to interact favorably with SiO_2 as the carbonyl groups and O in the precursor could react with the surface -OH groups. This resulted in an exothermic reaction on both Ru and SiO_2. Furthermore, the role of O_2 as a reactant was shown

to be crucial in removing the carbonyls and hydrocarbons on the Ru surface during the deposition process. O_2 was shown to react exothermically both in dissociation on the Ru surface and in forming CO_2 and H_2O as reaction products.

The use of passivation techniques and oxidative precursor – reactant chemistries could be adjusted to achieve selective growth using a variety of precursors and reactants. Understanding these mechanisms further allows us to tune ALD reaction for selective growth. Strong oxidative precursors or ligands that interact poorly with passivated SiO_2 can be used to achieve selective growth despite atomic Ru showing little affinity for metallic surfaces.

References

(1) Xunyuan Zhang; Huai Huang; Patlolla, R.; Wei Wang; Mont, F. W.; Juntao Li; Chao-Kun Hu; Liniger, E. G.; McLaughlin, P. S.; Labelle, C.; Ryan, E. T.; Canaperi, D.; Spooner, T.; Bonilla, G.; Edelstein, D. Ruthenium Interconnect Resistivity and Reliability at 48 Nm Pitch. In *2016 IEEE International Interconnect Technology Conference / Advanced Metallization Conference (IITC/AMC)*; IEEE, 2016; pp 31–33. https://doi.org/10.1109/IITC-AMC.2016.7507650.

(2) Liang Gong Wen; Adelmann, C.; Pedreira, O. V.; Dutta, S.; Popovici, M.; Briggs, B.; Heylen, N.; Vanstreels, K.; Wilson, C. J.; Van Elshocht, S.; Croes, K.; Bommels, J.; Tokei, Z. Ruthenium Metallization for Advanced Interconnects. In *2016 IEEE International Interconnect Technology Conference / Advanced Metallization Conference (IITC/AMC)*; IEEE, 2016; pp 34–36. https://doi.org/10.1109/IITC-AMC.2016.7507651.

(3) van der Veen, M. H.; Heyler, N.; Pedreira, O. V.; Ciofi, I.; Decoster, S.; Gonzalez, V. V.; Jourdan, N.; Struyf, H.; Croes, K.; Wilson, C. J.; Tokei, Z. Damascene Benchmark of Ru, Co and Cu in Scaled Dimensions. In *2018 IEEE International Interconnect Technology Conference (IITC)*; IEEE, 2018; pp 172–174. https://doi.org/10.1109/IITC.2018.8430407.

(4) Hu, C.-K.; Kelly, J.; Chen, J. H.-C.; Huang, H.; Ostrovski, Y.; Patlolla, R.; Peethala, B.; Adusumilli, P.; Spooner, T.; Gignac, L. M.; Bruley, J.; Breslin, C.; Cohen, S. A.; Lian, G.; Ali, M.; Long, R.; Hornicek, G.; Kane, T.; Kamineni, V.; Zhang, X.; Mont, F.; Siddiqui, S. Electromigration and Resistivity in On-Chip Cu, Co and Ru Damascene Nanowires. In *2017 IEEE International Interconnect Technology Conference (IITC)*; IEEE, 2017; pp 1–3. https://doi.org/10.1109/IITC-AMC.2017.7968977.

(5) Knisley, T. J.; Saly, M. J.; Heeg, M. J.; Roberts, J. L.; Winter, C. H. Volatility and High Thermal Stability in Mid- to Late-First-Row Transition-Metal Diazadienyl Complexes. *Organometallics* **2011**, *30* (18), 5010–5017. https://doi.org/10.1021/om200626w.

(6) Mackus, A. J. M.; Bol, A. A.; Kessels, W. M. M. The Use of Atomic Layer Deposition in Advanced Nanopatterning. *Nanoscale* **2014**, *6* (19), 10941–10960. https://doi.org/10.1039/C4NR01954G.

(7) Kim, S.-S.; Chalykh, R.; Kim, H.; Lee, S.; Park, C.; Hwang, M.; Park, J.-O.; Park, J.; Kim, H.; Jeon, J.; Kim, I.; Lee, D.; Na, J.; Kim, J.; Lee, S.; Kim, H.; Nam, S.-W. Progress in EUV Lithography toward Manufacturing; Panning, E. M., Goldberg, K. A., Eds.; 2017; p 1014306. https://doi.org/10.1117/12.2264043.

(8) Bisschop, P. De. Stochastic Effects in EUV Lithography: Random, Local CD Variability, and Printing Failures. *J. Micro/Nanolithography, MEMS, MOEMS* **2017**, *16* (04), 1. https://doi.org/10.1117/1.JMM.16.4.041013.

(9) Ritala, M.; Leskelä, M. Atomic Layer Deposition. In *Handbook of Thin Films*; Elsevier, 2002; pp 103–159. https://doi.org/10.1016/B978-012512908-4/50005-9.

(10) Leick, N.; Verkuijlen, R. O. F.; Lamagna, L.; Langereis, E.; Rushworth, S.; Roozeboom, F.; van de Sanden, M. C. M.; Kessels, W. M. M. Atomic Layer Deposition of Ru from CpRu(CO)2Et Using O2 Gas and O2 Plasma. *J. Vac. Sci. Technol. A Vacuum, Surfaces, Film.* **2011**, *29* (2), 021016. https://doi.org/10.1116/1.3554691.

(11) Lu, J.; Low, K. Bin; Lei, Y.; Libera, J. A.; Nicholls, A.; Stair, P. C.; Elam, J. W. Toward Atomically-Precise Synthesis of Supported Bimetallic Nanoparticles Using Atomic Layer Deposition. *Nat. Commun.* **2014**, *5*. https://doi.org/10.1038/ncomms4264.

(12) Minjauw, M. M.; Rijckaert, H.; Driessche, I. Van; Detavernier, C.; Dendooven, J. Nucleation Enhancement and Area-Selective Atomic Layer Deposition of Ruthenium Using RuO4 and H2 Gas. *Chem. Mater.* **2019**, *31* (5), 1491–1499. https://doi.org/10.1021/acs.chemmater.8b03852.

(13) Zyulkov, I.; Krishtab, M.; De Gendt, S.; Armini, S. Selective Ru ALD as a Catalyst for Sub-Seven-Nanometer Bottom-Up Metal Interconnects. *ACS Appl. Mater. Interfaces* **2017**, *9* (36), 31031–31041. https://doi.org/10.1021/acsami.7b07811.

(14) Wen, L. G.; Roussel, P.; Pedreira, O. V.; Briggs, B.; Groven, B.; Dutta, S.; Popovici, M. I.; Heylen, N.; Ciofi, I.; Vanstreels, K.; Østerberg, F. W.; Hansen, O.; Petersen, D. H.; Opsomer, K.; Detavernie, C.; Wilson, C. J.; Elshocht, S. Van; Croes, K.; Bömmels, J.; Tőkei, Z.; Adelmann, C. Atomic Layer Deposition of Ruthenium with TiN Interface for Sub-10 Nm Advanced Interconnects beyond Copper. *ACS Appl. Mater. Interfaces* **2016**, *8* (39), 26119–26125. https://doi.org/10.1021/acsami.6b07181.

(15) Eom, T. K.; Sari, W.; Choi, K. J.; Shin, W. C.; Kim, J. H.; Lee, D. J.; Kim, K. B.; Sohn, H.; Kim, S. H. Low Temperature Atomic Layer Deposition of Ruthenium Thin Films Using Isopropylmethylbenzene-Cyclohexadiene-Ruthenium and O2. *Electrochem. Solid-State Lett.* **2009**, *12* (11), 85–88. https://doi.org/10.1149/1.3207867.

(16) Vos, M. F. J.; Chopra, S. N.; Verheijen, M. A.; Ekerdt, J. G.; Agarwal, S.; Kessels, W. M. M.; Mackus, A. J. M. Area-Selective Deposition of Ruthenium by Combining Atomic Layer Deposition and Selective Etching. *Chem. Mater.* **2019**, *31* (11), 3878–3882. https://doi.org/10.1021/acs.chemmater.9b00193.

(17) Maniwa, A.; Chiba, H.; Kawano, K.; Koiso, N.; Oike, H.; Furukawa, T.; Tada, K. Characterization of Ru Thin Films from a Novel CVD/Atomic Layer Deposition Precursor "Rudense" for Capping Layer of Cu Interconnects. *J. Vac. Sci. Technol. A Vacuum, Surfaces, Film.* **2015**, *33* (1), 01A133. https://doi.org/10.1116/1.4902560.

(18) Winter, C. H.; Upadhyay, A.; Overbeek, M.; Hollin, J.; Cwik, S. Group 7 and 8 Compounds for Chemical Vapor Deposition. *Ref. Modul. Chem. Mol. Sci. Chem. Eng.* **2020**, 1–19. https://doi.org/10.1016/b978-0-12-409547-2.14951-0.

(19) Park, K. J.; Doub, J. M.; Gougousi, T.; Parsons, G. N. Microcontact Patterning of Ruthenium Gate Electrodes by Selective Area Atomic Layer Deposition. *Appl. Phys. Lett.* **2005**, *86* (5), 1–3. https://doi.org/10.1063/1.1852079.

(20) Kresse, G.; Furthmüller, J. Efficiency of Ab-Initio Total Energy Calculations for Metals and Semiconductors Using a Plane-Wave Basis Set. *Comput. Mater. Sci.* **1996**, *6* (1), 15–50. https://doi.org/10.1016/0927-0256(96)00008-0.

(21) Langreth, D. C.; Mehl, M. J. Beyond the Local-Density Approximation in Calculations of Ground-State Electronic Properties. *Phys. Rev. B* **1983**, *28* (4), 1809–1834. https://doi.org/10.1103/PhysRevB.28.1809.

(22) Dudarev, S. L.; Botton, G. A.; Savrasov, S. Y.; Humphreys, C. J.; Sutton, A. P. Electron-Energy-Loss Spectra and the Structural Stability of Nickel Oxide: An LSDA+U Study. *Phys. Rev. B* **1998**, *57* (3), 1505–1509. https://doi.org/10.1103/PhysRevB.57.1505.

(23) Wang, L.; Maxisch, T.; Ceder, G. A First-Principles Approach to Studying the Thermal Stability of Oxide Cathode Materials. *Chem. Mater.* **2007**, *19* (3), 543–552. https://doi.org/10.1021/cm0620943.

(24) Lany, S. Semiconductor Thermochemistry in Density Functional Calculations. *Phys. Rev. B* **2008**, *78* (24), 245207. https://doi.org/10.1103/PhysRevB.78.245207.

(25) Henkelman, G.; Uberuaga, B. P.; Jónsson, H. A Climbing Image Nudged Elastic Band Method for Finding Saddle Points and Minimum Energy Paths. *J. Chem. Phys.* **2000**, *113* (22), 9901–9904. https://doi.org/10.1063/1.1329672.

(26) Henkelman, G.; Jónsson, H. Improved Tangent Estimate in the Nudged Elastic Band Method for Finding Minimum Energy Paths and Saddle Points. *J. Chem. Phys.* **2000**, *113* (22), 9978–9985. https://doi.org/10.1063/1.1323224.

(27) Goumans, T. P. M.; Wander, A.; Brown, W. A.; Catlow, C. R. A. Structure and Stability of the (001) α-Quartz Surface. *Phys. Chem. Chem. Phys.* **2007**, *9* (17), 2146–2152. https://doi.org/10.1039/B701176H.

(28) Mohimi, E.; Zhang, Z. V.; Liu, S.; Mallek, J. L.; Girolami, G. S.; Abelson, J. R. Area Selective CVD of Metallic Films from Molybdenum, Iron, and Ruthenium Carbonyl Precursors: Use of Ammonia to Inhibit Nucleation on Oxide Surfaces. *J. Vac. Sci. Technol. A* **2018**, *36* (4), 041507. https://doi.org/10.1116/1.5023236.

(29) Soethoudt, J.; Crahaij, S.; Conard, T.; Delabie, A. Impact of SiO 2 Surface Composition on Trimethylsilane Passivation for Area-Selective Deposition. *J. Mater. Chem. C* **2019**, *7* (38), 11911–11918. https://doi.org/10.1039/C9TC04091A.

(30) Soethoudt, J.; Tomczak, Y.; Meynaerts, B.; Chan, B. T.; Delabie, A. Insight into Selective Surface Reactions of Dimethylamino-Trimethylsilane for Area-Selective Deposition of Metal, Nitride, and Oxide. *J. Phys. Chem. C* **2020**, *124* (13), 7163–7173. https://doi.org/10.1021/acs.jpcc.9b11270.

(31) O'Neill, H. S. C.; Nell, J. Gibbs Free Energies of Formation of RuO2, IrO2, and OsO2: A High-Temperature Electrochemical and Calorimetric Study. *Geochim. Cosmochim. Acta* **1997**, *61* (24), 5279–5293. https://doi.org/10.1016/S0016-7037(97)00317-7.

(32) Emmez, E.; Anibal Boscoboinik, J.; Tenney, S.; Sutter, P.; Shaikhutdinov, S.; Freund, H.-J. Oxidation of the Ru(0001) Surface Covered by Weakly Bound, Ultrathin Silicate Films. *Surf. Sci.* **2016**, *646* (9), 19–25. https://doi.org/10.1016/j.susc.2015.06.019.

(33) Wang, L.; Maxisch, T.; Ceder, G. Oxidation Energies of Transition Metal Oxides within the GGA+U Framework. *Phys. Rev. B - Condens. Matter Mater. Phys.* **2006**, *73* (19), 195107. https://doi.org/10.1103/PhysRevB.73.195107.

(34) Ezzat, S. S.; Mani, P. D.; Khaniya, A.; Kaden, W.; Gall, D.; Barmak, K.; Coffey, K. R. Resistivity and Surface Scattering of (0001) Single Crystal Ruthenium Thin Films. *J. Vac. Sci. Technol. A* **2019**, *37* (3), 031516. https://doi.org/10.1116/1.5093494.

(35) Minjauw, M. M.; Dendooven, J.; Capon, B.; Schaekers, M.; Detavernier, C. Atomic Layer Deposition of Ruthenium at 100 °C Using the RuO 4 -Precursor and H 2. *J. Mater. Chem. C* **2015**, *3* (1), 132–137. https://doi.org/10.1039/C4TC01961J.

(36) Yim, S. S.; Lee, D. J.; Kim, K. S.; Kim, S. H.; Yoon, T. S.; Kim, K. B. Nucleation Kinetics of Ru on Silicon Oxide and Silicon Nitride Surfaces Deposited by Atomic Layer Deposition. *J. Appl. Phys.* **2008**, *103* (11). https://doi.org/10.1063/1.2938052.

(37) Kozodaev, M. G.; Lebedinskii, Y. Y.; Chernikova, A. G.; Korostylev, E. V.; Chouprik, A. A.; Khakimov, R. R.; Markeev, A. M.; Hwang, C. S. Temperature Controlled Ru and RuO 2 Growth via O* Radical-Enhanced Atomic Layer Deposition with Ru(EtCp) 2. *J. Chem. Phys.* **2019**, *151* (20), 204701. https://doi.org/10.1063/1.5107509.

(38) Nørskov, J. K.; Rossmeisl, J.; Logadottir, A.; Lindqvist, L.; Kitchin, J. R.; Bligaard, T.; Jónsson, H. Origin of the Overpotential for Oxygen Reduction at a Fuel-Cell Cathode. *J. Phys. Chem. B* **2004**, *108* (46), 17886–17892. https://doi.org/10.1021/jp047349j.

CHAPTER 6

CONCLUSIONS

4.1 Conclusion

As devices continue to scale down in size, the techniques and materials used to create and pattern each feature adjusts to meet the new demands of the technology. The surface interaction with the precursor and reactant chemistry is one of the fundamental mechanisms which will allow the future of device nanopatterning to advance. AS-ALD fundamentally relies on the catalytic properties of the substrate surface with respect to the precursor and reactants used in the ALD process.

The importance of the surface chemistry in regulating chemical reactions has been shown through the previous chapters. Understanding these reactions and the affect they have on the deposition process is a crucial step in AS-ALD precursor design. One of the best ways to accurately and consistently understand reaction mechanisms and their energetics is through the use of modeling. The theoretical design of a catalysis surface has been described in chapter 3. These design principles allow us to create accurate surface models which can quantitatively predict experimental phenomena. Here the interaction of binary and ternary oxides with O_2, NO_x, and CO_x were studied and used to identify processes to create predictive surface models. It was shown that using both experimental analysis, such as RGA, and theoretical modeling, accurate surface models could be created that reliably predicted NO_x and CO_x desorption temperature, rate, and chemical species, all of which are experimentally verifiable.

This understanding can be applied to the ALD of Co for interconnects in BEOL applications as described by Chapter 4. Co deposition is known to be selective experimentally, in

many cases favoring metals over SiO_2. These properties were studied using DFT by creating surface-precursor-reactant models that could explain these experimental traits. Co precursors often show selective properties due to a few fundamental traits. First is the intrinsic selectivity of Co itself, Co is shown to have a 3-4 eV thermodynamic affinity for metal surfaces over that if SiO_2. Next is the dissociative energy of NH_3 or reductant on the metal and SiO_2 surfaces. NH_3 dissociation is strongly favored on the metal substrates. There are also stronger ligand interactions on the metal surfaces than that of SiO_2. NH_3 may also play a role in passivating the SiO_2 surface further contributing to weaken precursor – surface interactions. The combination of these factors leads to nearly ideal selective deposition favoring the metal substrates at the 180 °C deposition temperature. These metal substrates exhibit strong catalytic traits in both the dissociation of the reductant and the precursor.

Furthermore, the selectivity of multiple Ru precursors in Chapter 5 is investigated. Chapter 5 shows the impact surface passivation has on the precursor – surface interaction. Additionally, the impact of selecting precursor – reactant chemistries that favor certain substrates is explained. RuO_4 is shown to be intrinsically selective as its strong oxidation properties limit the bonding and dissociation on SiO_2. Furthermore, the role defects and labile oxygen have on the deposition of $Ru(EtCp)_2$ is investigated along with the use of dimethylamino-trimethylsilane (DMA-TMS) to passivate the surface with $-CH_3$ groups. $Ru(EtCp)_2$ is also shown to be selective as the chemical bonding to Ru surfaces is superior to that of SiO_2 when passivated. The impact of the reactant O_2 is also studied and shown to play a vital role in removing hydrocarbons from the reaction process making the deposition of Ru and desorption of CO_2 and H_2O exothermic.

These deposition mechanisms for Co and Ru are increasingly important to understand as Co and Ru metal replaces Cu in small interconnects and vias for scaling devices. The improved dielectric diffusion and increase conductivity below cross-sections of 400 nm^2 make Co and Ru viable replacement in BEOL applications. Additionally, the deposition of the metals using AS-ALD can be used to supplement innovative lithography processes such as EUV, reducing costs and accelerating the patterning process.

BIOGRAPHICAL SKETCH

Nickolas Ashburn was born in Austin, Texas in 1995. He received a BA in Physics from Austin College, in Sherman, Texas in 2016. His undergraduate research experience was in superconducting materials, calibration techniques for observatory telescopes using dome flats, and theoretical physics used in studying the orbits of particles and photons around a singularity. In August of 2016 he joined The University of Texas at Dallas in Dr. Kyeongjae Cho's group as a PhD candidate in Materials Science and Engineering. Nick's primary research focuses on chemical vapor deposition for semiconductor device fabrication and catalysis for clean energy applications using a combination of theoretical and experimental approaches.

CURRICULUM VITAE

Nickolas Ashburn

Education

The University of Texas at Dallas August 2016 – May 2021

- PhD candidate in Materials Science and Engineering GPA: 3.73
  - Advisor: Dr. Kyeongjae Cho
- MS in Materials Science and Engineering

Austin College, Sherman, TX August 2013 – May 2016

- BA in Physics / Minor: Mathematics GPA: 3.64 / Cum Laude

Employment and Work Experience

Micron Technology June 2019 – December 2019

- Interned in the TCAD group and performed R&D on device materials and growth methods for AS-ALD of metals and films on various substrates. Worked on 3 projects including MoS_2 growth, Co AS-ALD, and Ru AS-ALD under both NAND and DRAM product groups. Additionally, worked on projects relating to the device fabrication process for 3D NAND. Was required to work closely with various development teams to solve problems and improve device quality and behavior. Used first principle modeling resources, such as Schrodinger and VASP, as well as phase-field models, to get accurate energetics and electronic properties to model surface reactions and interaction properties. This data was consumed by other groups who used it to advance the fabrication process.

Research Assistant at the University of Texas at Dallas August 2016 – May 2021

- More than two years of research on inorganic and metal materials. Worked in conjunction with other research groups to identify new materials and mechanisms for ALD for devices as well as catalysts for pollution control and fuel production. Worked with external companies and research groups from the US, China, and Korea to develop more efficient catalysts and devices.
- Experience in ALD growth and modeling the precursor decomposition and reaction mechanisms on the substrate surface. Studied electrocatalysts including CO_2 reduction carbide, nitride, and pure metal catalysts used for fuel production in a carbon neutral cycle. Also developed metal oxide catalysts for combustion engines such as diesel oxidation catalyst and selective reduction catalysts for both efficiency and longevity including sulfur and water resistance. Developed surface chemistry analysis technique to characterize a material's surface on a molecular level, which is important to catalyst design. Surface and bulk thermodynamic stability studies used in characterizing active and most stable surfaces as well as a material's phase stability both in formation and under environmental conditions.

Teaching Assistant in Physics at Austin College August 2015 –June 2016

- Worked under two professors with one other TA to teach two entry level physics courses. Required to use good communication skills to portray information accurately and timely to a

class with diverse backgrounds. We instructed two labs in physics one and two, classical mechanics and electromagnetism, while also being responsible for teaching occasional courses along with holding office hours and tutoring. Wrote and graded homework, quizzes, and tests.

Undergraduate Research August 2013 – June 2016

- Worked under two different professors with a group of five students to grow carbon nanotubes using a tube furnace and four different concentrations of catalyst. These were analyzed by SEM at the University of Texas, Dallas. Studied superconductors and their transition temperature and electrical properties. Wrote programs to analyze and study the resistance of YBCO at and below its transition temperature. Additionally, studied critical temperature of these superconductors and found an average Tc of 93.9k. Conducted theoretical research on orbits and black holes for physics 231. Calculated the differences in proper and coordinate time for orbits around large gravitational masses for particle orbits. In addition, calculated time for orbits of photons around the same mass. Research in dome flat design for calibrating observatory telescopes at Austin College for advanced research while working with 1 other student to verify accurate calibration could be achieved. Studied environmental climate change in which thermal couple temperature sensors along with humidity sensors were calibrated and tested before being installed at the university weather station. This sensor was used to collect data to determine average temperature change in the area over a period of 12 years. Collected data and poster were used by the city of Sherman in city council meetings. Determined absolute minimums for distribution centers to minimize travel distance for a company. This utilized Lagrange Multipliers and the theorem for absolute minimums, along with partial derivatives and partial integrals, to derive the location in Longitude and Latitude for the distribution center.

Experience and Training

Programming

- Experience with first principal simulations, density functional theory and computational physics including Schrodinger – Poisson modeling and some Monte Carlo.
- Frequent use of C++, Mathematica, Linux systems, MATLAB, and Microsoft Office products. Some additional experience with Python, Fortran, and LabView.

Material Characterization

- Extensive training in X-ray diffraction and unit cell refinement (Rietveld refinement), residual gas analysis (RGA) including calibration and maintenance, gravimetric analysis (TGA), physisorption, and chemisorption techniques, and Fourier transform infrared spectroscopy (FTIR).

Material Synthesis

- Lengthy experience in hydrothermal, coprecipitation – calcination, combustion. Additional experience with ALD, ozone-plasma treating, and chemical bath deposition material synthesis methods.

Leadership and Honors

- Sigma Pi Sigma, Physics Honor Society
- Dean’s List, Austin College, 2014-2015, 2015-2016

- Treasurer, DKE, Austin College

Activities

- Austin College Tennis Team
- Formula SAE

Publications

1. **Ashburn, N.**, Zheng, Y., Thampy, S., Dillon, S., Chabal, Y. J., Hsu, J. W., & Cho, K. (2019). Integrated Experimental–Theoretical Approach To Determine Reliable Molecular Reaction Mechanisms on Transition-Metal Oxide Surfaces. *ACS applied materials & interfaces*, *11*(33), 30460-30469.

2. Thampy, S.[*], **Ashburn, N.[*]**, Martin, T. J., Li, C., Zheng, Y., Chan, J. Y., ... & Hsu, J. W. (2018). Effect of R-site element on crystalline phase and thermal stability of Fe substituted Mn mullite-type oxides: R 2 (Mn 1− x Fe x) 4 O 10− δ (R= Y, Sm or Bi; x= 0, 0.5, 1). *RSC Advances*, *8*(1), 28-37. ([*]: contributed equally)

3. Thampy, S., **Ashburn, N.**, Cho, K., & Hsu, J. W. P. (2021). Earth-Abundant Transition Metal Based Mullite-Type Oxide Catalysts for Heterogeneous Oxidation Reactions. *Advanced Energy and Sustainability Research*, 2000075.

4. Kim, U. H., Park, G. T., Conlin, P., **Ashburn, N.**, Cho, K., Yu, Y. S., ... & Sun, Y. K. (2021). Cation ordering Ni-rich layered cathode for ultra-long battery life. *Energy & Environmental Science*.

5. Thampy, S., **Ashburn, N.**, Dillon, S., Chabal, Y. J., Cho, K., & Hsu, J. W. (2020). Role of Surface Oxygen Vacancies in Intermediate Formation on Mullite-type Oxides upon NO Adsorption. *The Journal of Physical Chemistry C*, *124*(29), 15913-15919.

6. Thampy, S., **Ashburn, N**., Dillon, S., Liu, C., Xiong, K., Mattson, E. C., ... & Hsu, J. W. (2019). Critical Role of Mullite-type Oxides' Surface Chemistry on Catalytic NO Oxidation Performance. *The Journal of Physical Chemistry C*, *123*(9), 5385-5393.

7. Thampy, S., **Ashburn, N.**, Liu, C., Xiong, K., Dillon, S., Zheng, Y., ... & Hsu, J. W. (2019). Superior low-temperature NO catalytic performance of PrMn 2 O 5 over SmMn 2 O 5 mullite-type catalysts. *Catalysis Science & Technology*, *9*(11), 2758-2766.

8. Thampy, S., **Ashburn, N.**, Liu, C., Xiong, K., Dillon, S., Zheng, Y., ... & Hsu, J. W. (2019). Superior Low-Temperature NO Catalytic Performance of $PrMn_2O_5$ over $SmMn_2O_5$ Mullite-Type Catalysts.

9. Zheng, Y., Thampy, S., **Ashburn, N.**, Dillon, S., Wang, L., Jangjou, Y., ... & Cho, K. (2019). Stable and active oxidation catalysis by cooperative lattice oxygen redox on SmMn2O5 mullite surface. *Journal of the American Chemical Society*, *141*(27), 10722-10728.

10. Wang, Q., Liang, C., Zheng, Y., **Ashburn, N.**, Oh, Y. J., Kong, F., ... & Cho, K. (2017). First principles study of the Mn-doping effect on the physical and chemical properties of mullite-family Al 2 SiO 5. *Physical Chemistry Chemical Physics*, *19*(36), 24991-25001.

Conference Presentations

Talks

1. "Role of Surface Catalytic Reactions on Area-selective Atomic Layer Deposition of Co and Ru Interconnect Metals," United Scientific Group CCE. Virtual, (February 22-26, 2021).

2. "Density Functional Theory for Thermal ALD Growth of Co and Ru," SRC Techcon. Virtual, (September 21-25, 2020).

3. "Efficient NO Oxidation via a Modified MvK Reaction Pathway and Cooperative Lattice Oxygen", Well-Defined Materials for Cooperative Catalysis, American Chemical Society, Virtual, (August 16-20, 2020).

4. "Efficient NO Oxidation via a Modified MvK Reaction Pathway and Co-operative Lattice Oxygen," United Scientific Group CCE. Houston, Texas, (February 24-26, 2019).

Posters

1. Sean Dillon, Sampreetha Thampy, **Nickolas Ashburn**, Eric C. Mattson, Yongping Zheng, Chengfa Liu, Ka Xiong, Yves J Chabal, Kyeongjae Cho, and Julia W. P. Hsu, "Synthesis Method Effect on The Surface Chemistry and Oxidation Activity of RMn2O5 (R=Sm, Bi) Mullite-Type Oxidation Catalysts," Southwest Catalysis Society, Houston, Texas, (April 2018).

2. Sampreetha Thampy, **Nickolas Ashburn**, Sean Dillon, Yongping Zheng, Chengfa Liu, Ka Xiong, Yves Chabal, Kyeongjae Cho, and Julia W.P. Hsu, "$PrMn_2O_5$ Mullite-type Oxides as Low Temperature and Highly Efficient NO Oxidation Catalysts," Southwest Catalysis Society, Houston, Texas, (April 2018).

3. **Nickolas Ashburn**, Yemisirach Seyoum, Faith Sourber, AnnaBeth Thomas, and Andy Villarreal, "Synthesis of High Temperature Superconductors and their Magnetic Properties," Austin College Student Sholarship Conference, Sherman, Texas, (March 2016).

4. **Nickolas Ashburn**, John Happel, and Dr. David Baker, "Local Warming? Temperature and Dew Point Change In Grayson County," Austin College Posey Leadership Award event, Perot Museum of Nature and Science, Dallas, Texas, (March 2015).